ABSTRACT

Title of dissertation: DELAY INDUCED INSTABILITIES IN
COUPLED SEMICONDUCTOR LASERS AND
MACKEY-GLASS ELECTRONIC CIRCUITS

Min-Young Kim, Doctor of Philosophy, 2005

Dissertation directed by: Professor Rajarshi Roy
Department of Physics

We describe two experimental systems where a time-delayed feedback mech-
anism plays an important role in inducing instabilities. The first system consists
of two cross-coupled semiconductor lasers with time-delayed negative optoelectronic
feedback. This system is described by coupled delay-differential equations, and we
explore the dynamics near the onset of oscillations as the coupling strength is varied.
We study the influence of asymmetric coupling strengths on the onset of oscillations
and the dependence of the amplitudes of oscillations on the coupling strengths. In-
phase oscillations with a period of twice the delay time emerge as the product of
coupling strengths increases above a critical value. A scaling relationship is ob-
served between rescaled amplitudes of oscillations and the product of the coupling
strengths. We also study the dependence of the periodicity and the phase relations
of the oscillations as we adjust the delay time.

The second system is an electronic circuit with time-delayed nonlinear feed-
back which simulates the Mackey-Glass model described by a delay-differential equa-

tion. First we study the dynamics of the Mackey-Glass system in various parameter regimes and then we study the synchronization of two unidirectionally coupled Mackey-Glass circuits. The change of the quality of the synchronization with parameter mismatch as well as bandwidth limitations in the transmission channel is investigated. With a low pass filter in the transmission line, we find that the inclusion of the dominant frequency component of the original driver signals is crucial to achieve synchronization between the driver and receiver circuits, both numerically and experimentally.

DELAY INDUCED INSTABILITIES IN
COUPLED SEMICONDUCTOR LASERS AND
MACKEY-GLASS ELECTRONIC CIRCUITS

by

Min-Young Kim

Dissertation submitted to the Faculty of the Graduate School of the
University of Maryland, College Park in partial fulfillment
of the requirements for the degree of
Doctor of Philosophy
2005

Advisory Committee:

Professor Rajarshi Roy, Chair/Advisor
Dr. Joan L. Aron
Professor Michael A. Coplan
Professor Robert Dorfman
Professor Edward Ott
Dr. Ira B. Schwartz

For my mom and dad, and my husband.

ACKNOWLEDGMENTS

the first pair of working Mackey-Glass circuits and Chris Sramek took experimental data for the coupled circuits with bandwidth limitations on the transmission line. I would also like to acknowledge help and support from some of the staff members. Donald Martin's technical help is highly appreciated, as is the computer hardware support from Edward Condon, LaTex and software help from Dorothea Brosius and purchasing help from Nancy Boone.

My colleagues at the nonlinear optics laboratory have made the lab experience to be pleasant and valuable. Former graduate students, Wing-Shun Lam, Bhaskar Khubchandani, David DeShazer, Christian Silva and Ryan McAllister, welcomed me to the lab and helped me with suggestions and comments about the research. Current graduate students, Beth Rogers, Will Ray and Tony Franz, have supported me with helpful discussions and humor. In particular, I would like to recognize the editorial contributions of Beth and Will. I wish happiness for Beth and her fiance, Dan Dakin, and for Will and his fiance, Heather Downey. A post-doctoral researcher, Dr. Fabien Rogister, helped me to understand the numerical algorithm for simulating delay-differential equations.

During my five years at University of Maryland, I had the pleasure of sharing my life with a fine group of people: Matt, Junjie, Yung-Fu, Mike, Torr, Willie, Brian, Su-Young, Kyuyong, Youngchan, Maria, Jonghee, Hanhee, Sejin, Bora, Youngsoo, Junghwan, Sooseung, Il-Chul, Yongsun, Yong-Seok, Yuri and Seung-Jong. I would like to thank people from ballroom dancing group for the special memories: Karen, Noriko and Steve, Jason, Shreyas, Atul, Alden and Igor, Emiko and Rex, Joe, Lisa, Malaika, Shannon and Chris, Melissa, Don, Cindy and Ed, Erin, Rebecca and Min.

iv

For more than twenty years of education, there have been a number of people who have influenced my career. I would like to recognize my high school physics teacher, Boo-Ho Choi, and my alumni friends, Dr. Young-Tae Chang and Dr. Kwangduk Lee, in particular. I thank Na-Young Park who made me enjoy learning English from the beginning.

Finally, I would like to thank my family for giving me the support to achieve the first goal in my life. My parents taught me to be independent and responsible. I owe my deepest appreciation and thanks to my mom for her enduring love and mental support. I extend my thanks to Jeong-Min, Hee-Yeon, Young-Woo and my parents-in-law.

It is impossible for me to fully express the extent of my gratitude to my husband, Young-Jun Sohn, for the endless patience, encouragement, faith and love that he has shown me for last ten years. Without him, I would not even have considered a Ph.D. program. He has taught me how to live freely and emphasized the importance of having dreams. Thank you so much and I love you.

TABLE OF CONTENTS

LIST OF TABLES

LIST OF FIGURES

xiii

Chapter 1

Introduction

1.1 Delay Induced Instabilities

Nonlinear dynamics and complex behaviors have been actively studied recently in various fields of research in biology, chemistry, and physics. In particular, instabilities in nonlinear systems induced by the finite propagation time of signals has attracted much attention, where the dynamics depend not only on the current state but also on the state in the past. A few examples include optical systems with delayed feedback [1, 2, 3], physiological systems with time-delayed control [4], and ecosystems with time-delayed regulatory mechanisms [5]. Delay differential equations which describe the dynamics of above examples are important for practical applications, and also serve as suitable topics for a numerical and analytical discussion.

In this thesis, we study two experimental systems where a time-delayed feedback mechanism plays an important role in inducing instabilities. The first system consists of two cross-coupled semiconductor lasers with a time-delayed negative optoelectronic feedback. Isolated laser diodes exhibit simple steady state behavior with a constant injection current. Nonlinear dynamics are observed when the laser diodes are current modulated, or optically injected from another laser, or subjected to delayed optical or optoelectronic feedbacks [6, 7, 8, 9, 10, 11, 12]. In our setup,

the feedback current proportional to the light intensity fluctuations in one laser modulates the injection current of the other laser through an optoelectronic delay loop. The dynamics of cross-coupled lasers will be investigated for different parameter regimes. We study the influence of asymmetric coupling strengths on the onset of oscillations and relate the amplitude of oscillations and the coupling strengths. The periodicity and phase relations are studied by adjusting the delay time. The effect of external modulation is also considered.

Single laser oscillators with instabilities induced by time-delayed feedback have been studied for at least two decades [13, 14, 15]. Previous theoretical studies of globally coupled nonlinear oscillators with time-delayed coupling [16, 17, 18] have examined their synchronization as a function of coupling strength but do not include the relaxation dynamics of populations with different time scales of decay. Moreover, it has been considered very complicated to analyze the laser system with time-delayed coupling or feedback, both mathematically and numerically, when the delay time is very long compared with the characteristic time scale of the relaxation dynamics [19, 20]. The numerical computation takes a long time in order to obtain non-transient behavior of the system when the delay time is very long. In addition, since there are many parameters in the coupled laser systems, it is difficult to predict the dynamics for different parameter regimes. With our coupled laser experiments, however, we can get a quick overview of the change in the system dynamics for different parameter values. Therefore, the experiments lead us to identify important control parameters of the system and to develop a model that can be studied numerically and analytically to verify the experimental observations.

Our experiments with cross-coupled semiconductor lasers were initially motivated by the formal correspondences between laser population dynamics and epidemic population dynamics. The dynamics of each system can be described by two variables with different time scales, i.e., one fast variable and one slow variable, and the nonlinear interaction between two variables, together with the dissipative mechanism of each variable, determine the time evolution of the system. In the study of disease population dynamics, the interaction between noise and nonlinear dynamics and the synchronization of the spatial patterns are considered to be very important [5, 21, 22, 23, 24, 25]. Yet the role of delays in the transmission of disease caused by migration between populations has received inadequate study. Most of the research on the transmission of a disease in coupled population models has been done under a theoretical framework of symmetric conditions and instantaneous transmission between populations [25, 26, 27, 28].

An analog system of laser experiments can serve as a powerful tool to investigate the influence of the time delay and asymmetric coupling on the population dynamics of a disease. First, it is difficult to control the epidemic population dynamics in the real world and secondly it takes years of data gathering for the empirical studies of the long-term dynamics in the disease population. The laser experiments, which take a few hours to yield data over a wide range of parameters, enable us to study the possible role of the particular parameters in the epidemics. Our observations with the laser experiments underline the importance of understanding the underlying mechanisms in the transmission of the disease with a finite propagation time delay in order to predict an epidemic outbreak or periodicity.

The Mackey-Glass analog electronic circuit is the second system we study where a time-delayed feedback introduces instabilities in a nonlinear system. Ever since Mackey and Glass suggested a mathematical model to describe the dynamics of a physiological control system [4], there have been numerous studies on the Mackey-Glass model [29, 30, 31, 32, 33, 34, 35, 36, 37]. It is well known that the Mackey-Glass system, described by a delay differential equation, shows steady, periodic, and chaotic dynamics as the delay time is varied, and the dimension of the system is proportional to the delay time [29]. Using electronic circuits simulating Mackey-Glass systems, we study the synchronization of two unidirectionally coupled Mackey-Glass systems.

The synchronization of chaotic systems has been investigated extensively because of its potential applications in communications [38, 39, 40, 41, 42, 43, 44, 45, 46]. A chaotic signal is used as a broadband carrier and an information signal containing a message is added to the chaotic signal or a parameter of the driver is modulated by the information signal for the transmission of the chaotic signal. Here, the synchronization between the driver and the receiver is necessary to recover the information at the receiver. However, there have been few studies on the synchronization of chaotic systems with filtered signal and channel noise [47, 48, 49, 50]. The signal from the driver can be altered when it passes through the transmission channel, and we investigate the properties of synchronization with frequency bandwidth limitations in the transmission channel. The effect of the linear amplification or attenuation in the transmission channel is considered as well.

1.2 Outline of the Thesis

This thesis consists of two parts. First we present the dynamics of cross-coupled semiconductor lasers in Chapters 2, 3, and 4. The dynamics of unidirectionally coupled Mackey-Glass electronic circuits will be considered in Chapters 5 and 6.

In Chapter 2, a brief introduction of semiconductor lasers will be followed by description of the numerical model for a single-mode laser diode. The rate equations are analyzed mathematically to understand the steady state behavior and the relaxation oscillations of the system. Then an analogy between laser population dynamics and disease population dynamics will be introduced to motivate the research presented in Chapters 3 and 4.

In Chapter 3, we study the dynamics of two cross-coupled lasers with delayed negative optoelectronic feedback. In the experiment, we explore the dynamics near the onset of oscillations. In-phase oscillations with a period of twice the delay time emerge as the product of coupling strengths increases through a critical constant, and we discover a scaling law that relates the amplitudes of oscillations and the coupling strengths. Linear stability analysis and numerical simulations of the rescaled coupled laser equations are also carried out and they are consistent with observations from the experiments.

In Chapter 4, we study the periodicity and the phase relation of the cross-coupled lasers as we adjust the delay time experimentally. In-phase oscillations with a fundamental frequency dominate for smaller delay times, while anti-phase oscillations with higher harmonic frequencies appear as the delay time is increased.

We discuss the competition between dynamics of different time scales. The effect of an external modulation is also considered.

The chaotic dynamics of Mackey-Glass electronic circuits are presented in Chapter 5. First we review the dynamics of Mackey-Glass system by varying the delay time and introduce an analog circuit which simulates the system. Then we study the dynamics of the system by varying the linear gain of the feedback term. Both the delay time and the linear gain can be used as control parameters to determine the dynamics of the system and display a period doubling route to chaos. Chaotic signals generated from a Mackey-Glass circuit in the experiment are compared to numerical simulations with matching parameters.

In Chapter 6, we study the synchronization of two unidirectionally coupled Mackey-Glass circuits with an open-loop receiver configuration. To characterize the quality of synchronization, the time-shifted cross-correlation coefficient is calculated between the driver and the receiver signals. The quality of synchronization with parameter mismatch is investigated through numerical simulations. The synchronization between the driver and receiver circuits is found to be more sensitive to the strength of the coupling strength than to mismatched circuit parameters. Secondly, we study the synchronization with bandwidth limitation in the transmission channel. With a low pass filter in the transmission line, we find that the inclusion of the dominant frequency component of the original driver signals is crucial to achieve synchronization between the driver and receiver circuits, both numerically and experimentally. The maximum cross-correlation and the corresponding time shift reveal that the frequency dependent attenuation and phase distortion

6

occurring during the transmission change the quality of synchronization.

Chapter 7 concludes this thesis with a summary and future work.

Chapter 2

Dynamics of Semiconductor Lasers

2.1   Introduction to Semiconductor Lasers

Laser, or Light Amplification by Stimulated Emission of Radiation, is an optical os-
cillator. All lasers perform light amplification by stimulated emission and feedback
of light by a reflecting mirror. Lasers are sources of highly directional, monochro-
matic, coherent light.

Semiconductor lasers are one of the most important class of lasers in use today.
Compact semiconductor lasers are made by sandwiching the active semiconductor
medium between another semiconductor material that has a larger band-gap en-
ergy and a small index of refraction to confine the optical field. Such a double
heterostructure permits the effective confinement of carriers (electrons and holes)
and light. Using AlGaAs and InGaAsP, one can easily obtain lasers in the range of
$0.8 - 1.6 \mu$m. Semiconductor lasers emitting at 1.3 μm and 1.55 μm wavelengths are
of particular interest because of their application in optical fiber communications
[51].

One simple and commonly used laser consists of a forward-biased p-n junc-
tion. Fig. 2.1 shows the energy-band diagram of the p-n homojunction (junction
between two similar semiconductors). When a p-type and an n-type semiconduc-
tor are brought into contact with each other, an equilibrium is established through
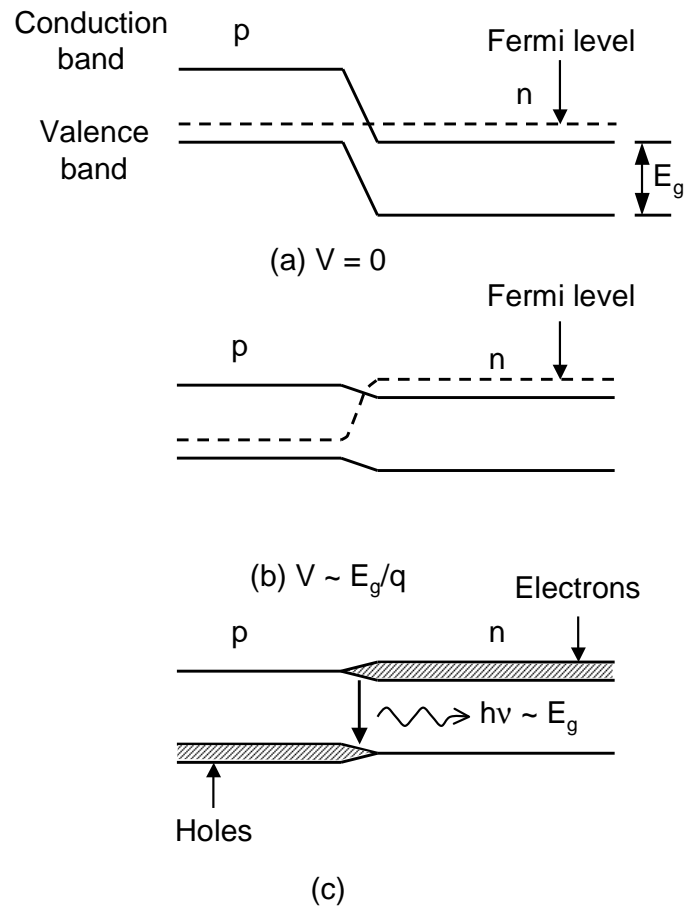
Figure 2.1: Energy diagram of a p-n junction at (a) zero bias and (b) forward bias. (c) Schematic representation of the electron and hole densities under forward bias [51].

diffusion of electrons from the n side to the p side, while the reverse occurs for holes (empty electron states). These diffusing electrons and holes recombine in the junction region, establishing an electric field across the p-n junction, which opposes further diffusion. When a p-n junction is forward biased by applying an external voltage, the built-in electric field is reduced, allowing further diffusion of electrons and holes across the junction. These electrons and holes can recombine either radiatively or nonradiatively. Photons of energy $h\nu \sim E_g$ are emitted during the radiative recombination. However, these photons can be absorbed through a reverse process that generates electron-hole pairs. When the rate of photon emission exceeds that of absorption, then the p-n junction is able to amplify the electromagnetic radiation.

Fig. 2.2 shows the energy-band diagram for a double heterostructure laser. The thin p-type active region has a lower band gap compared to that of the two p-type and n-type cladding layers. The charge carriers can move freely to the active region under forward bias, but they cannot cross over to the other side because of the potential barrier resulting from the band-gap difference. This allows a large electron and hole population inside the active region, where they recombine to produce optical gain. On the other hand, the active layer has a higher refractive index compared with that of the surrounding cladding layers. Therefore, the active layer acts as a dielectric waveguide wherein the generated optical field remain confined.

When current is applied to the semiconductor laser, charge carriers are injected into the thin active region, where they can recombine through either radiative or nonradiative mechanisms. A nonradiative mechanism, known as the Auger process, is intrinsic and the energy released by the electron-hole recombination is
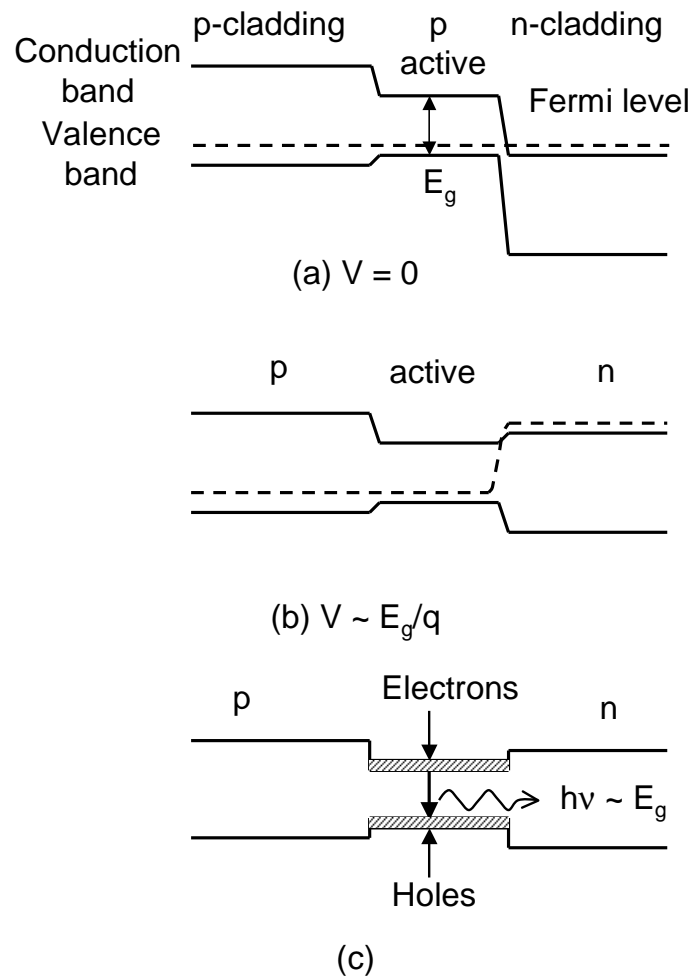
Figure 2.2: Energy diagram of a double heterostructure semiconductor laser at (a) zero bias and (b) forward bias. (c) Schematic representation of the electron and hole densities under forward bias [51].

conduction band

valence band

(a)   (b)   (c)
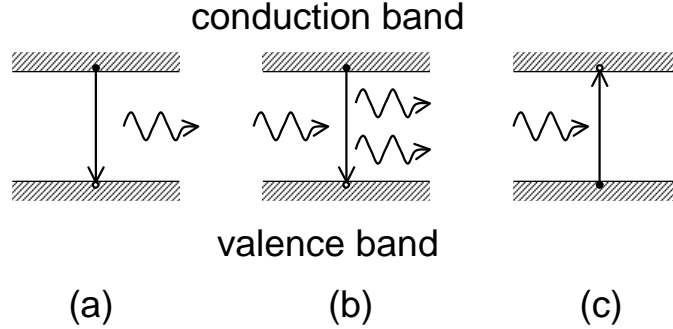
Figure 2.3: Schematic illustration of (a) spontaneous emission, (b) stimulated emission and (c) absorption processes [51].

taken by a third charge carrier. Radiative recombination occurs when an electron in the conduction band recombines with a hole in the valence band and the excess energy is emitted in the form of a photon. This can happen through two optical processes known as spontaneous emission and stimulated emission. Fig. 2.3 shows these processes schematically. In spontaneous emission, photons can be emitted in any direction with no phase relationship among them. Stimulated emission is initiated by an already existing photon and the emitted photon has the same wavelength, phase and propagation direction as the incident photons.

In addition to the optical gain, optical feedback is required to operate a laser. In semiconductor lasers, the cleaved facets of the gain medium form a Fabry-Perot (FP) cavity and provide sufficient optical feedback (Fig. 2.4). Only photons travelling perpendicular to the facets can be amplified by stimulation emission process and the feedback is strongest for wavelengths corresponding to the longitudinal modes of the Fabry-Perot cavity.

When the injected current is small, absorption dominates and the laser doesn't
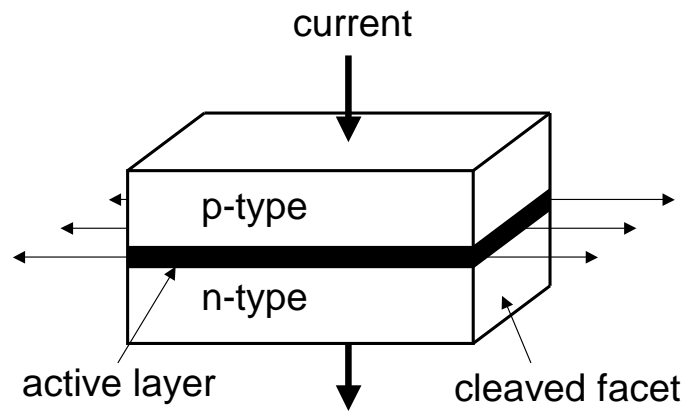
Figure 2.4: Schematic illustration of an edge-emitting semiconductor laser with double-heterostructure [51].
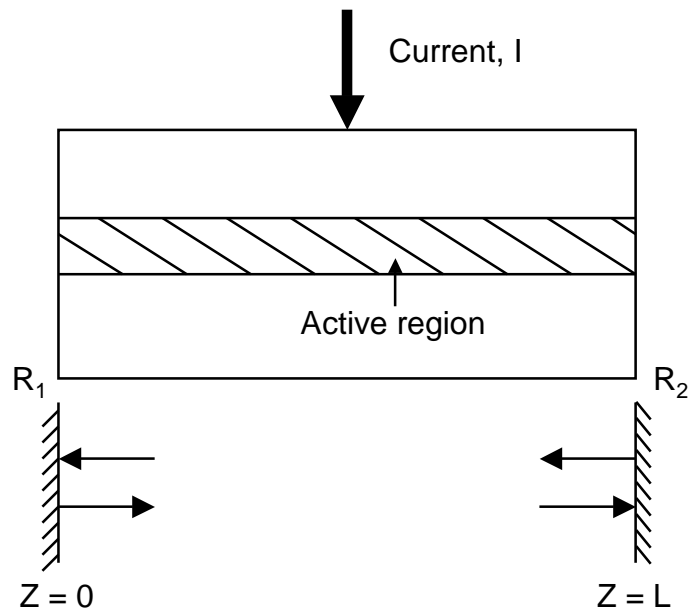
Figure 2.5: Schematic illustration of an semiconductor laser and corresponding Fabry-Perot cavity [51].
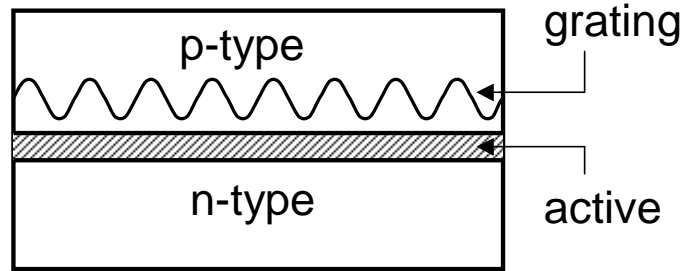
Figure 2.6: Schematic illustration of a distributed-feedback (DFB) semiconductor laser [51].

emit coherent light. The rate of stimulated emission increases as the externally injected current increases and at a certain value of the external current, the rate of stimulated emission becomes equal to the rate of photon absorption, making the semiconductor optically transparent. Beyond transparency, the net stimulated emission occurs and photons are emitted. However, not all photons make it out of the cavity, some are lost through the partially transmitting facets and some get scattered or absorbed inside the cavity. These are the cavity losses. At threshold, gain equals loss and stimulated emission begins to dominate. Above threshold, the laser output increases almost linearly with the current, while the number of electron-hole pairs remains almost stable at its threshold value.

Besides the Fabry-Perot resonator structure, distributed feedback (DFB) is often employed in semiconductor lasers to achieve single-frequency operation. In a resonator, a grating with a periodicity is imposed on or near a waveguide as shown in Fig. 2.6 and a strong reflection is produced when the scattered waves superpose in-phase. Typical optical spectra of a Fabry-Perot laser and a distributed feedback
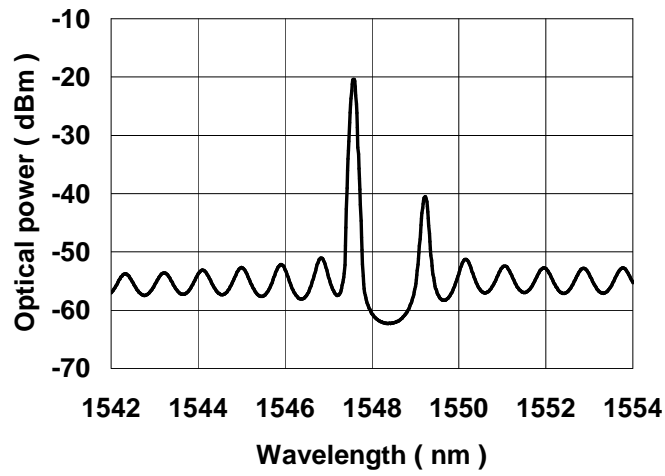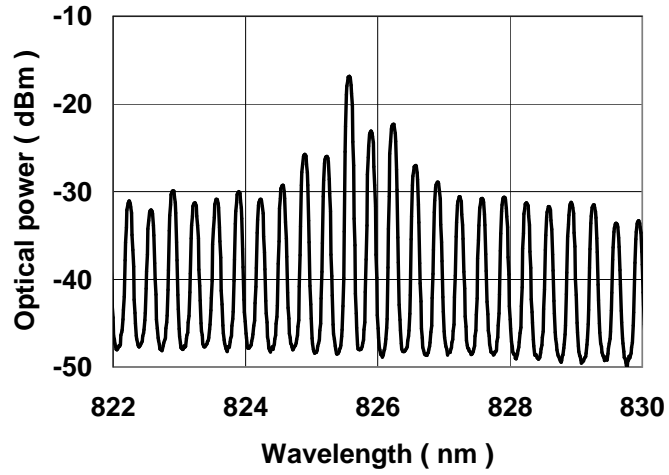
Figure 2.7: Typical optical spectrum of (a) a Fabry-Perot laser and (b) a distributed feedback laser.

laser are shown in Fig. 2.7.

2.2 Single-mode Solitary Laser Diode

2.2.1 Rate Equations

The dynamical behavior of a semiconductor laser can be modelled by rate equations, a set of first order differential equations that describe the evolution of the optical field and carrier number [51]. The dynamics of a single mode semiconductor laser is described by

$$\dot{E} = \frac{(1+i\alpha)}{2}\left[G - \gamma_p\right]E \tag{2.1}$$

$$\dot{N} = \frac{I}{q} - \gamma_e N - G|E|^2 \tag{2.2}$$

where E is the complex optical field, N is the carrier number, α is the linewidth enhancement factor, G is gain per second, and I is the injection current. The loss due to absorptions or transmission through the reflective facets is denoted by γ_p, q is the charge of the electron, γ_e is the rate of non-radiative recombination of electron-hole pairs. The last term in Eqn. 2.2 accounts for the loss of electron-hole pairs due to the stimulated recombination.

Assuming that the optical gain increases linearly with the number of electron-hole pair for all values of the injection current, the gain $G(N)$ can be approximated as

$$G = G(N) = \left.\frac{\partial G}{\partial N}\right|_{N_0} (N - N_0) = G_N(N - N_0) \tag{2.3}$$

where N_0 is the carrier number at transparency and $G_N = \partial G/\partial N$ is the differential gain. When the solitary laser is pumped far above threshold, the gain saturates and

is often rewritten as

$$G = G(N, |E|^2) = G_N(N - N_0)(1 - \epsilon|E|^2) \tag{2.4}$$

where ϵ is the gain saturation coefficient of the laser. The role of gain saturation is less relevant when the laser is operated close to threshold.

Eqn. 2.1 and Eqn. 2.2 are deterministic and contain no noise. The contribution of the spontaneous emission can be included by adding a Langevin noise current to the rate equations such that

$$\dot{E} = \frac{(1 + i\alpha)}{2}\left[G(N, |E|^2) - \gamma_p\right]E + F_E(t) \tag{2.5}$$

where $F_E(t)$ is the noise term, satisfying the relations

$$< F_E(t) > \; = \; 0, \tag{2.6}$$

$$< F_E(t)F_E^*(t') > \; = \; R_{sp}\delta(t - t') \tag{2.7}$$

where R_{sp} is the rate of spontaneous emission. In this thesis, we focus on the deterministic model by ignoring the spontaneous emission process.

Until now, we have considered rate equations for the slowly-varying complex field amplitude $E(t)$. It is often convenient to consider the dynamics of the photon number $P(t)$ and the phase $\phi(t)$ instead of the complex electric field because they are observables. Introducing the relation

$$E(t) = \sqrt{P(t)}\exp(i\phi(t)), \tag{2.8}$$

Eqn. 2.1 can be rewritten as

$$\frac{dP(t)}{dt} \; = \; \left[G(N, P) - \gamma_p\right]P(t), \tag{2.9}$$

$$\frac{d\phi(t)}{dt} \; = \; \frac{\alpha}{2}\left[G(N, P) - \gamma_p\right], \tag{2.10}$$

17

whereas Eqn. 2.2 becomes

$$\frac{dN}{dt} = \frac{I}{q} - \gamma_e N - G(N, P)P, \tag{2.11}$$

where the nonlinear gain is

$$G(N, P) = G_N(N - N_0)(1 - \epsilon P). \tag{2.12}$$

2.2.2 Steady State Solutions

In this section, we study the dependence of the steady state solutions of the rate equations, Eqns. 2.9 - 2.12, on the injection current. The steady state solutions are characterized by a constant photon number P_s, a constant carrier number N_s, and a constant frequency shift $\Delta\omega_s$ with respect to the threshold frequency ω_s, and we assume that the gain saturation effect is negligible, i.e., $\epsilon = 0$. By taking the time derivatives of P and N to be zero and the time derivative of ϕ to be $\Delta\omega_s$, we have

$$\left[G_N(N_s - N_0) - \gamma_p \right] P_s = 0, \tag{2.13}$$

$$\frac{I}{q} - \gamma_e N_s - G_N(N_s - N_0)P_s = 0, \tag{2.14}$$

$$\Delta\omega_s = \frac{\alpha}{2}\left[G_N(N_s - N_0) - \gamma_p \right]. \tag{2.15}$$

There are two steady state solutions given by

$$P_s = 0, \ N_s = \frac{I}{\gamma_e q} \text{ and } \Delta\omega_s = \frac{\alpha}{2}G_N\left[\frac{I}{\gamma_e q} - \frac{I_{th}}{\gamma_e q} \right], \tag{2.16}$$

and

$$P_s = \frac{I - I_{th}}{\gamma_p q}, \ N_s = N_{th} \text{ and } \Delta\omega_s = 0, \tag{2.17}$$

where $I_{th} = \gamma_e q N_{th}$ is the threshold current and $N_{th} = N_0 + \gamma_p/G_N$ is the threshold carrier number.

18
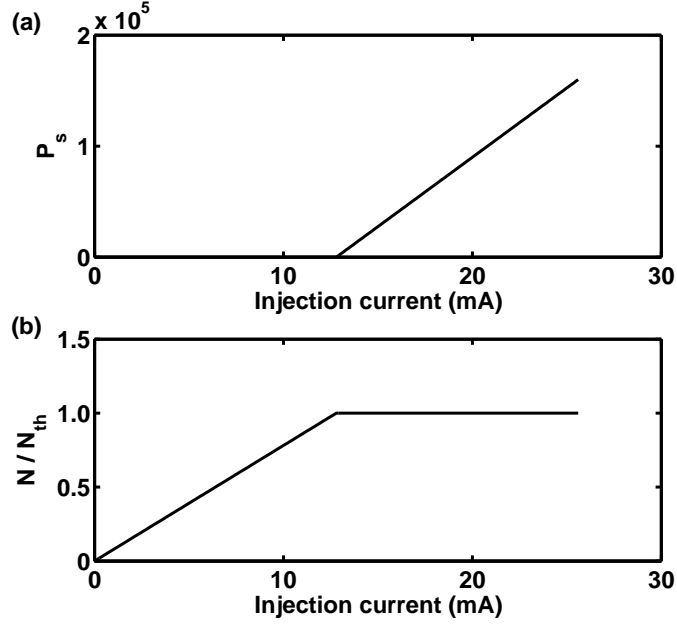
Figure 2.8: The steady state behavior of a laser obtained from numerical simulation. (a) The photon number P_s versus the injection current. (b) The carrier number normalized to the threshold carrier number N/N_{th} versus the injection current.

Since the photon number and the carrier number cannot be negative, the second solution is physically meaningful only for $I > I_{th}$. Below the threshold, the carrier number and the frequency shift obey the first solution and increase linearly with the injection current with no photon in the laser cavity. Above threshold, the first solution becomes unstable and the second solution becomes stable. Therefore, the photon number increases linearly with the injection current while the carrier number and the frequency shift are clamped to their threshold values.

Fig. 2.8 shows the photon number-current (P-I) and the carrier number-current (N-I) curves obtained from Eqn. 2.13 and 2.14 with parameter values given in Table 2.1.

Symbol	Parameter	Value
α	Linewidth enhancement factor	4
G_N	Differential gain	$10^4 \ sec^{-1}$
N_0	Carrier number at transparency	1.1×10^8
γ_e	Carrier recombination rate	$0.5 \times 10^9 \ sec^{-1}$
γ_p	Photon decay rate	$0.5 \times 10^{12} \ sec^{-1}$

Table 2.1: Parameter values for solitary semiconductor laser

2.2.3 Relaxation Oscillations

The output of a semiconductor laser exhibits damped periodic oscillations before settling down to its steady state value, which is called as relaxation oscillations. Fig. 2.9 shows the temporal evolution of N and P calculated numerically using parameter values in Table 2.1 at $I = 1.1 I_{th}$. An expression for the frequency and decay rate can be obtained using the small signal analysis of the single-mode rate equations, where the steady state values of P and N are perturbed by a small amount δP and δN. The rate equations, Eqns. 2.9 - 2.11, are linearized by neglecting the quadratic and higher powers of δP and δN. We then obtain

$$\delta \dot{P} = G_N P_s \delta N, \tag{2.18}$$

$$\delta \dot{N} = -\gamma_p \delta P - (\gamma_e + G_N P_s) \delta N. \tag{2.19}$$

If we assume an exponential time dependence

$$\delta P(t) = \delta P_0 \exp(\lambda t), \tag{2.20}$$

$$\delta N(t) = \delta N_0 \exp(\lambda t), \tag{2.21}$$

Figure 2.9: Time evolution of the photon number (P) and the carrier number (N) exhibiting relaxation oscillations.

where δP_0 and δN_0 are the initial values of the perturbation, the constant s satisfies

$$\lambda(\lambda + \gamma_e + G_N P_s) + \gamma_p G_N P_s = 0, \tag{2.22}$$

i.e.,

$$\lambda = -\Gamma_R \pm i\Omega_R, \tag{2.23}$$

where

$$\Gamma_R = \frac{\gamma_e + G_N P_s}{2} \tag{2.24}$$

is the decay rate of relaxation oscillations and

$$\Omega_R = \left(\gamma_p G_N P_s - \Gamma_R^2\right)^{1/2} \tag{2.25}$$

is the angular frequency of relaxation oscillations. For strongly spiking lasers, $\gamma_e \ll \gamma_p$ and to a good approximation

$$\Omega_R \cong (\gamma_p G_N P_s)^{1/2} = \left[\frac{G_N(I - I_{th})}{q}\right]^{1/2}. \qquad (2.26)$$

Since the decay rate is positive, fluctuations from the steady state exhibit damped relaxation oscillations.
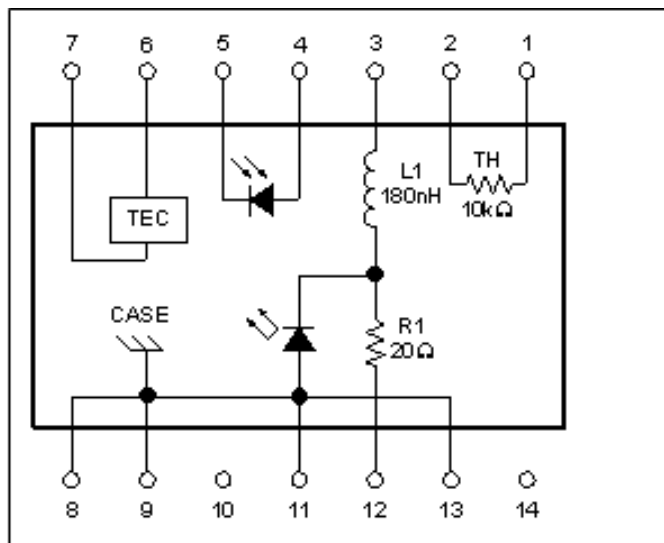
Figure 2.10: Schematic pin diagram for Fitel DFB laser diode (FOL15DCWD-A81-19345). 1 and 2: thermistor connections; 3: laser DC bias (-); 4: Monitor diode anode; 5: Monitor diode cathode; 6: TEC (+); 7: TEC (-); 8 and 9: case ground; 10 and 14: no connections; 11: laser DC bias (+), ground common; 12: laser RF (-); 13: laser DC bias (+), ground common.

2.3 Basic Measurements

We utilize a 1550 nm wavelength distributed feedback (DFB) laser diode (Fitel FOL15DCWD-A81) pigtailed to polarization maintaining fiber. Fig. 2.10 is the pin diagram where the diode is configured with a thermoelectric cooler (TEC), a thermistor (TH) and a bias-T structure for adding an RF component to the injection current. The TEC connected to a temperature controller (Newport 350) provides $0.01°C$ temperature stability, minimizing the frequency and power drift due to heating effects. A laser diode driver (Newport 505) provides DC injection current

23

with 0.1 mA resolution. The light generated by the laser propagates through the fiber which is connected to a photodetector or to an optical spectrum analyzer for observations.

Fig. 2.11 is the light power-current measurements for two DFB lasers (LD_1, LD_2) taking a multi-function optical meter (Newport 1835-C and 818-IR) in continuous operation mode. By calculating the best fit lines in linear operation region for each laser, the threshold current values are obtained. I_{th} is 9.1 mA for LD_1 and 11.7 mA for LD_2.

The relaxation oscillations can be monitored by an RF spectrum analyzer (Hewlett-Packard 8559A, $0.01 \sim 21$ GHz) with a photodetector (New Focus 1611, 30 $kHz \sim 1$ GHz) which produces voltage proportional to the light power fluctuations. We can see a peak on the screen that shifts towards larger frequencies with increasing injection current. Fig. 2.12 shows the dependence of the relaxation oscillation frequency on the injection current.

In addition to the RF spectrum, the optical spectrum of two semiconductor lasers is measured using an optical spectrum analyzer (Agilent 86141B). Fig. 2.13 shows the optical power spectral density as a function of wavelength for two lasers (LD_1 and LD_2). Laser 1 is centered at 1548.05 nm and laser 2 at 1547.58 nm and both of them show a single longitudinal mode with the largest side mode suppressed by more than 20 dB.
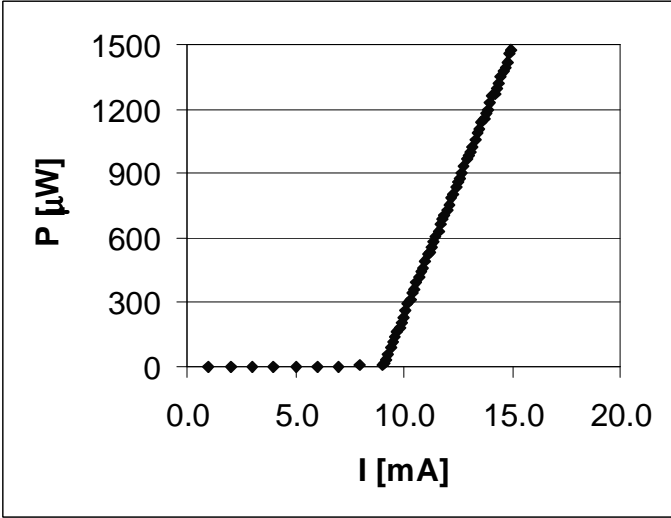
(a)
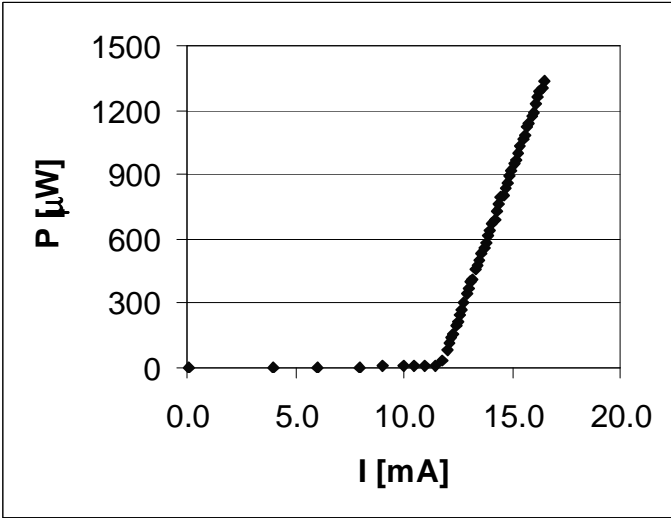
(b)

Figure 2.11: Light-current measurements for (a) laser 1 and (b) laser 2.
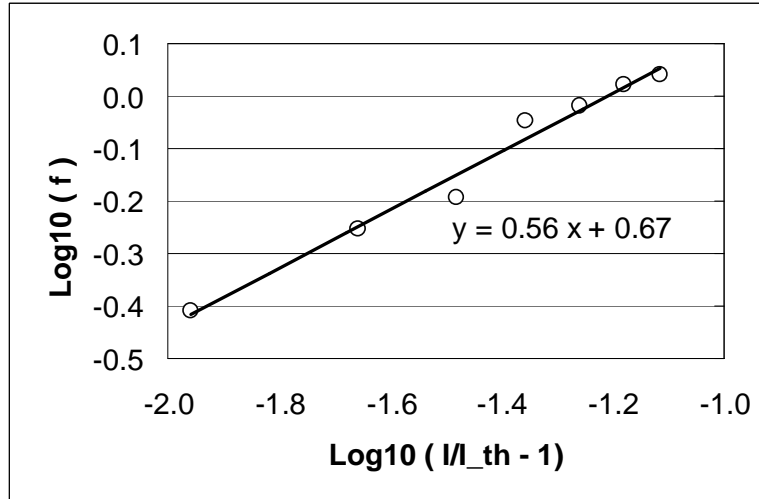
Figure 2.12: The relaxation oscillation frequency as a function of injection current.
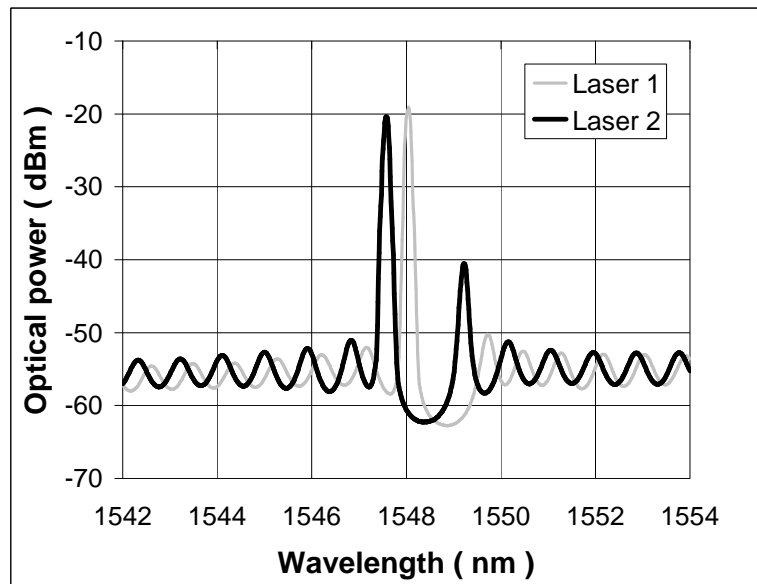
Figure 2.13: The optical spectrum of two semiconductor lasers.

2.4 Analogy between Laser Population Dynamics and Disease Population Dynamics

So far, we have explained the principles of the semiconductor lasers and studied the mathematical model which describes the dynamics of the semiconductor lasers. It is interesting to notice that Charles Townes, who won the Nobel Prize for his role in the invention of the maser (microwave amplification by stimulated emission of radiation) and the laser, formulated the mathematical model of the maser based on concepts from microbial population growth. Microbial population fluctuation occurs when microbes are both dying and multiplying (by division) at the same time. Likewise, the photons in the maser are both dying (via absorption) and being born (via stimulated emission) simultaneously [52, 53]. Billings and co-workers later showed the similarities of a class of population and laser models, both analytically and topologically [54]. This unexpected correspondence between the dynamics of the photon population and the dynamics of the population in the biological system encouraged us to apply the results from the laser models to understand interesting phenomena in biological systems. In this section, we study the analogy between laser population dynamics and disease population dynamics.

One of the most challenging problems in population dynamics is that of predicting the origin of large-amplitude events such as major outbreaks of infectious diseases. Better understanding and prediction will lead to improved ways to manage, limit or prevent disease. Prediction depends on advances in knowledge of the underlying dynamics of infection, which may display periodicity, chaotic fluctuations, spa-

tial synchrony, and other patterns of behavior. Many studies of these types of behaviors in recent decades have explored the effects of many factors, including stochastic noise, seasonal forcing, climatic forcing, nonlinearities in contact rates, spatial heterogeneity, and time delays in single-population models [24, 27, 54, 55, 56, 57, 58, 59].

One of the mathematical models describing the dynamics of how a disease spreads is the well known SEIR model [56, 57]. We will follow Schwartz and Smith [56] in making the following definitions and assumptions which are illustrated in Fig. 2.14. Assume a given population may be divided into following groups:

- Susceptible - those capable of contracting the disease

- Exposed - those who are infected but not yet infective

- Infective - those capable of transmitting the disease

- Recovered - those who are immune.

In addition, suppose:

1. The population consists of those who are susceptible, infected but not yet infective, infective, and immune. The population size is constant.

2. The disease is not lethal; equal and constant birth and death rates μ are assumed.

3. The population is homogeneous and uniformly mixed.

4. The contact rate, κ, is defined as the average number of effective contacts with other individuals per infective per unit time.
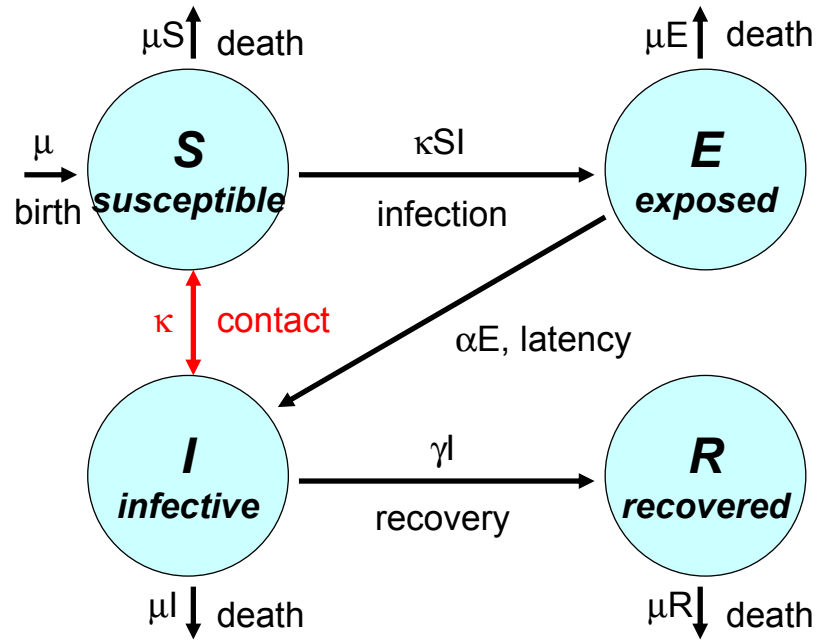
Figure 2.14: The schematic diagram of SEIR model.

5. An exposed individual becomes infective with the mean latent period described by $1/\alpha$.

6. An infective individual recovers with the mean infective period described by $1/\gamma$, and γ is called the recovery rate.

7. Recovered individuals are permanently immune.

Letting S, E, I, R denote respectively the fractions of the population that are susceptible, exposed, infective, and recovered, the above assumptions lead to the

following equations:

$$\frac{dS}{dt} = \mu - \mu S - \kappa I S, \tag{2.27}$$

$$\frac{dE}{dt} = \kappa I S - (\mu + \alpha)E, \tag{2.28}$$

$$\frac{dI}{dt} = \alpha E - (\mu + \gamma)I, \tag{2.29}$$

$$\frac{dR}{dt} = \gamma I - \mu R. \tag{2.30}$$

Since $S+E+I+R = 1$, the first three equations are sufficient to describe the dynamics. Eqn. 2.27- 2.30 have two steady steady states: $(1,0,0,0)$ and (S_0, E_0, I_0, R_0), where

$$S_0 = \frac{(\mu + \alpha)(\mu + \gamma)}{\kappa \alpha}, \tag{2.31}$$

$$E_0 = \frac{(\mu + \gamma)I_0}{\alpha}, \tag{2.32}$$

$$I_0 = \frac{\mu(Q - 1)}{\kappa}, \text{ where } Q = 1/S_0. \tag{2.33}$$

The latter state is practically meaningful for $Q > 1$. An infective disease can be endemic only if Q, which is called the reproductive rate of infection, exceeds unity.

Refs. [56, 60] show that for almost all cases, the infective and exposed populations follow each other in time to first order, i.e.,

$$I(t) = \left(\frac{\alpha}{\mu + \gamma}\right) E(t) + O(\epsilon), \tag{2.34}$$

for some small parameter ϵ. Therefore, the SEIR model can be reduced to two equations, the so called modified SI model (MSI), given by

$$\frac{dS}{dt} = \mu - \mu S - \kappa I S, \tag{2.35}$$

$$\frac{dI}{dt} = \left(\frac{\alpha}{\mu + \gamma}\right) \kappa I S - (\mu + \alpha)I. \tag{2.36}$$

30

In the previous section, the dynamics of the laser population were described by Eqns. 2.9 - 2.11 with Eqn. 2.12, which can be rewritten after we redefine $(N - N_0) \rightarrow N$ and $(I/q - \gamma_e N_0) \rightarrow R_p$,

$$\frac{dP}{dt} = G_N N P - \gamma_p P, \tag{2.37}$$

$$\frac{dN}{dt} = R_p - \gamma_e N - G_N N P, \tag{2.38}$$

where ϵ is assumed to be zero and R_p is the pump rate. Billings et al. showed the similarities between a class of epidemic models described by Eqn. 2.35, 2.36 and a class of the laser models, analytically and topologically [54]. The dynamics of both systems are described by two variables, i.e., one slow variable and one fast variable, and they are coupled by nonlinear interaction whose strength is proportional to the product of two variables. Both systems have constant input sources to the dynamics of the slow variable and each variable decays at a constant rate. Table 2.2 summarizes the correspondences between the two systems.

Description of dynamical variables and parameters	Epidemic model	Laser model
Slow dynamical variable	S, Susceptible population	N, Carrier number
Fast dynamical variable	I, Infective population	P, Photon number
Source term	μ, Susceptible input rate	R_p, Pump rate
Nonlinear coupling	κ, Contact rate	G_N, Gain coefficient

Table 2.2: Correspondences between a single population epidemic model and a standard laser model

The similarities between the mathematical model of the epidemic population dynamics and a laser model encouraged us to perform simple but interesting experiments with two cross-coupled lasers, the details of which will be described in the following chapter. Our experimental approach to the coupled population model has a very important advantage when combined with numerical and analytical studies for the investigation of the long-term dynamics of the system. It is highly effective in revealing instabilities and investigating long time scale dynamics over a wide range of parameters.

Studying this system provides insight into the effect of migratory time delays between coupled populations on the appearance of outbreaks of disease. The inclusion of an effective delay in the transmission of disease between populations possibly explains some of the interesting dynamical phenomena observed for disease epidemics, including long inter-epidemic periods and in-phase oscillations of incidence [61, 62].

In Chapter 3, we will present the experimental results from a system consisting of two semiconductor lasers cross-coupled opto-electronically with a time delay, as well as the results from numerical simulations.

Chapter 3

Cross-coupled Lasers with Negative Optoelectronic Time-delayed
Coupling

3.1 Experimental Setup

3.1.1 Optoelectronic Loop

In this section, the experimental implementation of cross-coupled semiconductor
lasers with negative optoelectronic time-delayed coupling will be described. Fig.3.1
shows a schematic diagram of the system. Light emitted from one laser diode (LD)
passes through single mode optical fiber and is monitored by a photodiode detector
(PD). The AC signal of the photodetector (V) is amplified or attenuated and then
negatively fed back into the RF input of the other laser.

The light sources are two 1550 nm wavelength distributed feedback (DFB)
laser diodes whose basic operations are described in Sec. 2.4. Both lasers are
operated at slightly above the threshold, 9.3 mA for LD1 and 12.0 mA for LD2.
The characteristic relaxation oscillation time of the laser dynamics is $\sim 1\ ns$ for this
level of injection current.

Fig.3.2 shows the optical path in detail. Each laser has a polarization main-
taining single mode fiber pigtail, 1.4 m in length, terminated with a FC connector.
To avoid back reflections, a fiber optic isolator (Gould Fiber Optics, ISOL-D-P-55-
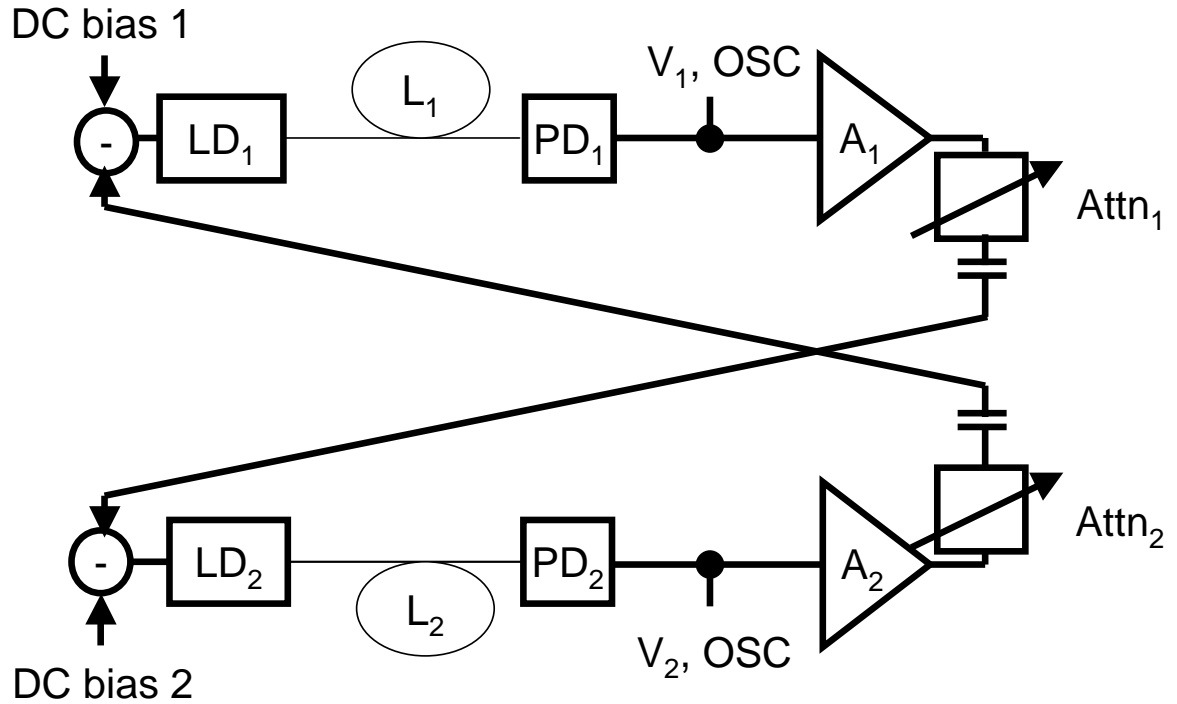
Figure 3.1: Schematic diagram of the cross-coupled laser experiment with delayed negative opto-electronic feedback. LD_1 and LD_2: laser diodes; PD_1 and PD_2: photodiodes; L_1 and L_2: optical fibers; OSC: oscilloscope; V_1 and V_2: photodiode output voltages; A_1 and A_2: electronic amplifiers; $Attn_1$ and $Attn_2$: variable electronic attenuators. The thin lines indicate the optical signal path through the fiber and the
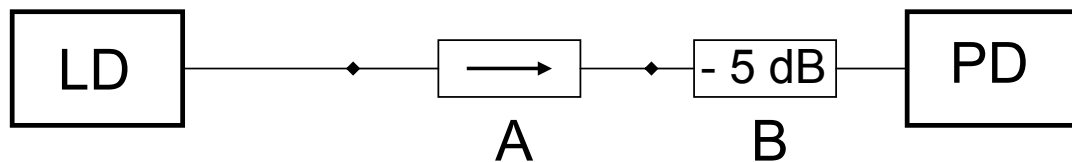
Figure 3.2: The detailed illustrations of the optical path. LD: a laser diode; A: a fiber optic isolator; B: a 5 dB inline attenuator; PD: a photodetector.

BB-103, 50 dB isolation) with a 1 m lead is inserted. A 5 dB inline attenuator, 1 m in length, is used to reduce the total optical power(FIS) at the photodiode. Each fiber is terminated with a FC/PC (Physical Contact polish resulting in back reflections of -30 to -40 dB) connector and a FC mating sleeve is used at each contact point on optical path. Additional fiber components of different lengths can be inserted between the isolator and the photodiode detector.

The electronic path is shown schematically in Fig.3.3. The part numbers of the electronic components are given in the figure caption. The photodiode detector (labelled A in Fig.3.3) produces a voltage proportional to the power fluctuations of the light. Half of the signal is split by a power splitter (B in Fig.3.3) and sent to a digital oscilloscope (Tektronix, TDS7104, 1 GHz, 10 GS/s) to monitor the system. The other half of the signal is sent to a low-noise, fixed-gain amplifier (C in Fig.3.3), a fixed attenuator (D in Fig.3.3), variable attenuators (E and F in Fig.3.3), and a DC-blocking capacitor ($0.22\mu F$, Picosecond Pulse Labs 5501A). The capacitor, i.e., DC block, is a high pass filter which reduces the gain at frequencies below 7 kHz. This signal will be sent to the RF input of the other laser to modulate the injection current. The polarity of the coupling is negative meaning that an increase in the light power of LD_1 reduces the light power of the LD_2 after the propagation delay time, and vice versa.

The optoelectronic feedback loop gives a system with an inherent delay that can be easily modified by inserting optical fibers of different length into the optical path. Without additional fiber components in the optical path, the delay time from one laser to the other laser is fixed at ~ 35 ns for the experiments presented in

35
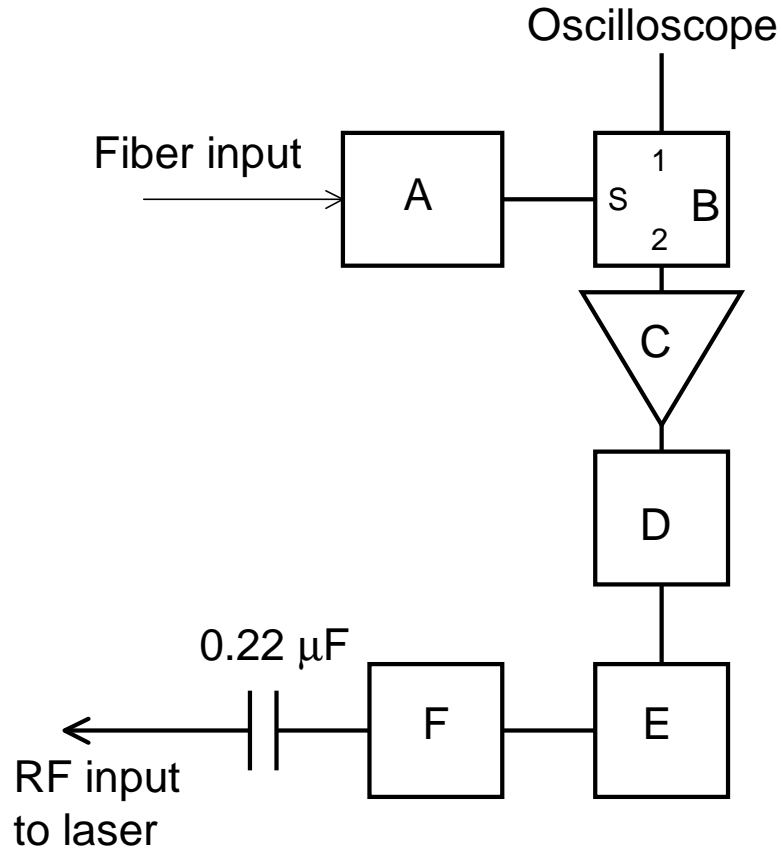
Figure 3.3: Schematic diagram of the electronic path. The components labelled A-F are as follows: A - New Focus photodetector 1611 (30k - 1 GHz); B - Mini-Circuits power splitter ZFSC-2-4 (.1 - 1000 MHz); C - Mini-Circuits amplifier ZFL-1000LN (.1 - 1000 MHz, + 18 dB); D - Mini-Circuits fixed attenuator; E - Pasternack 1 dB step attenuator PE7034-3 (DC - 2 GHz); F - Pasternack .1 dB step attenuator PE7034-1 (DC - 1 GHz).

Chapter 3, which is much longer than the characteristic relaxation oscillation time of the laser dynamics, $\sim 1 \ ns$. The coupling strengths are controlled separately with variable attenuators on the electronic path while all the other parameters are matched as closely as possible for the two coupled lasers.

3.1.2 Gain Measurements

To quantify the coupling strength from one laser to the other, the open loop gain of each path is measured, as shown in Fig. 3.4. Assuming that the default gain for each direction is constant for a sinusoidal input with any amplitude and frequency, we measure the ratio of the output signal amplitude to the input signal amplitude and define this as the coupling strength. The default linear gain from LD_1 to LD_2, d_{10}, and that from LD_2 to LD_1, d_{20}, can be given by

$$d_{10} = \frac{V_{out,1}}{V_{in,1}} \quad \text{and} \quad d_{20} = \frac{V_{out,2}}{V_{in,2}}. \tag{3.1}$$

The default gains in dB [decibel] unit, g_{10} and g_{20}, are defined by

$$g_{10} \ [dB] \ = \ 20 \ log_{10}\left(\frac{V_{out,1}}{V_{in,1}}\right) \ = \ 20 \ log_{10}(d_{10}), \tag{3.2}$$

$$g_{20} \ [dB] \ = \ 20 \ log_{10}\left(\frac{V_{out,2}}{V_{in,2}}\right) \ = \ 20 \ log_{10}(d_{20}). \tag{3.3}$$

Fig. 3.5 shows plots obtained from the open loop gain measurements where the sinusoidal wave at 10 MHz is used as the input signal. The time series is taken for 0.2 ms at 2.5 GS/s resolution. The standard deviation of the signal is used as the signal amplitude and the average default gains are $g_{10} = 8.0192$ and $g_{20} = 7.2150$ in decibels.
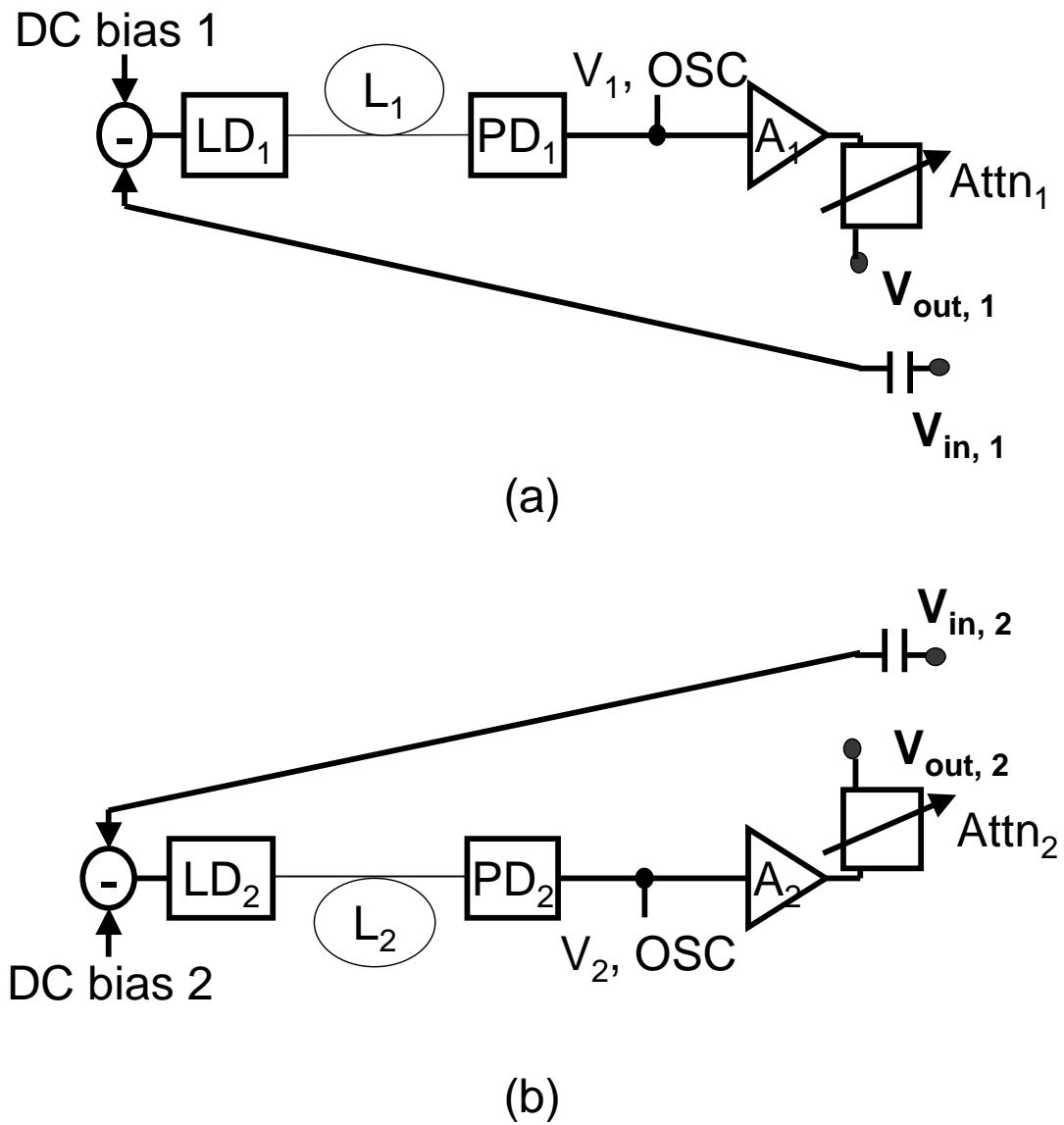
Figure 3.4: The schematic diagram for open loop gain measurements. (a) To measure the default gain from LD_1 to LD_2, d_{10}, and (b) the default gain from LD_2 to LD_1, d_{20}. For both cases, step attenuators are at zero attenuation level.
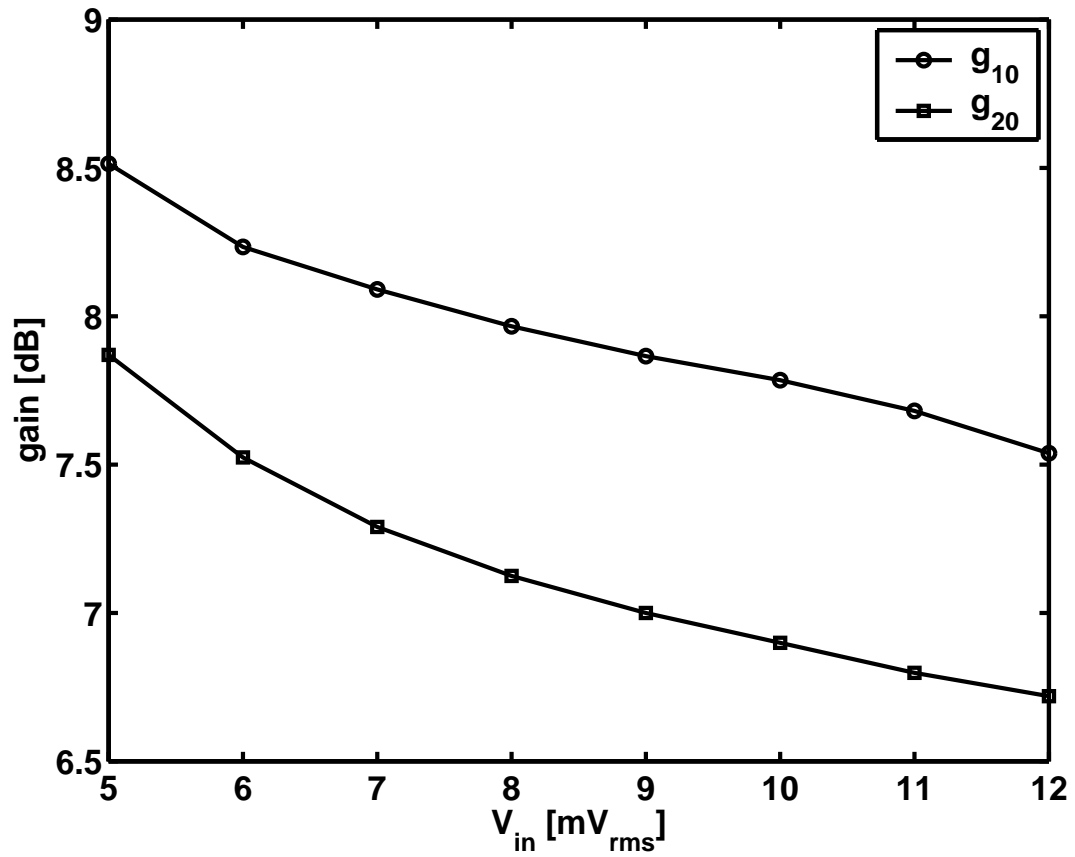
Figure 3.5: The open loop gain measurements. The default gain in [dB] unit from LD$_1$ to LD$_2$, g_{10}, and that from LD$_2$ to LD$_1$, g_{20}, are calculated for the sinusoidal input at 10 MHz in linear response regime.

For the experimental results presented in following section, the attenuation level in each direction, g_1 and g_2 (in dB unit), will be controlled asymmetrically, and the net gains are defined as

$$d_1 = 10^{(g_{10}+g_1)/20}, \tag{3.4}$$

$$d_2 = 10^{(g_{20}+g_2)/20}. \tag{3.5}$$

3.2 Experimental Observations and Analysis

In this section, the coupling strengths, d_1 and d_2, will be used as control parameters. For the fixed value of coupling strength d_1, d_2 is varied in the experiments. As the coupling is made stronger, the emergence of sinusoidal oscillations of the laser outputs is observed with growing amplitude thereafter. We study the influence of asymmetric coupling on the onset of the oscillations and discover a scaling law between the amplitudes of oscillations and the coupling strengths [63].

3.2.1 Emergence of Oscillations

Fig. 3.6 shows the typical evolution of system at different coupling strengths. For weak coupling, both lasers show noisy fluctuations in the signal intensity. As the coupling strength d_2 is made stronger, the emergence of the periodic oscillations is observed. It is seen that the oscillating signals from each laser are in phase and that the period of the oscillations is twice the delay time, ~ 70 ns. Intuitively, when the light intensities of both lasers stay high during half of the oscillation period, the output of both will be reduced by the feedback after the propagation time delay and stay low for the rest of the oscillation. Then after another propagation delay time has elapsed, the output of both will increase and stay high. Therefore, the in-phase oscillations with a period of twice the time delay becomes stable.

In Fig. 3.7, the amplitude of the signal measured by PD versus the coupling strength d_2 is shown for different values of the coupling strength d_1. For each set of parameters (d_1, d_2), the time series is recorded for time windows of 0.4 ms at 2.5
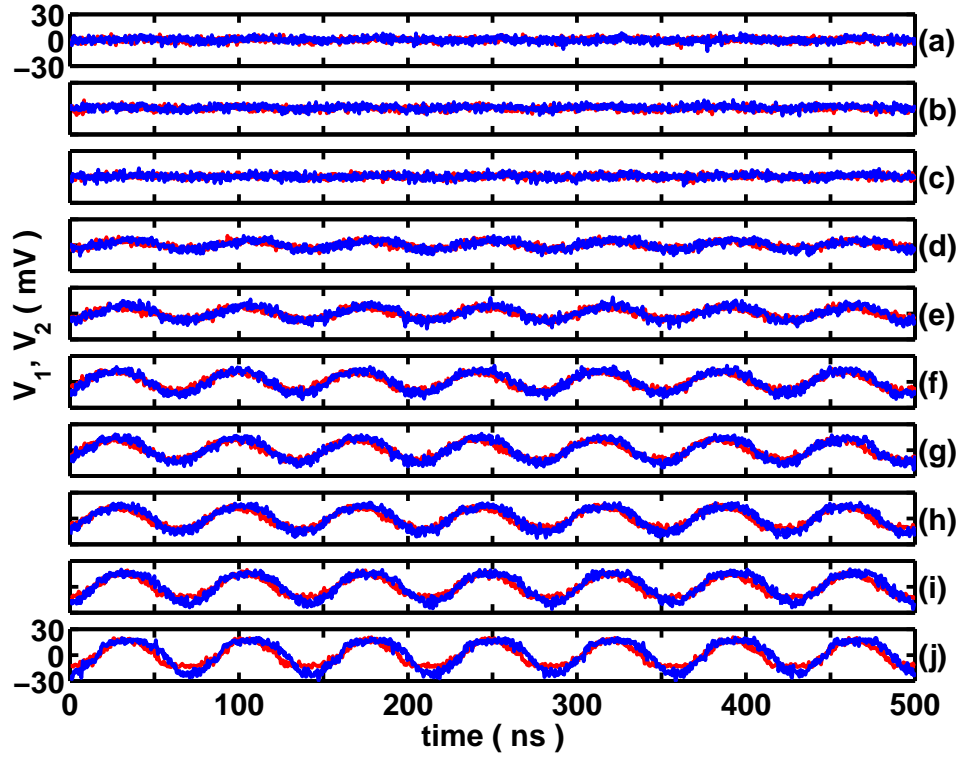
Figure 3.6: Emergence of the periodic oscillations. Time series are taken for $d_1 = 1.12$, and (a) $d_2 = 1.09$, (b) $d_2 = 1.10$, (c) $d_2 = 1.11$, (d) $d_2 = 1.12$, (e) $d_2 = 1.14$, (f) $d_2 = 1.15$, (g) $d_2 = 1.16$, (h) $d_2 = 1.18$, (i) $d_2 = 1.19$, and (j) $d_2 = 1.20$. Red dots are the time series taken from PD_1 (V_1) which is proportional to the light intensity fluctuations in LD_1, and blue dots are the time series taken from PD_2 (V_2) which is proportional to the light intensity fluctuations in LD_2.

giga samples per second (GS/s). Each time series is divided into 10 sub-windows and the standard deviations of the signals in each sub-window is calculated. The average of the standard deviation is used as the signal amplitude. For the parameter range shown in Fig. 3.7, the light intensities from both lasers oscillate in-phase with each other, and the period of the oscillations is double the delay time (not shown).

3.2.2 Onset of Oscillations

As shown in Fig. 3.7, even when the coupling in one direction is weak, the system starts oscillating if the coupling in other direction is strong enough. In other words, as the coupling strength d_1 is made stronger, the periodic oscillations emerge at smaller values of d_2. To obtain a quantitative relationship between the coupling strengths at the onset of the oscillations, the values of $log_{10}(d_1)$ and $log_{10}(d_2)$ are plotted at the onset. It is found that these points fall on a straight line, satisfying a linear relation given by

$$log_{10}(d_1) + log_{10}(d_2) = log_{10}(d_1 d_2) = c, \tag{3.6}$$

as shown in Fig. 3.8, where $c \sim 0.1$ from the best-fit linear model. A condition for the onset of the oscillation, therefore, is that the product of d_1 and d_2 increases through a critical constant, i.e., $d_1 d_2 = 10^{0.1} = 1.3$, in this case.

3.2.3 Scaling Behavior

Since the product of the coupling strengths, $d_1 d_2$, seems to serve as a control parameter, there arises a question of whether we can rescale the variables, V_1 and V_2,
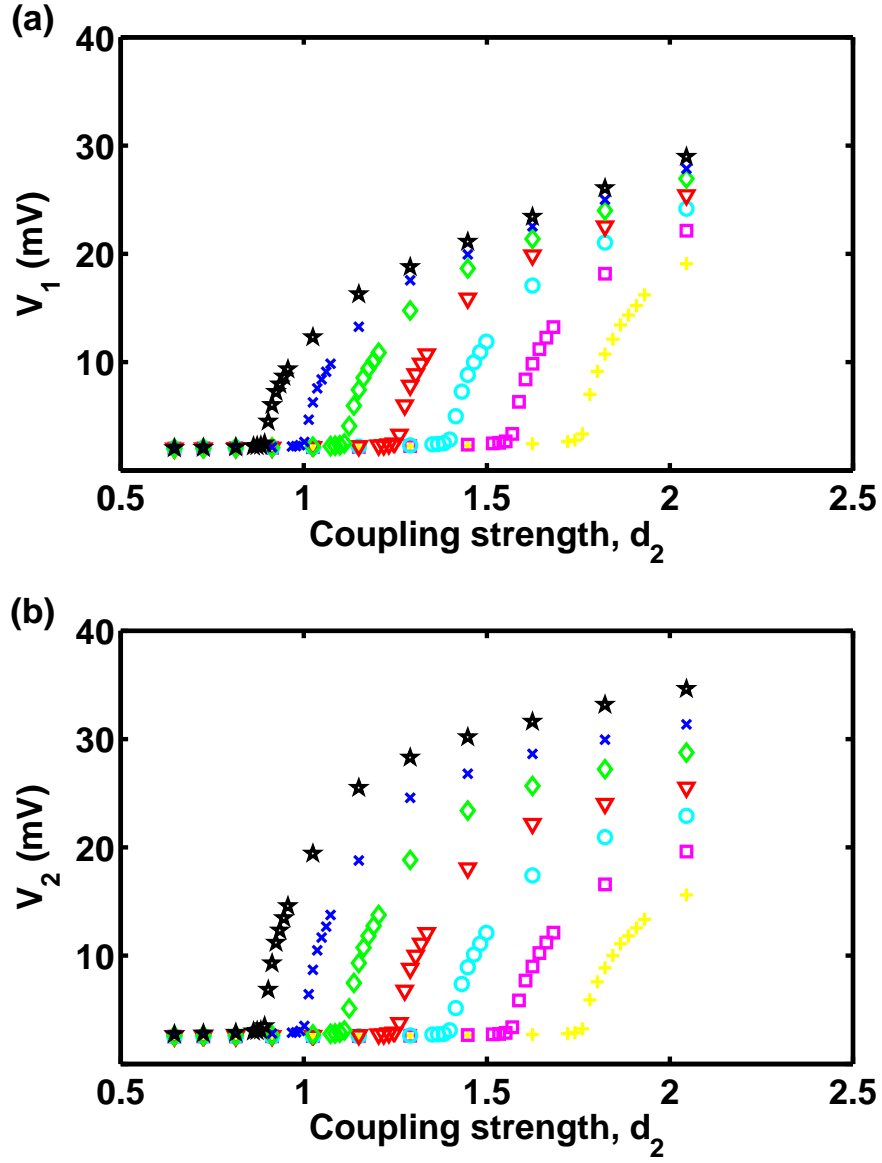
Figure 3.7: Plot of intensity oscillation amplitude measured by (a) PD_1, V_1, and by (b) PD_2, V_2, versus coupling strength d_2 for different coupling strengths d_1. Plus signs show the amplitude for $d_1 = 0.71$; Squares for $d_1 = 0.80$; Circles for $d_1 = 0.89$; Triangles for $d_1 = 1.00$; Diamonds for $d_1 = 1.12$; Crosses for $d_1 = 1.26$; Stars for $d_1 = 1.42$ [63].
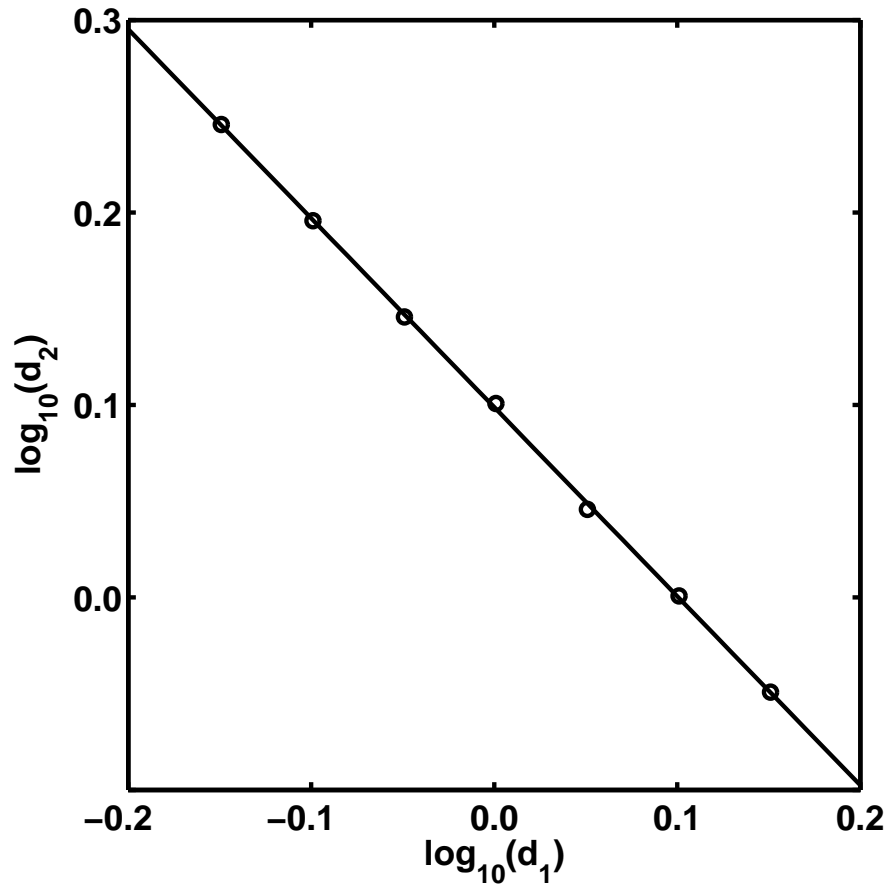
Figure 3.8: Plot of log_{10}(coupling strength d_2) versus log_{10}(coupling strength d_1) at the emergence of oscillations. The line shows the best-fit linear model [63].
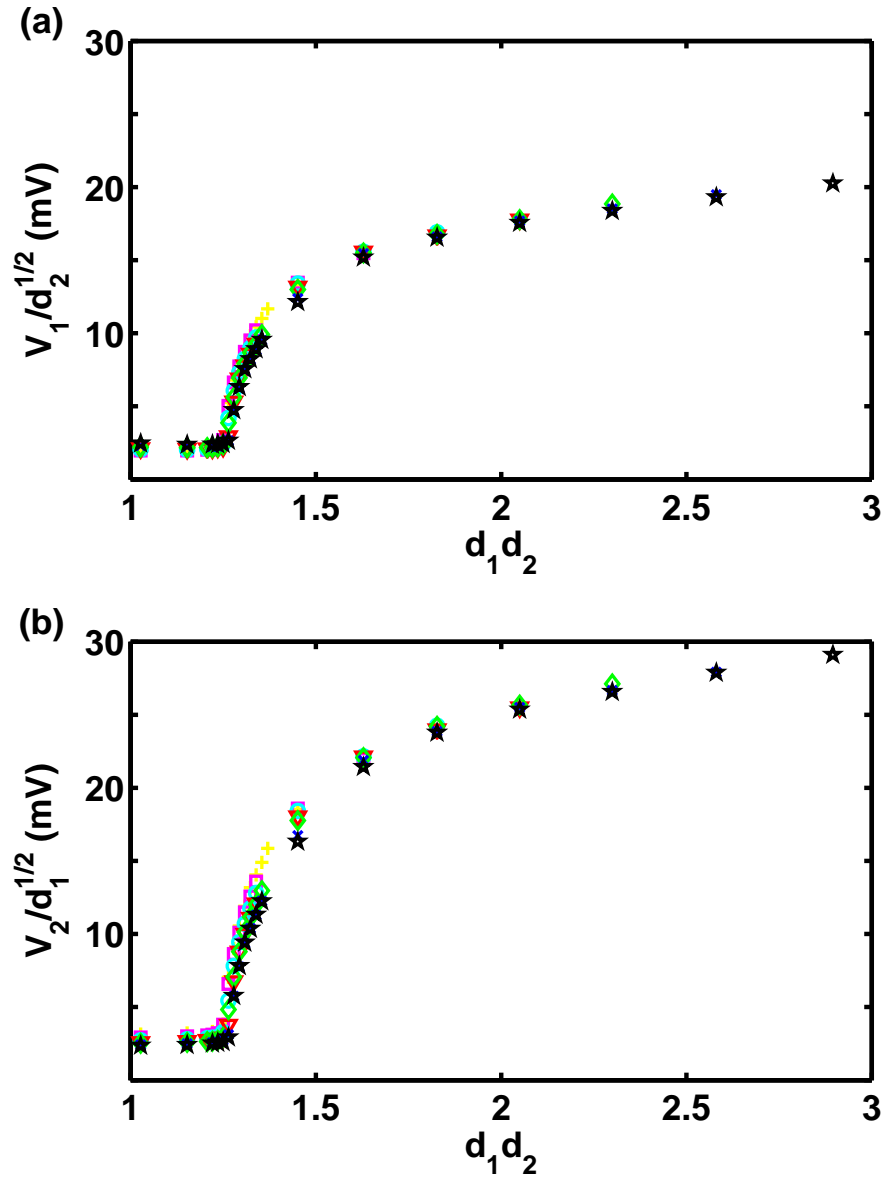
Figure 3.9: Plot of rescaled intensity amplitudes versus the product of coupling strengths. (a) $V_1/\sqrt{d_2}$ vs. $(d_1 d_2)$. (b) $V_2/\sqrt{d_1}$ vs. $(d_1 d_2)$. Same marker types are used for same d_1 values as in Fig. 3.7. This shows data collapse [63].
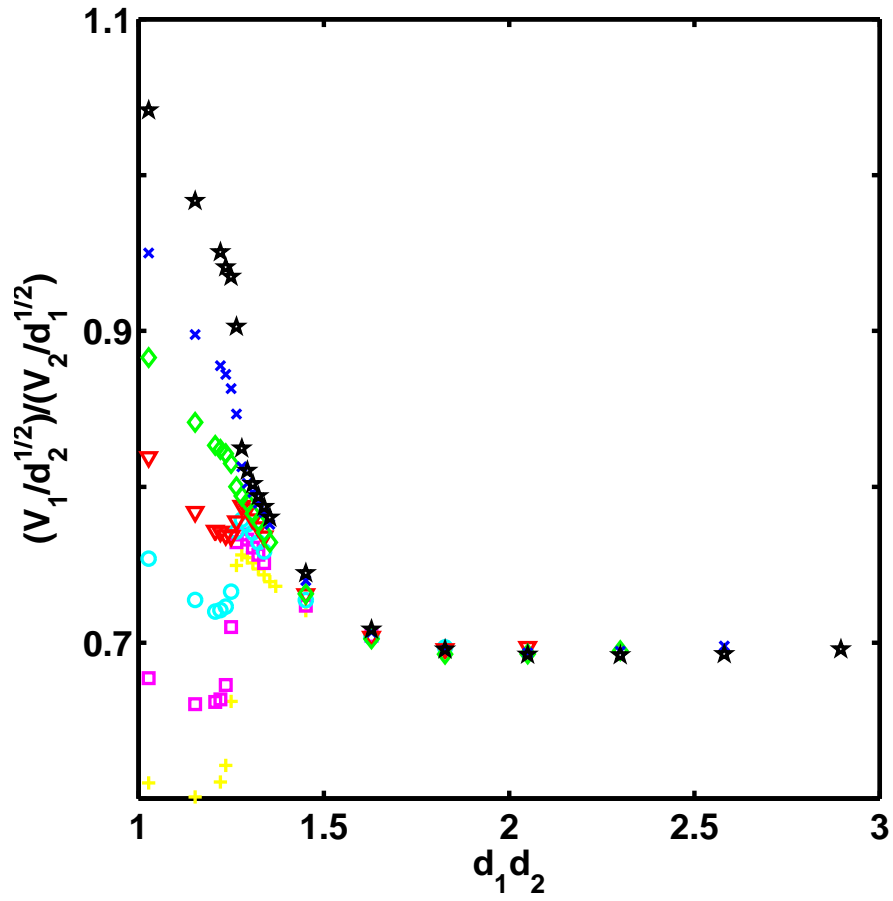
Figure 3.10: Plot of the ratio of the rescaled amplitudes $(V_1/\sqrt{d_2})/(V_2/\sqrt{d_1})$ versus $(d_1 d_2)$. Same marker types are used for same d_1 values as in Fig. 3.7 [63].

so that we can discover a scaling law that relates the amplitudes of oscillations and the coupling strengths.

Fig. 3.9 shows the plots of the rescaled amplitude of the oscillations, $V_1/\sqrt{d_2}$ and $V_2/\sqrt{d_1}$, versus $(d_1 d_2)$. As a result, the individual curves corresponding to different coupling strengths d_1 in Fig. 3.7 collapse to a single curve for each rescaled amplitude.

In Fig. 3.10, the ratio of rescaled amplitudes, i.e., $(V_1/\sqrt{d_2})/(V_2/\sqrt{d_1})$, is plotted as a function of $(d_1 d_2)$. When the product $(d_1 d_2)$ increases beyond the critical value 1.3, the ratio converges to a constant and periodic oscillations appear in both systems. This result implies that there exists, to a good approximation, a single function that determines the amplitudes of oscillations in both lasers for given coupling strengths.

In the following section, the mathematical model for the cross-coupled laser systems is derived and stability analysis near the onset of oscillations is carried out.

3.3 Mathematical Model for Coupled Lasers

3.3.1 Dimensionless Rate Equations

In this section, we rewrite the rate equations for the laser, Eqns. 2.9 - 2.11, in terms of rescaled variables

$$N' = \frac{G_N}{\gamma_p}(N - N_0) \ , \ \ P' = \frac{G_N}{\gamma_e}P \ \ \text{and} \ \ t' = \gamma_p t. \tag{3.7}$$

After rewriting the primed variables as unprimed variables, the equations are given by

$$\frac{dP(t)}{dt} = (N(t) - 1)P(t), \tag{3.8}$$

$$\frac{dN(t)}{dt} = \epsilon^2[A - (1 + P(t))N(t)], \tag{3.9}$$

with

$$\epsilon^2 = \frac{\gamma_e}{\gamma_p} \ \text{and} \ A = \frac{G_N}{\gamma_e\gamma_p}\left(\frac{I}{q} - \gamma_e N_0\right), \tag{3.10}$$

where ϵ^2 is the ratio of the carrier decay rate to the the photon decay rate, and A is proportional to the injection current above transparency, $(I - I_0)$.

Since we use the signal proportional to the photon intensity fluctuations from one laser to modulate the injection current of the other laser, we define new variables for the fluctuations from the steady states as

$$P_j = P_{j0}(1 + y_j) \ , \ \ N_j = 1 + \epsilon_j\sqrt{P_{j0}} \, x_j \ , \ \ \text{and} \ s = \epsilon_1\sqrt{P_{10}} \, t, \tag{3.11}$$

and the pump coupling is denoted as $A_j(t) = A_{j0} - P_{j0}\epsilon\delta_k y_k(t - \tau_k)$ with delay time τ_k and coupling constant δ_k. The subscript 0 refers to the steady state level without

coupling. The index $j = 1, 2$ corresponds to LD_1 and LD_2, respectively, whereas the index $k = 2, 1$ corresponds to LD_2 and LD_1. The new equations are

$$\frac{dy_1}{dt} = x_1(1 + y_1), \tag{3.12}$$

$$\frac{dx_1}{dt} = -y_1 - \epsilon x_1(a_1 + by_1) - \epsilon\delta_2 y_2(t - \tau_2), \tag{3.13}$$

$$\frac{dy_2}{dt} = \beta x_2(1 + y_2), \tag{3.14}$$

$$\frac{dx_2}{dt} = \beta[-y_2 - \epsilon\beta x_2(a_2 + by_2) - \epsilon\delta_1 y_1(t - \tau_1)], \tag{3.15}$$

where

$$\frac{\epsilon_2\sqrt{P_{10}}}{\epsilon_1\sqrt{P_{20}}} \equiv \beta \ , \ s \to t \ , \ \epsilon_1 \to \epsilon,$$

$$a_1 = \frac{1 + P_{10}}{\sqrt{P_{10}}}, \ a_2 = \frac{\sqrt{P_{10}}(1 + P_{20})}{P_{20}}, \ b = \sqrt{P_{10}}, \ \beta = 1 + \epsilon\alpha.$$

x_j and y_j ($j = 1, 2$) are the normalized intensity fluctuations and the scaled carrier number fluctuations for each laser. The coupling constants δ_1 and δ_2 are proportional to the coupling strengths d_1 and d_2 from the experiments. The time used in the equations is scaled so that

$$t \ [\text{dimensionless}] = 2\pi \frac{t_{\text{physical}}}{T_{\text{relaxation}}} \tag{3.16}$$

where t_{physical} is the real time in seconds and $T_{\text{relaxation}}$ is the period of the relaxation oscillations in seconds.

For the coupled identical lasers, the equations above can be simplified as

$$\frac{dy_1}{dt} = x_1(1 + y_1), \tag{3.17}$$

$$\frac{dx_1}{dt} = -y_1 - \epsilon x_1(a + by_1) - \epsilon \delta_2 y_2(t - \tau), \tag{3.18}$$

$$\frac{dy_2}{dt} = x_2(1 + y_2), \tag{3.19}$$

$$\frac{dx_2}{dt} = -y_2 - \epsilon x_2(a + by_2) - \epsilon \delta_1 y_1(t - \tau), \tag{3.20}$$

where $a = (1 + P_{10})/\sqrt{P_{10}}$ and $b = \sqrt{P_{10}}$.

3.3.2 Linear Stability Analysis

The steady state for Eqns. 3.17 - 3.20 is given by $(y_{10}, x_{10}, y_{20}, x_{20}) = (0, 0, 0, 0)$.
Since we are interested in the bifurcation of dynamics from steady state to periodic
state, we apply linear stability analysis to study the evolution of small perturbations
around the steady state as the coupling constants are increased. By linearizing
Eqns. 3.17 - 3.20, we obtain

$$\frac{dy_1}{dt} = x_1, \tag{3.21}$$

$$\frac{dx_1}{dt} = -y_1 - a\epsilon x_1 - \epsilon \delta_2 y_2(t - \tau), \tag{3.22}$$

$$\frac{dy_1}{dt} = x_2, \tag{3.23}$$

$$\frac{dx_2}{dt} = -y_2 - a\epsilon x_2 - \epsilon \delta_1 y_1(t - \tau). \tag{3.24}$$

We assume that all variables vary periodically in time with same angular frequency,
ω, i.e.,

$$y_i, \ x_i \ \sim e^{i\omega t}. \tag{3.25}$$

Then Eqn. 3.21 - Eqn. 3.24 can be rewritten as

$$
i\omega \begin{pmatrix} y_1 \\ x_1 \\ y_2 \\ x_2 \end{pmatrix} = \begin{pmatrix} 0 & 1 & 0 & 0 \\ -1 & -a\epsilon & -\epsilon\delta_2 e^{-i\omega\tau} & 0 \\ 0 & 0 & 0 & 1 \\ -\epsilon\delta_1 e^{-i\omega\tau} & 0 & -1 & -a\epsilon \end{pmatrix} \begin{pmatrix} y_1 \\ x_1 \\ y_2 \\ x_2 \end{pmatrix}, \tag{3.26}
$$

or,

$$
\begin{pmatrix} -i\omega & 1 & 0 & 0 \\ -1 & -a\epsilon - i\omega & -\epsilon\delta_2 e^{-i\omega\tau} & 0 \\ 0 & 0 & -i\omega & 1 \\ -\epsilon\delta_1 e^{-i\omega\tau} & 0 & -1 & -a\epsilon - i\omega \end{pmatrix} \begin{pmatrix} y_1 \\ x_1 \\ y_2 \\ x_2 \end{pmatrix} = 0. \tag{3.27}
$$

For nontrivial solutions to exist, the determinant of matrix shown in the left hand side (LHS) of Eqn. 3.27 must be zero. The characteristic equation is given by

$$
\left[i\omega(a\epsilon + i\omega) + 1 \right]^2 - \epsilon^2 \delta_1 \delta_2 e^{-2i\omega\tau} = 0, \tag{3.28}
$$

where the real part and the imaginary part can be separated, i.e.,

$$
\text{Re} \quad : \quad (\omega^2 - 1)^2 - (a\epsilon\omega)^2 = \epsilon^2 \delta_1 \delta_2 \cos(2\omega\tau), \tag{3.29}
$$

$$
\text{Im} \quad : \quad 2a\epsilon\omega(\omega^2 - 1) = \epsilon^2 \delta_1 \delta_2 \sin(2\omega\tau). \tag{3.30}
$$

For the injection current level not far from threshold, the LHS of Eqn. 3.29 remains positive while that of Eqn. 3.30 changes sign at $\omega = 1$, such that

$$
\cos(2\omega\tau) > 0 \text{ and } \sin(2\omega\tau) < 0 \quad \text{for} \quad \omega < 1, \tag{3.31}
$$

$$
\cos(2\omega\tau) > 0 \text{ and } \sin(2\omega\tau) > 0 \quad \text{for} \quad \omega > 1. \tag{3.32}
$$

In other words, the argument $(2\omega\tau)$ stays in 4th quadrant for $\omega < 1$, and in 1st quadrant for $\omega > 1$.

Eqn. 3.29 and Eqn. 3.30 can be rewritten for the convenience. By adding the square of Eqn. 3.29 and that of Eqn. 3.30, we have

$$\left[(\omega^2 - 1)^2 + (a\epsilon\omega)^2\right]^2 = (\epsilon^2\delta_1\delta_2)^2, \tag{3.33}$$

and by dividing Eqn. 3.30 by Eqn. 3.29, we obtain

$$\frac{2a\epsilon\omega(\omega^2 - 1)}{(w^2 - 1)^2 - (a\epsilon\omega)^2} = \tan(2\omega\tau). \tag{3.34}$$

For $\epsilon \ll 1$, Eqn. 3.33 can be approximated to the leading order in ϵ as

$$(\omega^2 - 1)^2 = 0 \text{ , i.e., } \omega = \pm 1. \tag{3.35}$$

This solution corresponds to the relaxation oscillations. By substituting $\omega = \pm 1$ in Eqn. 3.33, we have

$$a^2\epsilon^2 = \epsilon^2|\delta_1\delta_2|. \tag{3.36}$$

Assuming the same sign for δ_1 and δ_2, the onset condition for the solution $\omega = \pm 1$ is, therefore, given by

$$\delta_1\delta_2 = a^2. \tag{3.37}$$

Now, we will consider the case of $\omega \ll 1$, which corresponds to our experimental observations. To the leading order in ω, Eqn. 3.33 and Eqn. 3.34 are approximated by

$$1 = (\epsilon^2\delta_1\delta_2)^2 \tag{3.38}$$

$$-2a\epsilon\omega = \tan(2\omega\tau). \tag{3.39}$$
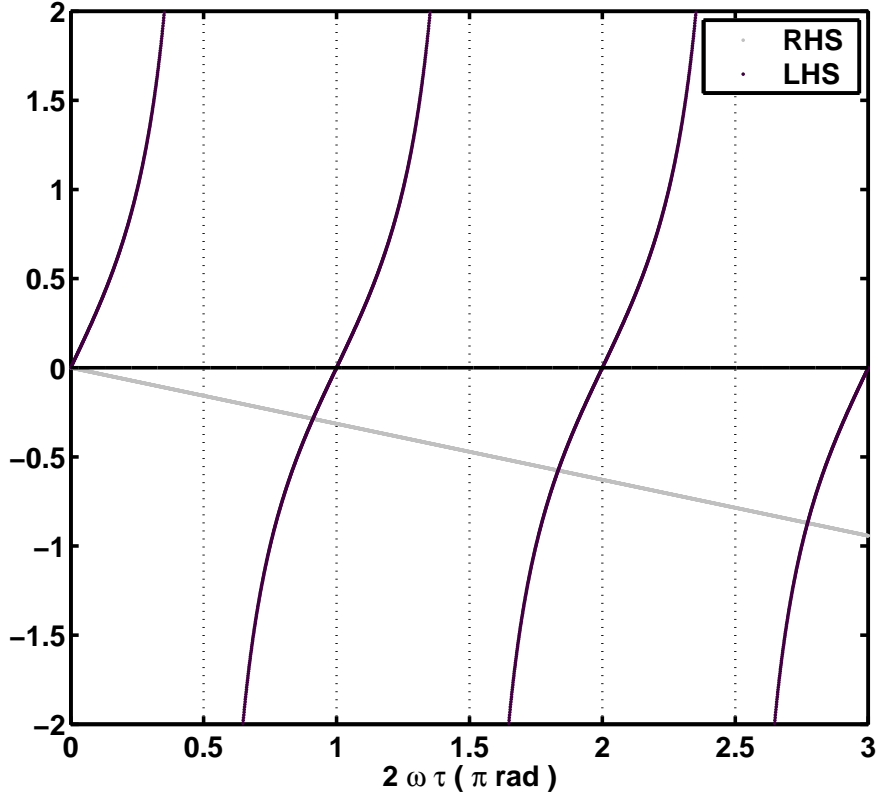
Figure 3.11: Plot of the left hand side (LHS) and the right hand side (RHS) of Eqn. 3.39 as a function of argument $(2\omega\tau)$. The slope of LHS is given by $-a\epsilon/\tau$ and the numerical value of -0.1 is used for above plot.

Again, assuming the same sign for coupling constants, Eqn. 3.38 gives the onset condition, i.e.,

$$\delta_1\delta_2 = \epsilon^{-2}. \tag{3.40}$$

In Fig. 3.11, the left hand side and the right hand side of Eqn. 3.39 are plotted as a function of argument $(2\omega\tau)$, for $a\epsilon/\tau = 0.1$. As the delay time τ gets longer, the slope becomes small and the line approaches the horizontal axis. As a result, the intersection points can be approximated by $2\omega\tau = n\pi$ with an integer n. Since

54

the solution of Eqn. 3.39 must stay in 4th quadrant for $\omega < 1$, n has to be an even number. The angular frequency of the periodic solution is, therefore, given by

$$\omega_m = \frac{2m\pi}{2\tau} = \frac{2\pi}{T_m} \quad \text{with } m = 1, 2, 3, 4, \ \ldots, \tag{3.41}$$

where the period T_m is given by $2\tau/m$. The fundamental period of the system, corresponding to $m = 1$, is double the delay time τ.

In summary, for the fixed value of the delay time, τ, there is the internal mode described by $\omega = \pm 1$ and an infinite number of external modes described by $\omega_m = m(2\pi)/(2\tau)$ with an integer m. For the internal mode, the periodic bifurcation occurs at $\delta_1\delta_2 = a^2$. In case of the external modes, the periodic bifurcation occurs at $\delta_1\delta_2 = \epsilon^{-2}$.

According to the onset conditions, the internal mode has a smaller value of $\delta_1\delta_2$ and so the internal mode will bifurcate first. This is the case which is shown in the following section where the numerical simulations of Eqn. 3.17 - Eqn. 3.20 are carried out. While an infinite-bandwidth photodetector and amplifier response is assumed in the numerical simulations, there exist the finite response of electronic components in the experiments. Our experimental observations show the bifurcation of external mode with the fundamental period. By adding an additional ordinary differential equation for the low pass filter, we can show the emergence of external modes in the numerical simulations.

3.4 Numerical Simulations

In order to verify the experimental observations of the cross-coupled semiconductor lasers, we integrate Eqn. 3.17 through Eqn. 3.20 using a standard fourth order Runge-Kutta method. We consider the case $a = 2$, $b = 1$ and $\epsilon = \sqrt{0.001}$ with $\tau = 30$. In other words, the injection current level is double the threshold level and the ratio of the delay time to the relaxation oscillation period is around 5. Even if these numerical values do not exactly match the experimental values, the model still shows similar rescaling behavior with related onset conditions. We will also look at the rescaling property for $\tau = 150$. The effect of the low pass filter along the electronic path will be considered numerically at the end of this section.

3.4.1 Numerical Observations of Instability without Filter

Fig. 3.12 shows the typical evolution of the time series as the coupling constant δ_2 is made stronger for a fixed coupling constant δ_1. The periodic oscillations emerge as the coupling constant δ_2 increases and the light intensities from each laser oscillate anti-phase with each other. The period of the oscillations corresponds to the relaxation oscillation time, i.e., 2π in dimensionless time units. Therefore the internal mode becomes unstable first as predicted from the stability analysis.

It is interesting to notice that in-phase periodic oscillations appear when a positive coupling is used instead of a negative coupling, as shown in Fig. 3.13. Here, we focus on the amplitudes of oscillations by varying the coupling constants with negative coupling and show that the onset condition as well as the scaling behavior
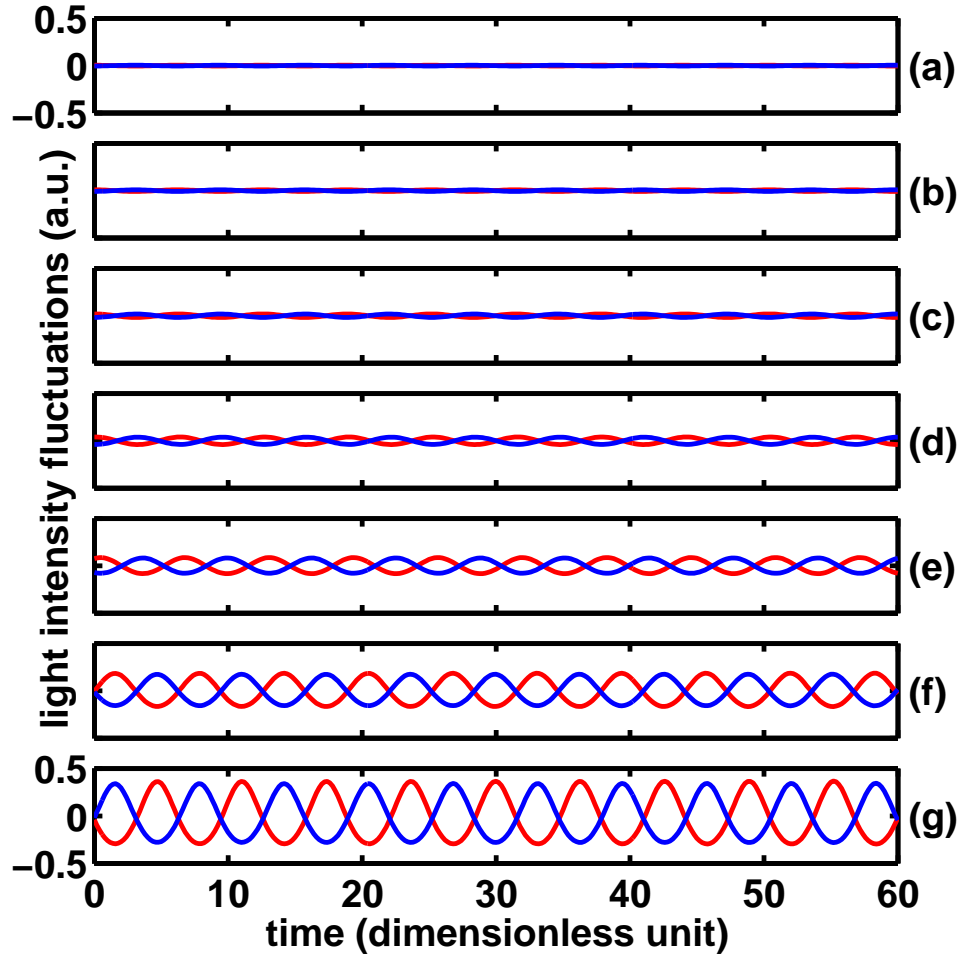
Figure 3.12: The emergence of the periodic oscillations in numerical simulation. Intensity time series are shown for $\delta_1 = 1.92$, and (a) $\delta_2 = 2.04$, (b) $\delta_2 = 2.06$, (c) $\delta_2 = 2.08$, (d) $\delta_2 = 2.10$, (e) $\delta_2 = 2.12$, (f) $\delta_2 = 2.14$, and (g) $\delta_2 = 2.16$. Red dots are $y_1(t)$ which is proportional to the light intensity fluctuations in LD_1, and blue dots are $y_2(t)$ which is proportional to the light intensity fluctuations in LD_2. ($a = 2$, $b = 1$, $\epsilon = \sqrt{0.001}$, and $\tau = 30$)
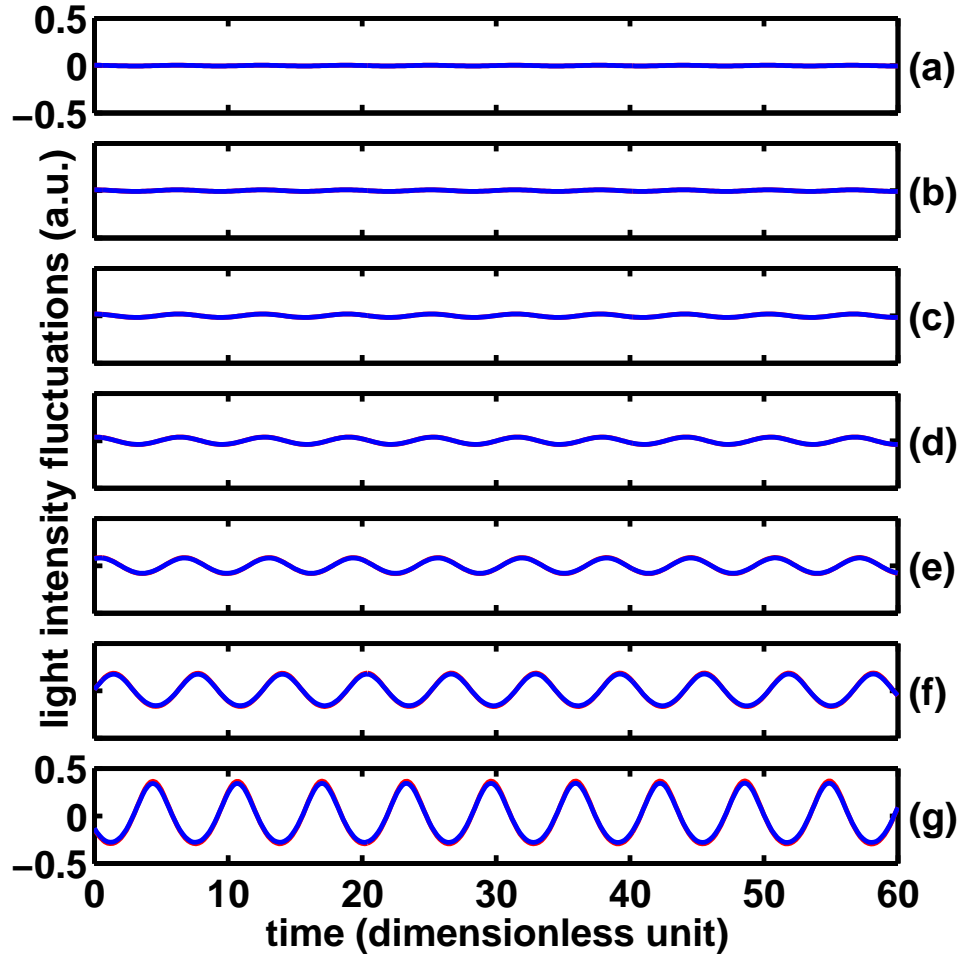
Figure 3.13: The emergence of the periodic oscillations in numerical simulation with a positive coupling scheme. Intensity time series are shown for $\delta_1 = -1.92$, and (a) $\delta_2 = -2.04$, (b) $\delta_2 = -2.06$, (c) $\delta_2 = -2.08$, (d) $\delta_2 = -2.10$, (e) $\delta_2 = -2.12$, (f) $\delta_2 = -2.14$, and (g) $\delta_2 = -2.16$. Red dots are $y_1(t)$ which is proportional to the light intensity fluctuations in LD_1, and blue dots are $y_2(t)$ which is proportional to the light intensity fluctuations in LD_2. ($a = 2$, $b = 1$, $\epsilon = \sqrt{0.001}$, and $\tau = 30$)
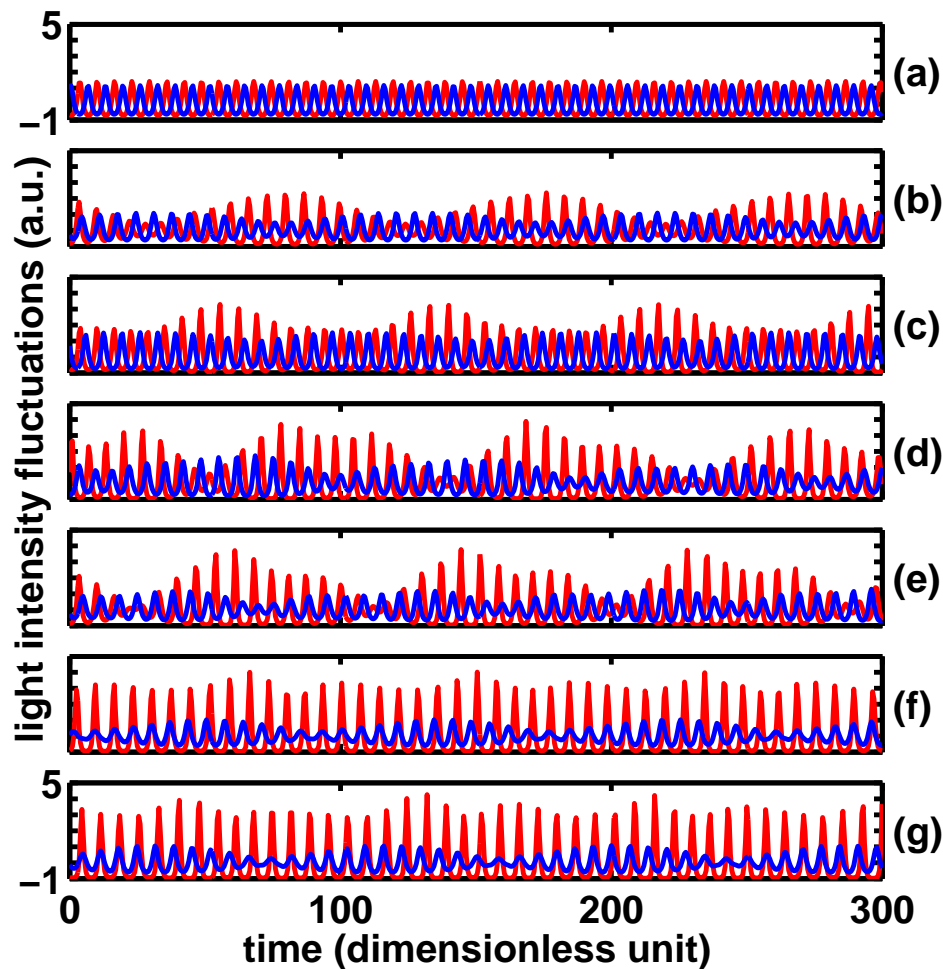
Figure 3.14: Complex patterns of oscillations in numerical simulation. Intensity time series are shown for $\delta_1 = 1.92$, and (a) $\delta_2 = 3.00$, (b) $\delta_2 = 5.00$, (c) $\delta_2 = 7.00$, (d) $\delta_2 = 9.00$, (e) $\delta_2 = 11.00$, (f) $\delta_2 = 13.00$, and (g) $\delta_2 = 15.00$. Red dots are $y_1(t)$ which is proportional to the light intensity fluctuations in LD_1, and blue dots are $y_2(t)$ which is proportional to the light intensity fluctuations in LD_2. ($a = 2$, $b = 1$, $\epsilon = \sqrt{0.001}$, and $\tau = 30$)

can be also found in numerical simulations. It is necessary for the phase relation between signals from both lasers to be investigated numerically, and some of the experimental observations will be presented in Chapter 4.

Fig. 3.14 shows the time series of the light intensity fluctuations at larger values of δ_2 with the same value of δ_1 used in Fig. 3.12. The time series are no longer periodic and show more complex patterns. The delay induced external modes begin to take part in the dynamics on top of the relaxation oscillations and the local maximum and minimum points do not remain constant as in the periodic regime. Both the envelope of the oscillations and the phase relation between the light intensity fluctuations from both lasers show complexity. For the remaining part of this chapter, we focus on the dynamical properties of the coupled lasers in the periodic regime.

Fig. 3.15 shows the amplitude of normalized intensity fluctuations, y_1 and y_2, versus the coupling constant δ_2 for different values of δ_1 obtained from the numerical computations. As in the experimental observations, the amplitude of the oscillations grows after the onset, and the value of δ_2 at the onset point decreases with increasing value of δ_1. The linear relationship between $log_{10}(\delta_2)$ and $log_{10}(\delta_2)$ at the emergence of oscillations is shown in Fig. 3.16. The best-fit linear model gives $log_{10}(\delta_1) + log_{10}(\delta_2) = 0.6$, therefore,

$$\delta_1 \delta_2 = 10^{0.6} = 4.0. \tag{3.42}$$

The onset condition for the internal mode is given by Eqn. 3.37, $\delta_1 \delta_2 = a^2$, and the result from numerical simulation matches to the mathematical analysis very well

60
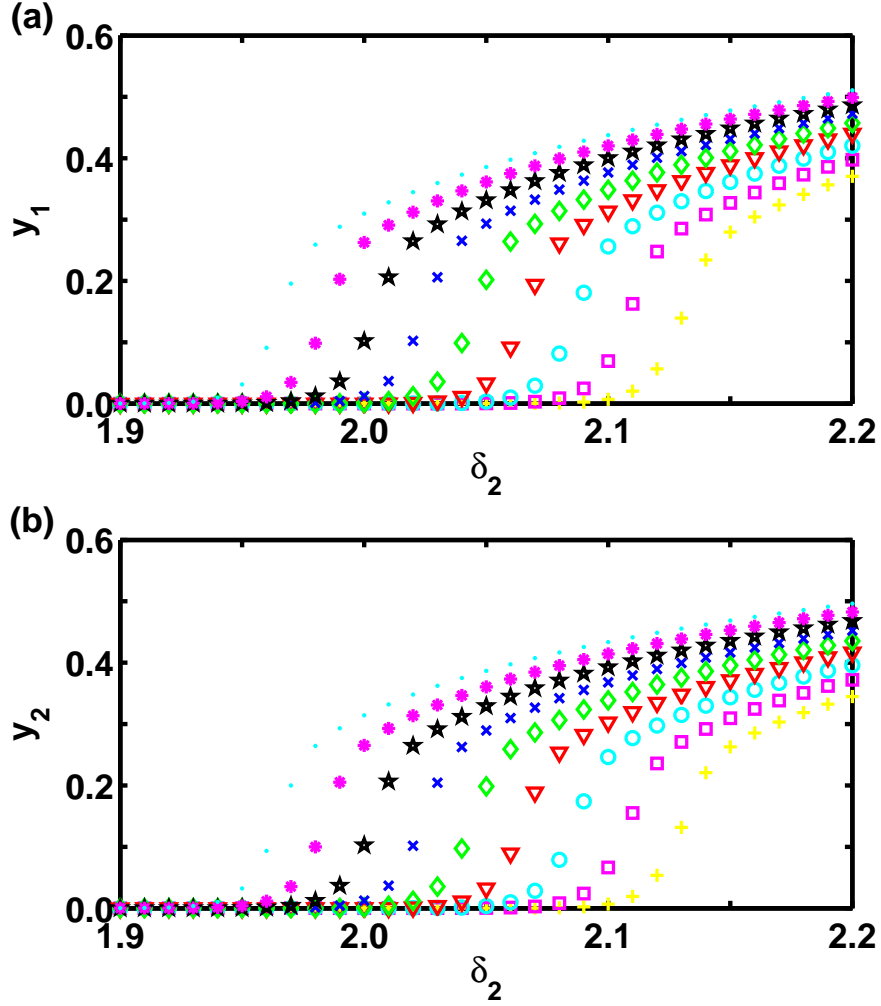
Figure 3.15: (a) The amplitude of the intensity fluctuations normalized to steady state level in the system 1, y_1, and system 2, y_2, versus the coupling constant δ_2 for different coupling constants δ_1. Plus signs show the amplitude for $\delta_1 = 1.90$; Squares for $\delta_1 = 1.92$; Circles for $\delta_1 = 1.94$; Triangles for $\delta_1 = 1.96$; Diamonds for $\delta_1 = 1.98$; Crosses for $\delta_1 = 2.00$; Stars for $\delta_1 = 2.02$; Asterisks for $\delta_1 = 2.04$; Points for $\delta_1 = 2.06$. These plots are obtained numerically with $a = 2$, $b = 1$, $\epsilon = \sqrt{0.001}$, and $\tau = 30$ in dimensionless units [63].
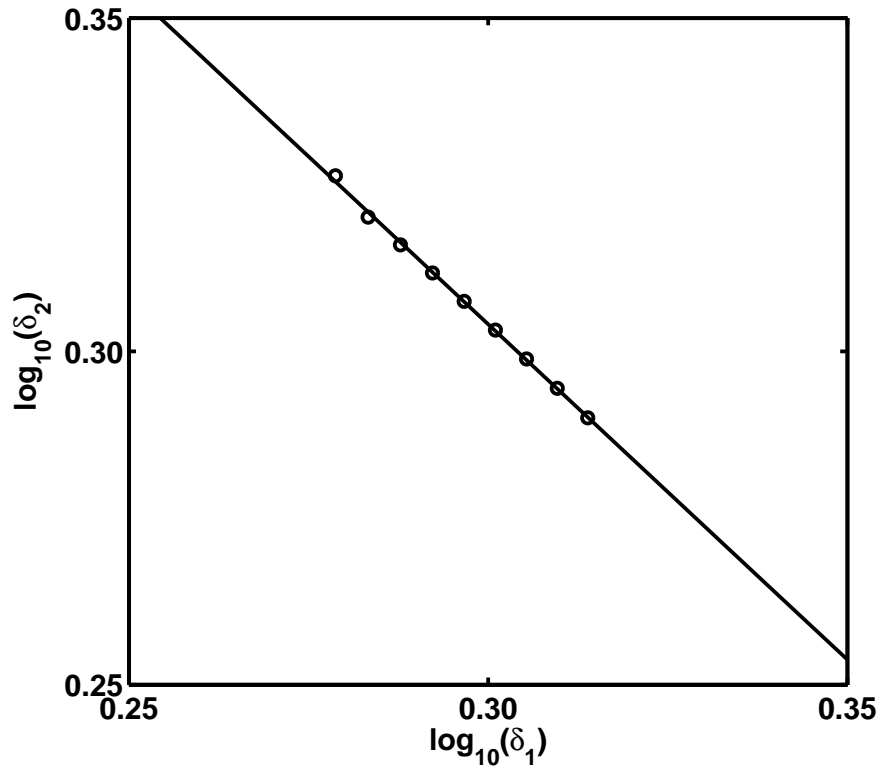
Figure 3.16: $log_{10}(\delta_2)$ versus $log_{10}(\delta_1)$ at the emergence of oscillations. The line shows the best-fit linear model. (Numerical simulations with $a = 2$, $b = 1$, $\epsilon = \sqrt{0.001}$, and $\tau = 30$.) [63]

with the given parameter, $a = 2$.

In Fig. 3.17(a) and 3.17(b), the rescaled amplitude of each system, $y_1/\sqrt{\delta_2}$ and $y_2/\sqrt{\delta_1}$, is plotted versus the product of the coupling constants, $\delta_1\delta_2$. The scaling property of the cross-coupled system can be seen very clearly in these figures, which display a data collapse similar to Fig. 3.9. The ratio of the rescaled amplitudes is plotted in Fig. 3.17(c), which is found to be unity. The experimental observations of cross-coupled lasers demonstrate more complex behavior as shown in Fig. 3.10, since differences between the lasers and detectors, as well as spontaneous emission noise levels, were not accounted for in the model.

Fig. 3.18 is similar to Fig. 3.17, except that the delay time is longer, i.e., $\tau = 150$. The scaling behavior still holds for the periodic regime. For larger values of $\delta_1\delta_2$, the intensity time series shows more complex patterns.

3.4.2 The Effect of a Low Pass Filter

So far, we have assumed an infinite-bandwidth response of the feedback loop in the numerical simulations. However, the electronic components, including photodetectors and amplifiers, have a finite bandwidth response in the real experimental system. The period of oscillations seems to be sensitive to the experimental components, such as the bandwidth limitations of electronic components and the possible resonance due to the boundary condition imposed by the connection between components. In this section, we investigate the effect of a low pass filter in order to understand how the system arrives at a stable state among the internal mode and an infinite number of external modes. The internal mode corresponding to the fast
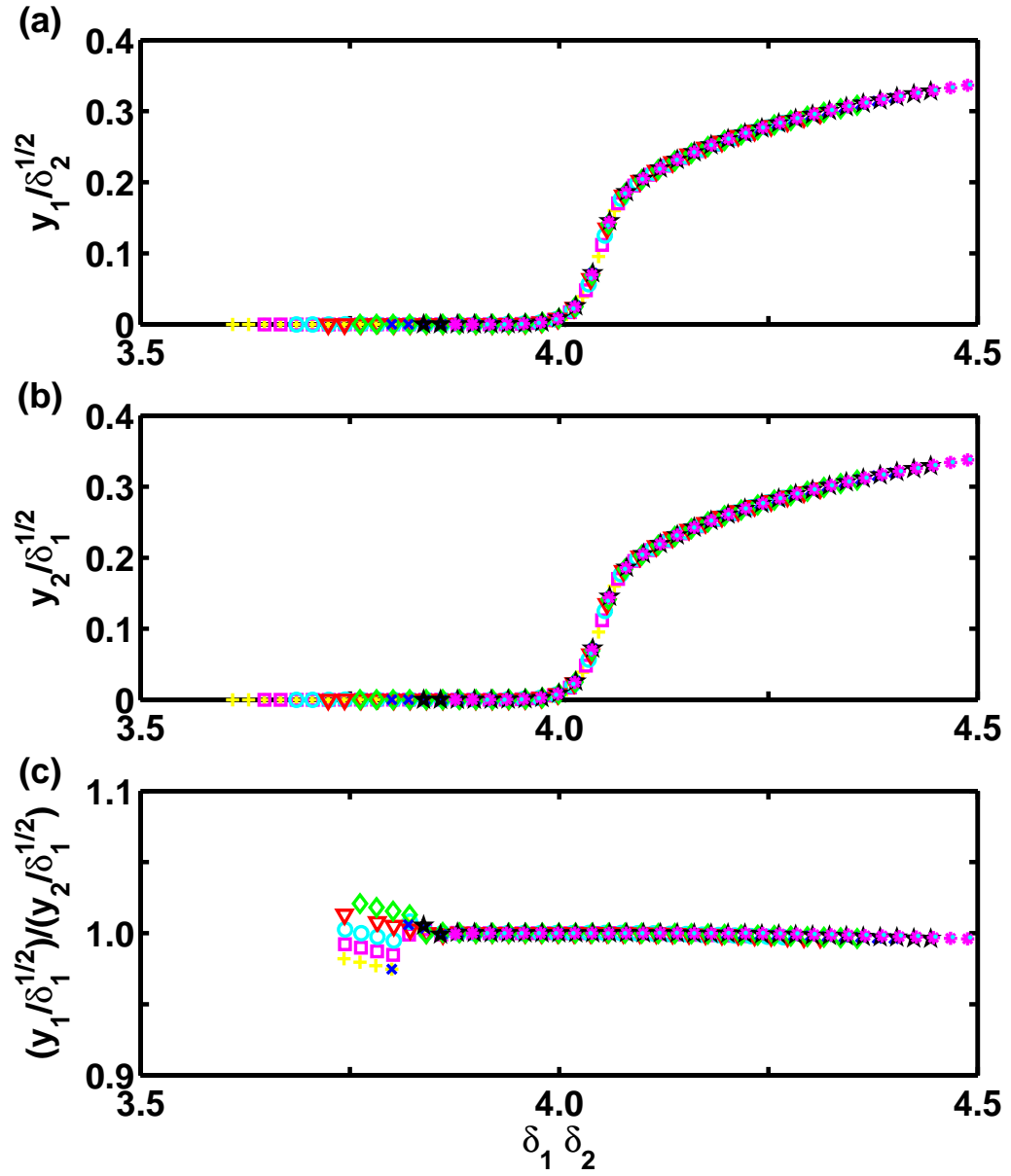
Figure 3.17: (a) The rescaled variable $y_1/\sqrt{\delta_2}$ versus the product of the coupling constants $\delta_1\delta_2$, and (b) $y_2/\sqrt{\delta_1}$ versus $\delta_1\delta_2$, showing the data collapse. (c) The ratio of the rescaled variables, $(y_1/\sqrt{\delta_2})/(y_2/\sqrt{\delta_1})$ versus $\delta_1\delta_2$. Same marker types are used for same δ_1 values in Fig. 3.15. (Numerical simulations with $a = 2$, $b = 1$, $\epsilon = \sqrt{0.001}$, and $\tau = 30$ in dimensionless units.) [63]
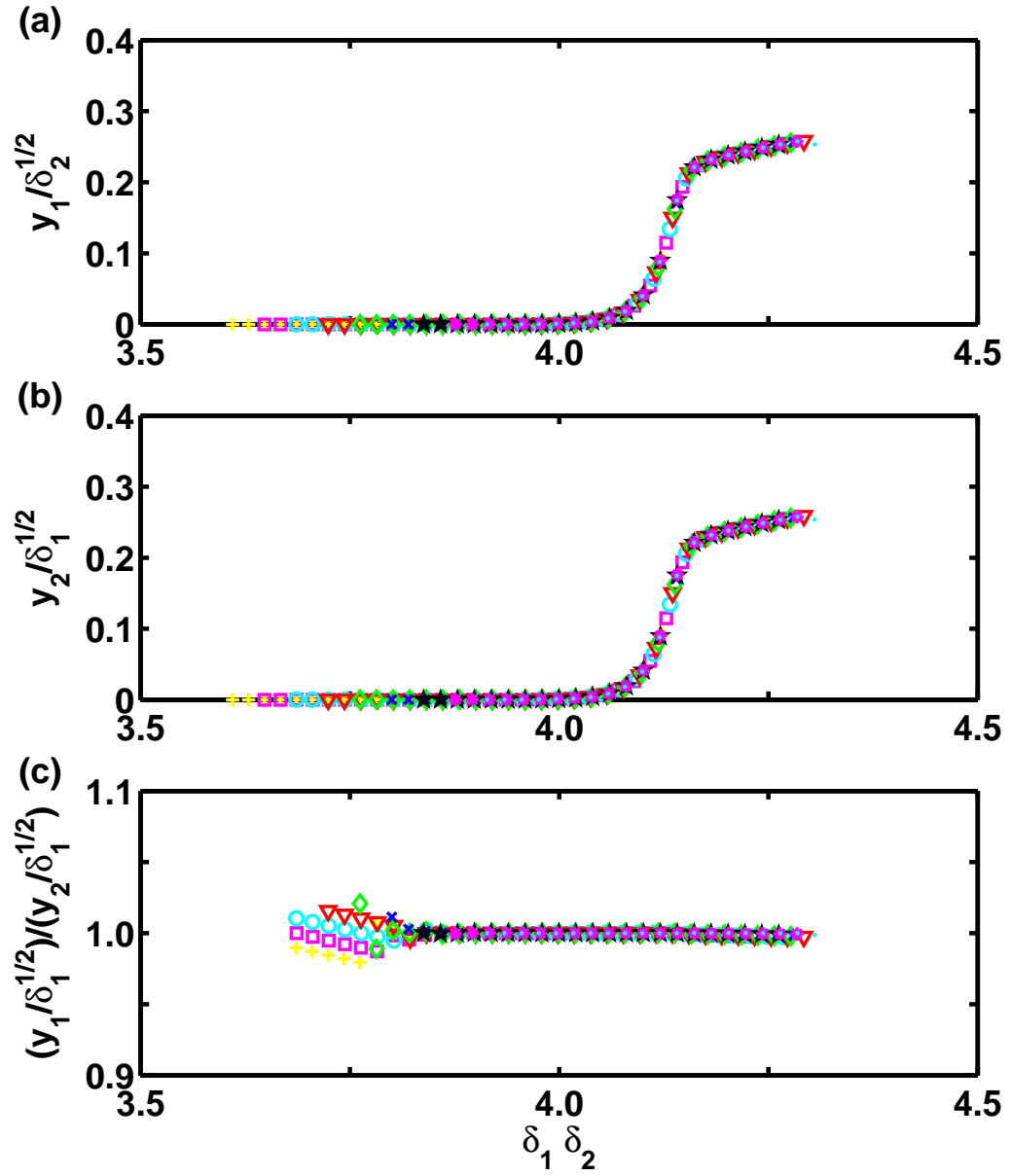
Figure 3.18: (a) The rescaled variable $y_1/\sqrt{\delta_2}$ versus the product of the coupling constants $\delta_1\delta_2$, and (b) $y_2/\sqrt{\delta_1}$ versus $\delta_1\delta_2$, showing the data collapse. (c) The ratio of the rescaled variables, $(y_1/\sqrt{\delta_2})/(y_2/\sqrt{\delta_1})$ versus $\delta_1\delta_2$. The same marker types are used for the same δ_1 values in Fig. 3.15. (Numerical simulations with $a = 2$, $b = 1$, $\epsilon = \sqrt{0.001}$, and $\tau = 150$ in dimensionless units.) [63]

relaxation oscillations is suppressed by the bandwidth limitation of a low pass filter and an external mode corresponding to the fundamental oscillations introduced by the delay loop emerges as a stable solution.

A single pole low pass filter is described by the equation

$$\dot{V} = \omega_L(V_{in}(t) - V), \tag{3.43}$$

where V_{in} is the input to the filter, $V(t)$ is the output, and ω_L is the cut-off angular frequency. To incorporate a low pass filter into the numerical model, we add simple filter equations to Eqns. 3.17 - 3.20 as $\dot{v}_i(t) = \omega_L(y_i(t - \tau) - v_i(t))$ where $i = 1, 2$, and use $v_k(t)$ instead of $y_k(t - \tau)$ for the modulation terms.

For $\tau = 150$, by placing the cut off angular frequency between the relaxation frequency, $\omega_r = 1$, and the fundamental frequency set by the delay time, $\omega_0 = 2\pi/(2 \times 150) \sim 0.021$, the delay dependent periodicity can be successfully introduced. For convenience, we vary the coupling constants symmetrically and use a symmetric constant initial condition in the numerical simulations. In Fig. 3.19, for $\omega_L = 0.1$, we observe that in-phase oscillations with a period of twice the delay time become a stable solution and that the onset occurs at $\delta_1\delta_2 \sim O(\epsilon^{-2})$.

In summary, the low pass filter seems to prevent the bifurcation of the internal mode and assist the bifurcation of the external mode by introducing a frequency dependent gain factor. In other words, when the cut off frequency of the low pass filter is placed between the internal mode frequency and the external mode frequency, the effective coupling strength becomes small for the internal mode and the external mode can bifurcate.
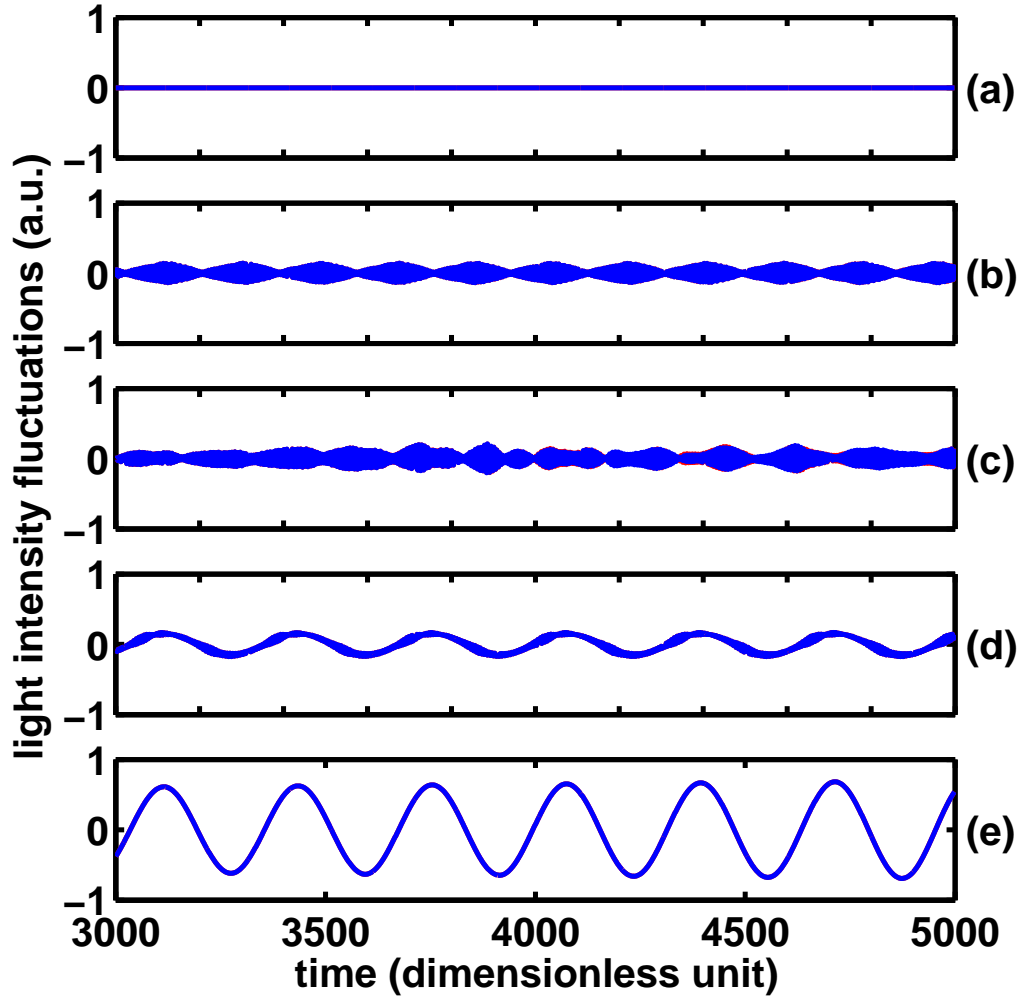
Figure 3.19: The intensity time series evolution of coupled identical lasers with a low pass filter in the feedback loop. Assuming $\delta_1 = \delta_2 \equiv \delta$, the time series is plotted for (a) $\delta = 2.5$, (b) $\delta = 30$, (c) $\delta = 1.0\ \epsilon^{-1}$, (d) $\delta = 1.02\ \epsilon^{-1}$, and (e) $\delta = 1.03\ \epsilon^{-1}$. Red dots are y_1 and blue dots are y_2. (Numerical simulations with $a = 2$, $b = 1$, $\epsilon = \sqrt{0.001}$, and $\tau = 150$ in dimensionless units.)

From the stability analysis, it has been shown that there exist an infinite number of external modes for the coupled identical lasers with delayed opto-electronic coupling. In this chapter, the fundamental external mode, for which the period of oscillations was twice the delay time, was observed as a stable solution. In Chapter 4, we present the dependence of periodicity on the delay time with experiments where the total delay time is changed by inserting an optical fiber in different lengths. Before we investigate this topic, we will discuss the implications of our observations in the following section.

3.5   Applications to Epidemics

The role of delays in the transmission of disease caused by migration between populations has received inadequate study. Two examples demonstrate the importance of this phenomenon in the geographic spread of disease outbreaks. A study of pre-vaccine measles epidemics in Iceland showed that the pattern of epidemics changed after World War II because of the greater internal and external transportation links (especially air travel), and as a result, epidemics became smaller and more frequent [61]. More recently, a study of the incidence of the mosquito-borne illness dengue hemorrhagic fever in 72 provinces of Thailand from 1983 to 1997 revealed a travelling wave emanating from Bangkok, the capital city, with a period of three years [62]. Changes in weather conditions, corresponding to the external drives, appear unlikely to explain this periodicity.

The longer period of outbreak recurrence compared with seasonal forcing can

be related to the slower time scale set by the transmission delays. For the case of dengue fever, Gubler *et al.* mention that dengue epidemics were infrequent with intervals of 10 to 40 years during the 18th and 19th centuries [64, 65]. In the late years of the 20th century, however, the outbreaks occurred more frequently with 3 to 5 year periodicity, possibly due to urbanization and fast transportation, which can be related to a reduction of the effective delay time in the transmission of disease. Our results underline the importance of studying mechanisms of disease transmission between different populations.

Chapter 4

Determination of the Periodicity in the Dynamics of Cross-coupled

Lasers

In previous chapter, we showed that two cross-coupled lasers oscillate in-phase with

a period of twice the time delay, i.e., the loop delay time, when the coupling is strong

enough. Frequency locking has been studied in many nonlinear systems subjected to

external periodic forcing, such as a nonlinear pendulum driven by a periodic force, a

light sensitive Belousov-Zhabotinsky reaction under periodic optical forcing [66], and

laser systems with external modulation. However, few studies have been reported

in a semiconductor laser with delayed optoelectronic feedback [67, 68, 69], and even

less for cross-coupled semiconductor lasers with delayed optoelectronic coupling. In

this chapter, we study the periodicity and the phase relation of the cross-coupled

lasers with delayed negative optoelectronic coupling as we adjust the length of the

delay loop [70]. The effect of an external modulation will be also studied later in

this chapter.
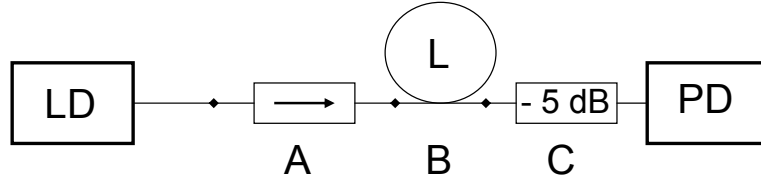
Figure 4.1: The optical path with an additional fiber. LD: a laser diode; A: a fiber optic isolator; B: a fiber of a length L; C: a 5 dB inline attenuator; PD: a photodetector.

4.1 Dependence of the Periodicity on the Delay Time in Cross-coupled Lasers

4.1.1 Period of Oscillations

As shown in Fig. 4.1, an additional fiber component at different length, L, is inserted between the optical isolator and the photodiode detector on the optical path. For simplicity, we increased the delay loop symmetrically by adding a fiber with the same length in each direction. Since the attenuation level along the single mode fiber is $\sim 0.25 dB/$ km at 1550 nm, we assume that the variation of the fiber length L, up to 200 m, doesn't change the coupling strength and that the default gains defined in Eqn. 3.2 and 3.3 remain constant with or without an additional fiber. The coupling strength d_1 is fixed for the experiments presented in this chapter and the coupling strength d_2 is varied as the length of an additional fiber is adjusted. Each time series is recorded for time windows of 0.2 ms at 2.5 GS/s.

Fig. 4.2 illustrates the in-phase and the anti-phase oscillations for the cross-coupled lasers with delayed negative opto-electronic coupling. Since the increase

71
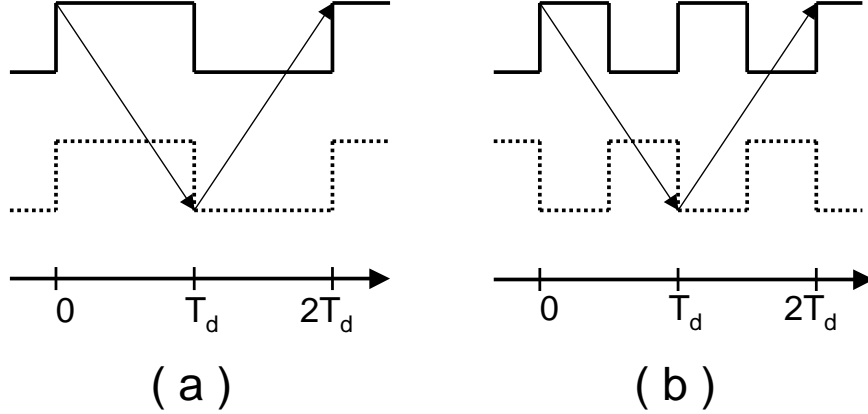
Figure 4.2: The illustration of (a) in-phase and (b) anti-phase relation for the cross-coupled lasers with negative opto-electronic coupling. The solid lines represent the state of LD_1 and the dashed lines represent that of LD_2. The arrows indicate the negative coupling after the propagation time delay T_d.

in the light power of one laser reduces the light power of the other laser after the propagation time delay T_d, either in-phase or anti-phase oscillations are possible as a periodic solution. The system demonstrates the in-phase relation when an odd number of oscillations exist during the loop delay time, i.e., $T_{\text{loop}} = 2T_d$, and exhibits the anti-phase relation for an even number of oscillations during the loop delay time.

In Fig. 4.3 through Fig. 4.10, we show the experimental intensity time series taken for $L = 2, 4, 8, 10, 20, 40, 100,$ and 200 m, as the coupling strength is made stronger. While in-phase oscillations emerge for the 2 m and 4 m case, anti-phase oscillations appear for longer fiber lengths, as the coupling is made stronger. In case of 200 m, switching between in-phase and anti-phase oscillations is observed.

Fig. 4.11 shows the observed frequency of the oscillations as well as the expected fundamental loop frequency. The oscillation frequency observed in the ex-
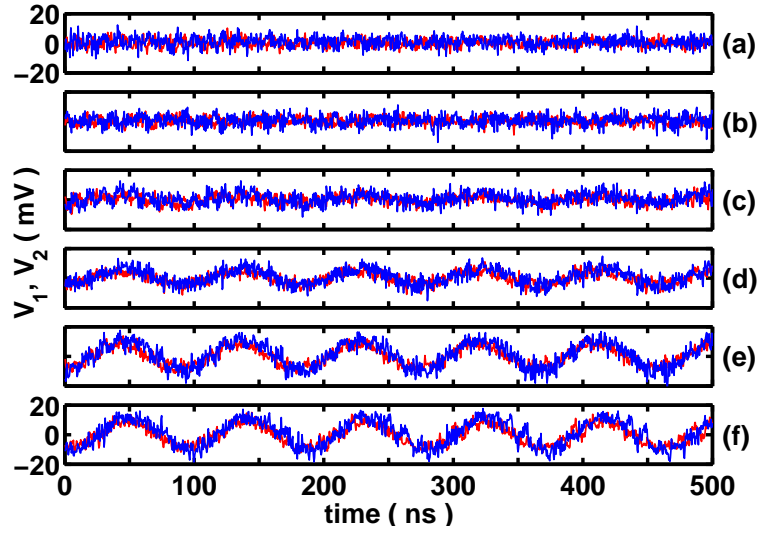
Figure 4.3: The time series taken for $L = 2m$. The product of coupling strengths, d_1d_2, is (a) 1.32, (b) 1.34, (c) 1.35, (d) 1.37, (e) 1.39, and (f) 1.40.
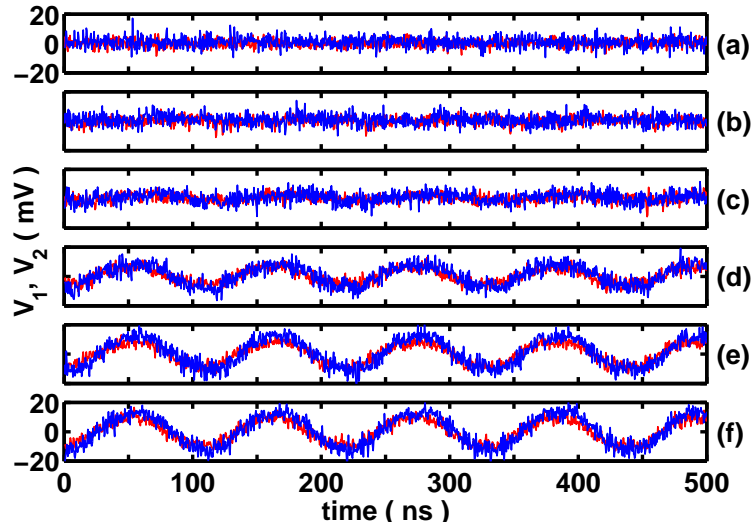
Figure 4.4: The time series taken for $L = 4m$. The product of coupling strengths, d_1d_2, is (a) 1.15, (b) 1.17, (c) 1.18, (d) 1.19, (e) 1.21, and (f) 1.22.
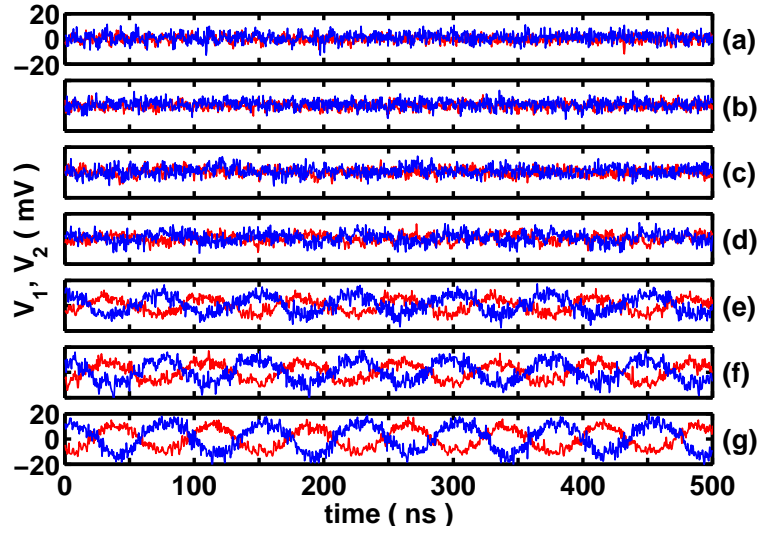
Figure 4.5: The time series taken for $L = 8m$. The product of coupling strengths, d_1d_2, is (a) 1.19, (b) 1.21, (c) 1.22, (d) 1.24, (e) 1.25, (f) 1.26, and (g) 1.28.
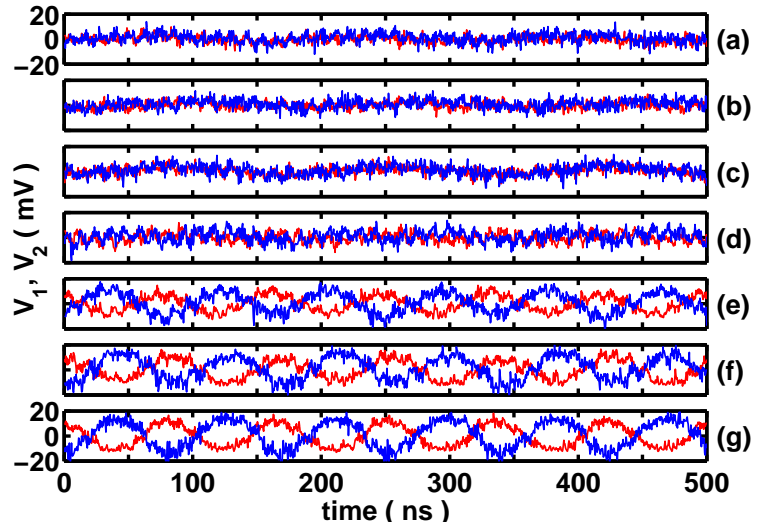
Figure 4.6: The time series taken for $L = 10m$. The product of coupling strengths, d_1d_2, is (a) 1.29, (b) 1.31, (c) 1.32, (d) 1.34, (e) 1.35, (f) 1.37, and (g) 1.39.

74
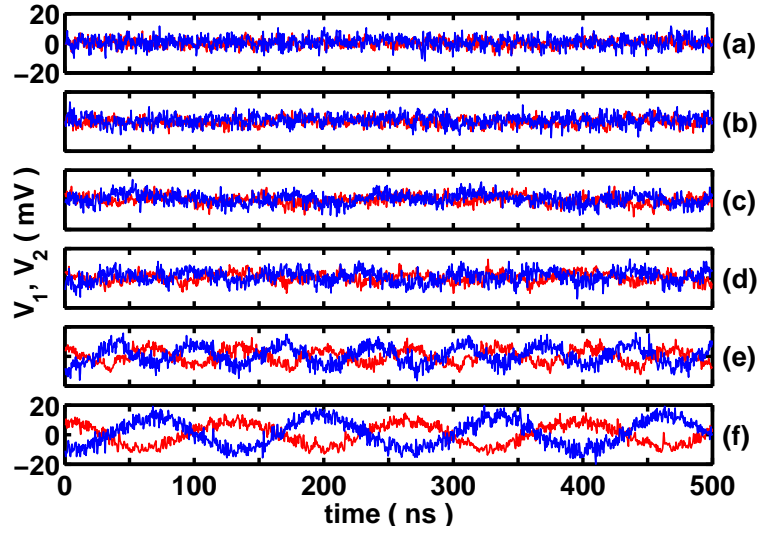
Figure 4.7: The time series taken for $L = 20m$. The product of coupling strengths, $d_1 d_2$, is (a) 1.24, (b) 1.25, (c) 1.26, (d) 1.28, (e) 1.29, and (f) 1.31.
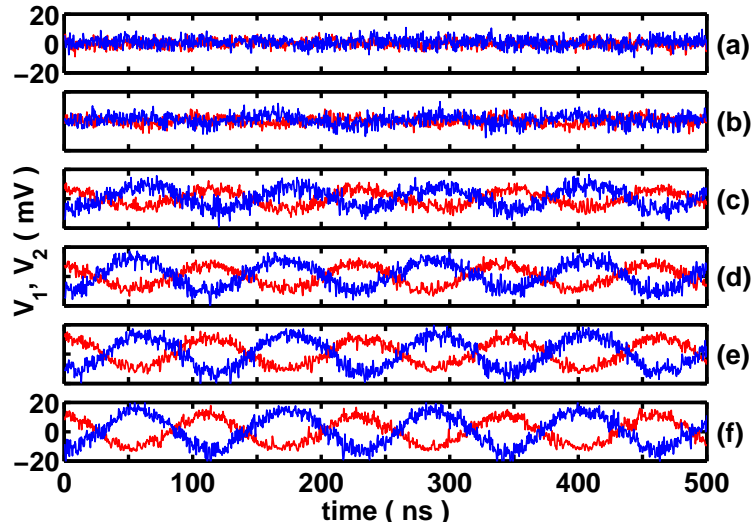
Figure 4.8: The time series taken for $L = 40m$. The product of coupling strengths, $d_1 d_2$, is (a) 1.25, (b) 1.26, (c) 1.28, (d) 1.29, (e) 1.31, and (f) 1.32.
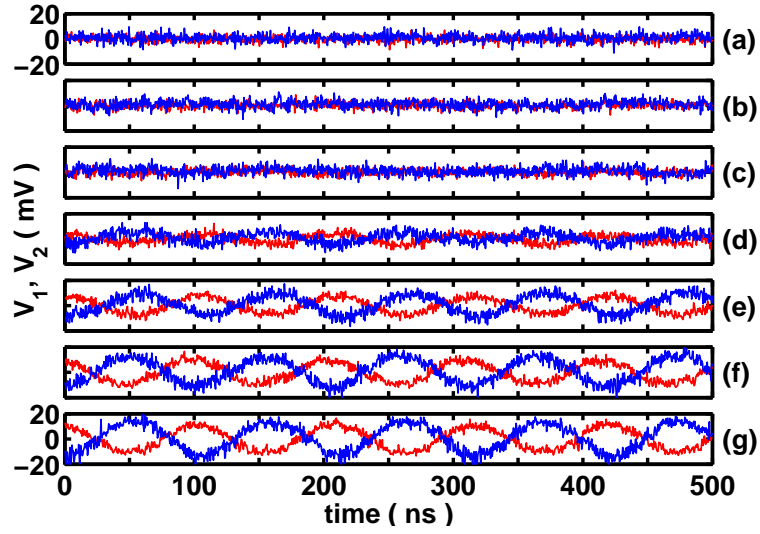
Figure 4.9: The time series taken for $L = 100m$. The product of coupling strengths, $d_1 d_2$, is (a) 1.28, (b) 1.29, (c) 1.31, (d) 1.32, (e) 1.34, (f) 1.35, and (g) 1.37.
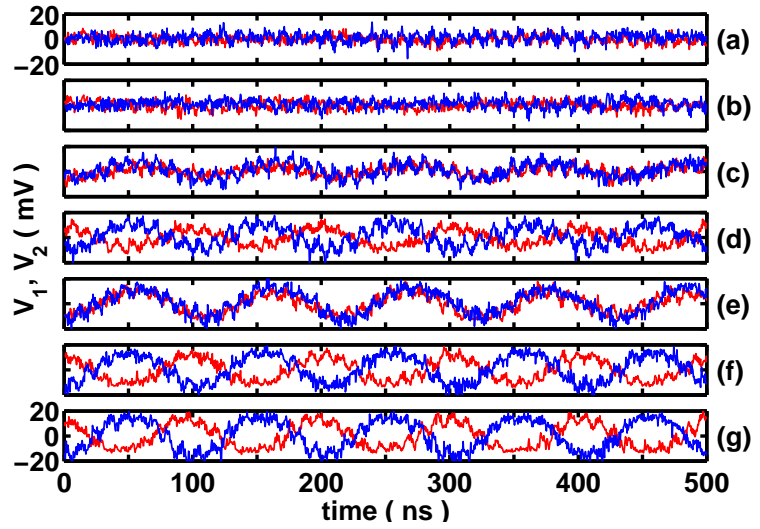
Figure 4.10: The time series taken for $L = 200m$. The product of coupling strengths, $d_1 d_2$, is (a) 1.26, (b) 1.28, (c) 1.29, (d) 1.31, (e) 1.32, (f) 1.34, and (g) 1.35.
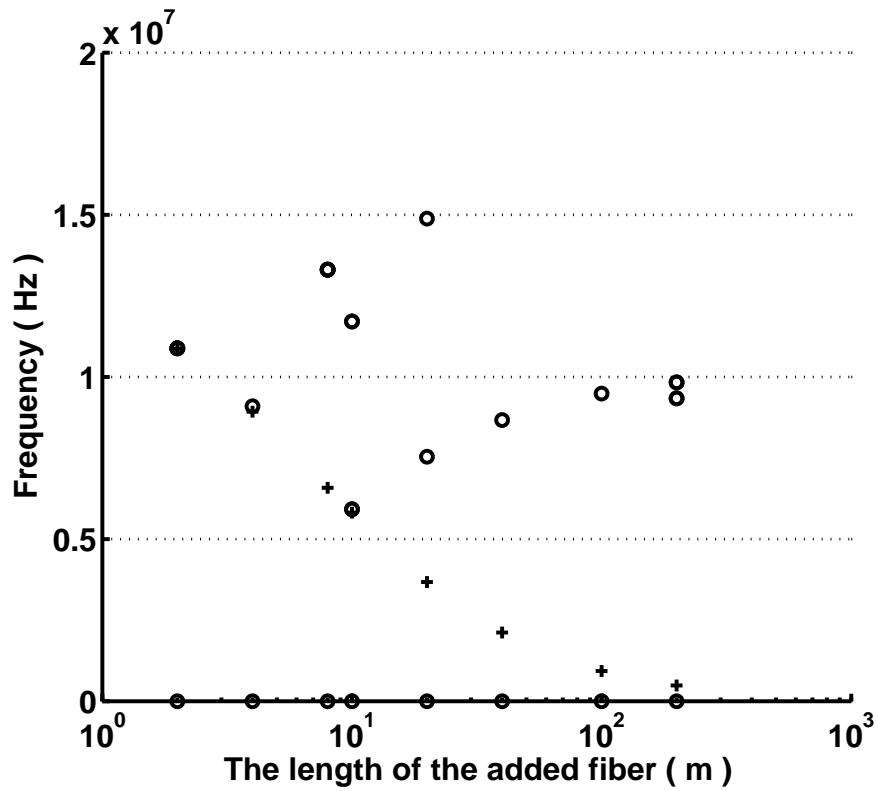
Figure 4.11: The frequency of oscillations versus the length of the additional fiber. Circles are the observed frequency from experimental measurements and pluses are the expected fundamental loop frequency [70].
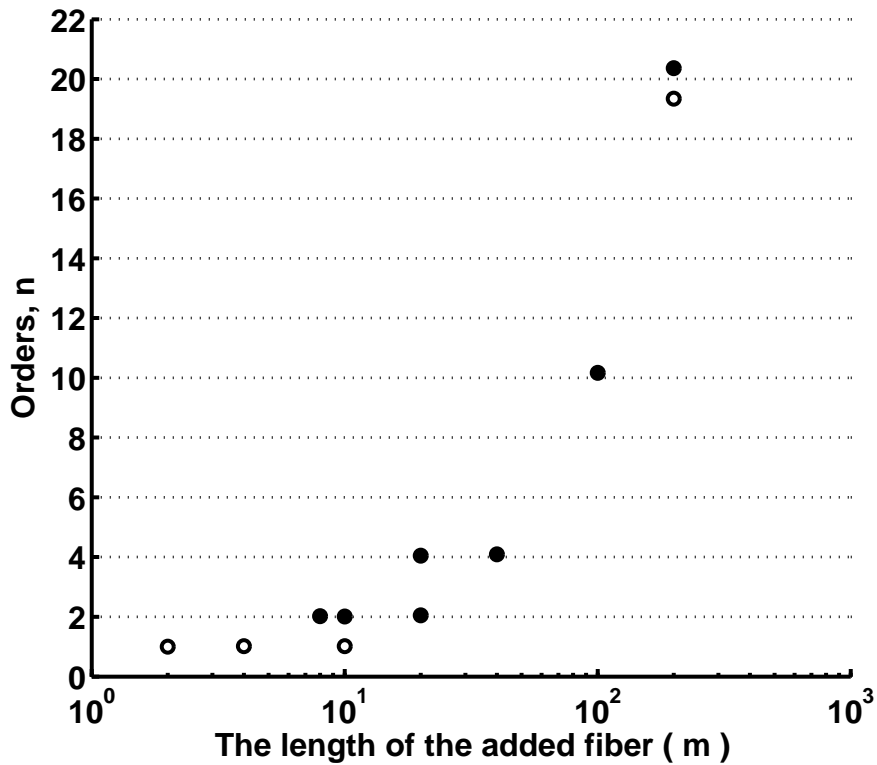
Figure 4.12: The orders of oscillations, $n = f/f_{\text{loop}}$, versus the length of the additional fiber. Open circles are for the in-phase oscillations and closed circles are for the anti-phase oscillations [70].

periment stays between 5 and 15 MHz, while the the expected fundamental loop frequency decreases monotonically as the delay time increases. Oscillations with the fundamental loop frequency, $f_{\text{loop}} = 1/T_{\text{loop}}$, are observed for $L = 2$ and 4 m, whereas oscillations with higher harmonics of the loop frequency are observed for the larger values of L.

A plot of the orders of harmonic oscillations is shown in Fig. 4.12. The orders of the harmonic oscillations, $n = f/f_{\text{loop}} = T_{\text{loop}}/T$ with the period T, increase from 1 to 20 as varying the length of the additional fiber from 2 m to 200 m. In addition to the orders, the phase relation between LD_1 and LD_2 is also shown in Fig. 4.12. The in-phase oscillations appear for an odd order while the anti-phase oscillations appear for an even order. This is consistent with the illustrations shown in Fig. 4.2.

4.1.2 Shifted Cross-correlation Coefficient

To compare two time series in more detail, we calculate the shifted cross-correlation coefficient

$$C(\Delta t) = \frac{< [V_1(t) - < V_1(t) >][V_2(t + \Delta t) - < V_2(t) >] >}{< |V_1(t) - < V_1(t) > |^2 >^{1/2} < |V_2(t) - < V_2(t) > |^2 >^{1/2}}, \qquad (4.1)$$

where $< \cdot >$ denotes the time average. In this calculation, the time series from PD_2 is continuously time shifted by a value of Δt with respect to the time series from PD_1.

Fig. 4.13 and Fig. 4.14 show the color map of the shifted cross-correlation coefficient calculated from the time series taken for different lengths of the additional fiber. The horizontal axis represents the time shift Δt and the vertical axis represents
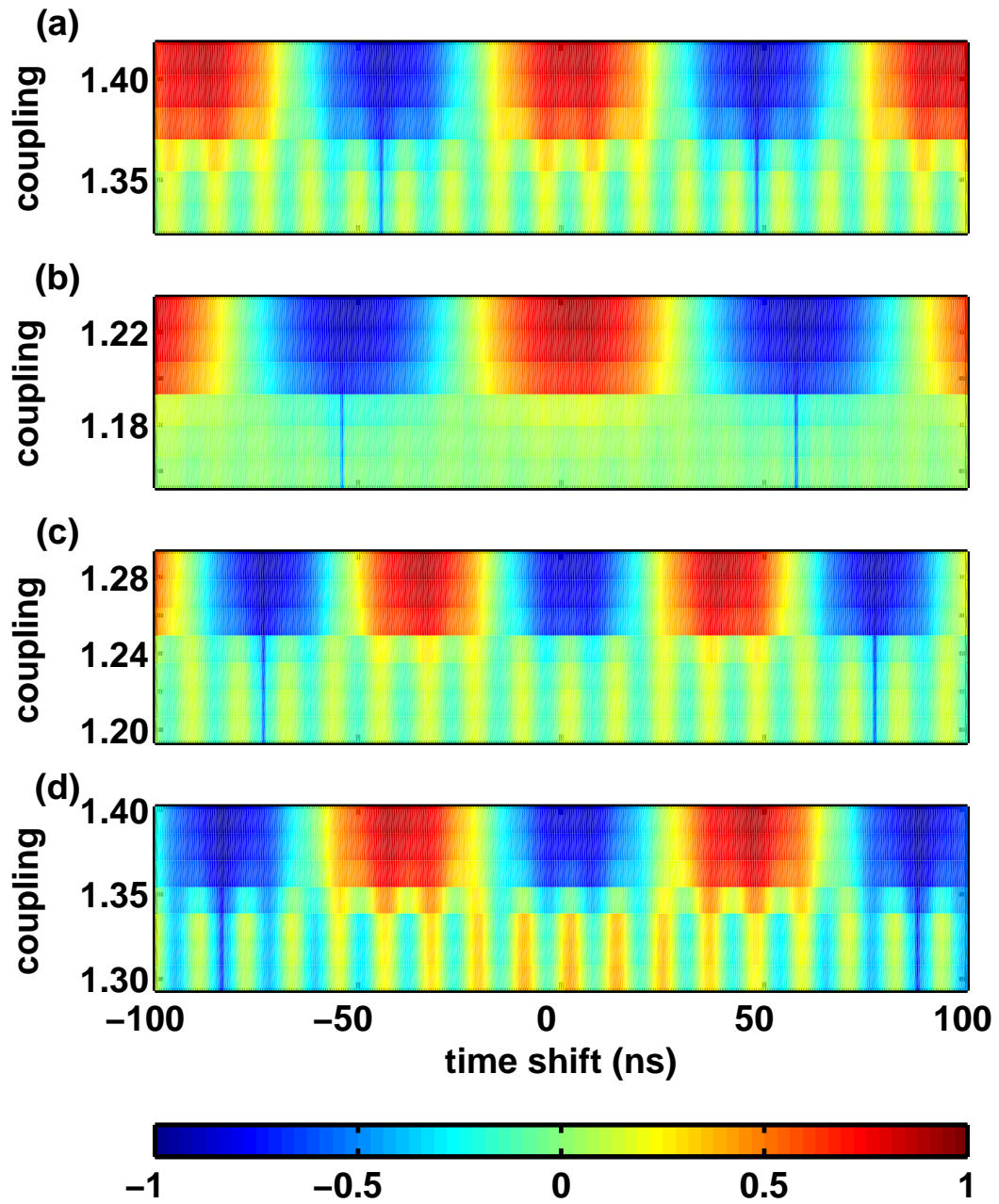
Figure 4.13: The color map of the shifted cross-correlation coefficient calculated from the time series taken for (a) $2\ m$, (b) $4\ m$, (c) $8\ m$, and (d) $10\ m$. The horizontal axis represents the time shift in nano seconds and the vertical axis represents the product of coupling strengths, $d_1 d_2$ [70].
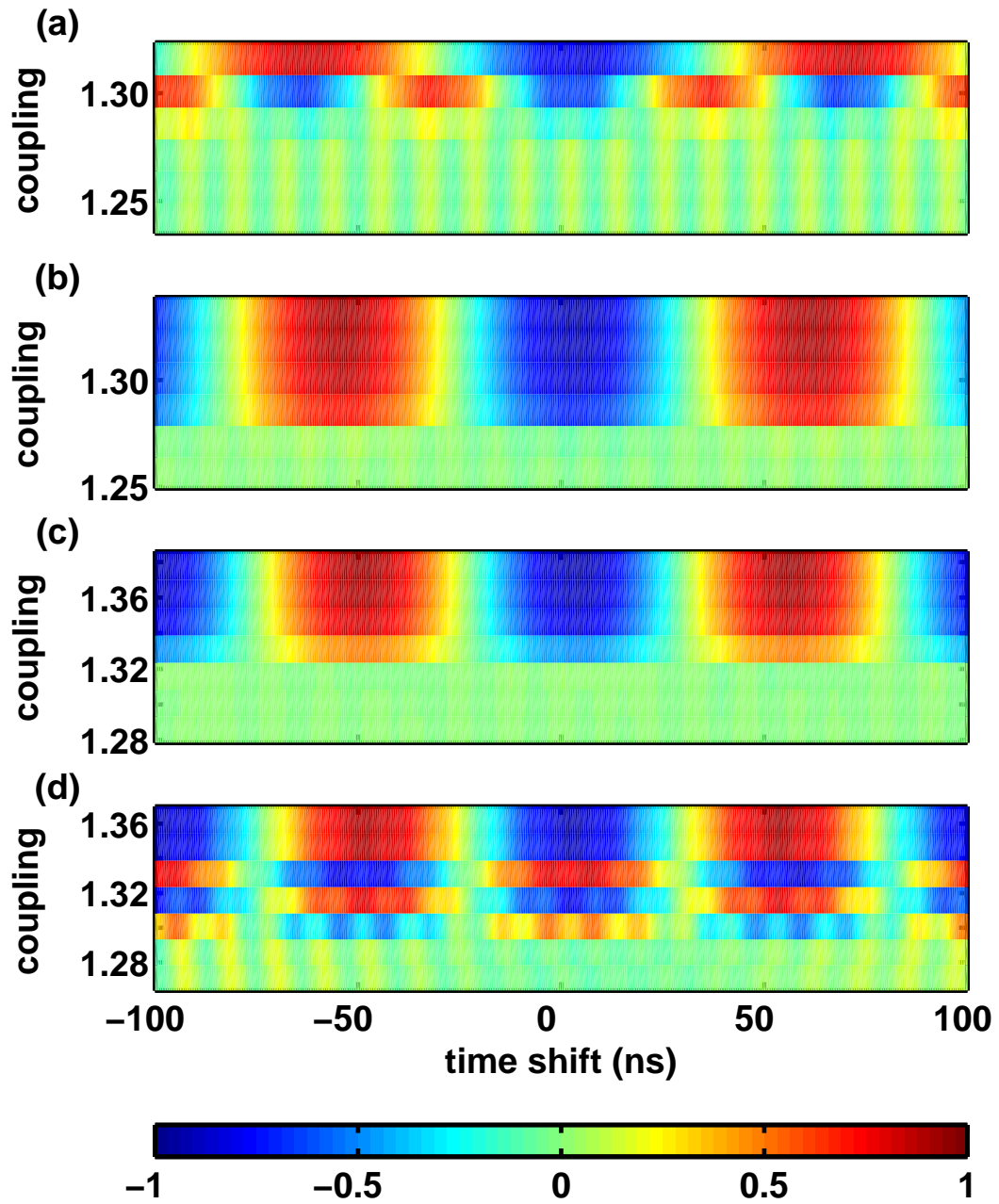
Figure 4.14: The color map of the shifted cross-correlation coefficient calculated from the time series taken for (a) 20 m, (b) 40 m, (c) 100 m, and (d) 200 m. The horizontal axis represents the time shift in nano seconds and the vertical axis represents the product of coupling strengths, $d_1 d_2$ [70].

the product of the coupling strengths. The red color corresponds to $C = +1$ while the blue corresponds to $C = -1$. As the coupling is made stronger, i.e., moving upward in vertical direction, a periodic band structure of blue and red appears. The difference in the time shift between the nearest red bands or between the nearest blue bands corresponds to the dominant period of oscillations.

In Fig. 4.13, two blue lines are observed at $\Delta t \sim \pm T_d$ for all considered coupling strengths. This is due to the delayed negative coupling between two lasers. The difference in the time shift between these blue lines corresponds to the loop delay time. Between the two blue lines, there is one repetition of color pattern in Fig. 4.13(a) and (b), indicating that the order of oscillation frequency is 1. On the other hand, in Fig. 4.13(c), there are two repetitions of color pattern, meaning the order is now 2. In Fig. 4.13(d), the order changes from 1 to 2 as the coupling is made stronger.

It is also interesting to see the value of the shifted cross-correlation coefficient at zero lag, i.e., $\Delta t \sim 0$. In Fig. 4.13(a) and (b), the color at zero lag is red, meaning that oscillations are in-phase for the cross-coupled lasers, while in Fig. 4.13(c), the color at zero lag is blue, meaning that oscillations are anti-phase. Again, in Fig. 4.13(d), the color changes from red to blue, i.e., the oscillations change from in-phase to anti-phase as the coupling is increased.

In Fig. 4.14, we don't observe the two blue lines corresponding to the loop delay time since they are located outside the window. Therefore, we cannot count the order of oscillations based on the color map. However, the color at zero lag still tells us whether the oscillations are in-phase or anti-phase. That is, in Fig. 4.14(a),(b), and

(c), the oscillations are anti-phase with blue color at zero lag, and in Fig. 4.14(d), switching between in-phase and anti-phase oscillations occurs, where each phase relation corresponds to the different frequencies of oscillation.

4.1.3   Competition between Dynamics with Two Different Time Scales

From the calculation of the shifted cross-correlation coefficient, another time scale is found in the experiment, which doesn't correspond either to the period of relaxation oscillations or to the loop delay time. In Fig. 4.13(a), a pattern with $\sim 12 \ ns$ periodicity is observed when the coupling is small. This is much longer than the relaxation oscillation period, $\sim 1 \ ns$, and much shorter than the loop delay time, T_{loop}, which is $\sim 72 \ ns$ without an additional fiber. The origin of this $(12 \ ns)^{-1} = 83 \ MHz$ frequency is not related to the optical path and has no dependence on the level of the injection current.

Assuming that this $12 \ ns$ time scale is not artificial (related with the sampling and the recording at the digital oscilloscope) and that the mechanism corresponding to this time scale plays an active role in dynamics of the cross-coupled laser system, we define a frequency f_s which characterizes this $12 \ ns$ oscillations. This may be explained by some resonance due to the boundary conditions imposed by connections between electronic components or due to the response of the photodetector circuitry.

There are two methods with which a new time scale described by f_s can be introduced in the system. One is an external modulation of the injection current to the lasers and the other is an initial function with periodicity characterized by f_s. The possibilities of these two methods as candidates for a source of the new time

scale are under investigation with numerical simulations.

In Fig. 4.13, we find a relationship between f_s and the fundamental loop frequency f_{loop}. Notice that the two blue lines at $\Delta t \sim \pm T_d$ coincide with two minima of the modulation pattern. Defining the ratio of the frequency f_s to the loop frequency f_{loop} as r, we observe that the in-phase oscillations emerge when r is an even integer and that the anti-phase oscillations emerge when r is an odd integer. Therefore, the oscillation frequency and the phase relation of two cross-coupled lasers seem to be determined by the competition between dynamics with two different time scales, i.e., the dynamics characterized by f_s and f_{loop}. The relaxation oscillation is not taken into consideration due to the finite frequency bandwidth of the electronic path.

4.2 Effect of an External Modulation

In this section, we study how the external modulation interacts with the internal dynamics of two cross-coupled semiconductor lasers with delayed negative opto-electronic feedback. Fig. 4.15 illustrates the schematic diagram of cross-coupled lasers with an external modulation. A sinusoidal signal generated from a function generator (Stanford Research Systems, DS345) is combined with the delayed feedback signal from LD_2 at a location between a DC blocking capacitor and a variable attenuator ($Attn_2$) to modulate the injection current of LD_1. To avoid reflections at each intersection point on the electronic path, a power splitter or a power combiner (Mini-Circuits, ZFSC-2-4, $0.1 - 1000 \ MHz$) is used to split or to combine signals.

We improved the experimental setup by replacing the old handmade laser mounts with commercial laser mounts (Thorlabs, LM14S2). Using this new setup without a function generator and the corresponding power combiner, the dominant frequency of oscillations without an additional fiber on the optical path is $f = 5f_{loop}$ with an in-phase relation. The scaling behavior and the onset condition still hold for this 5th harmonic solution.

Since we are interested in the effect of an external modulation on the existing internal dynamics of the cross-coupled lasers, we fix the coupling strength in both directions such that the product of the coupling strengths are slightly above the onset point ($g_1 = g_2 = -6 \ dB$). The time series of the system, V_1, V_2 and V_3, are taken simultaneously for 0.1 ms at 2.5 giga samples per second (GS/s), where the photodiode output voltages, V_1 and V_2, are proportional to the light power
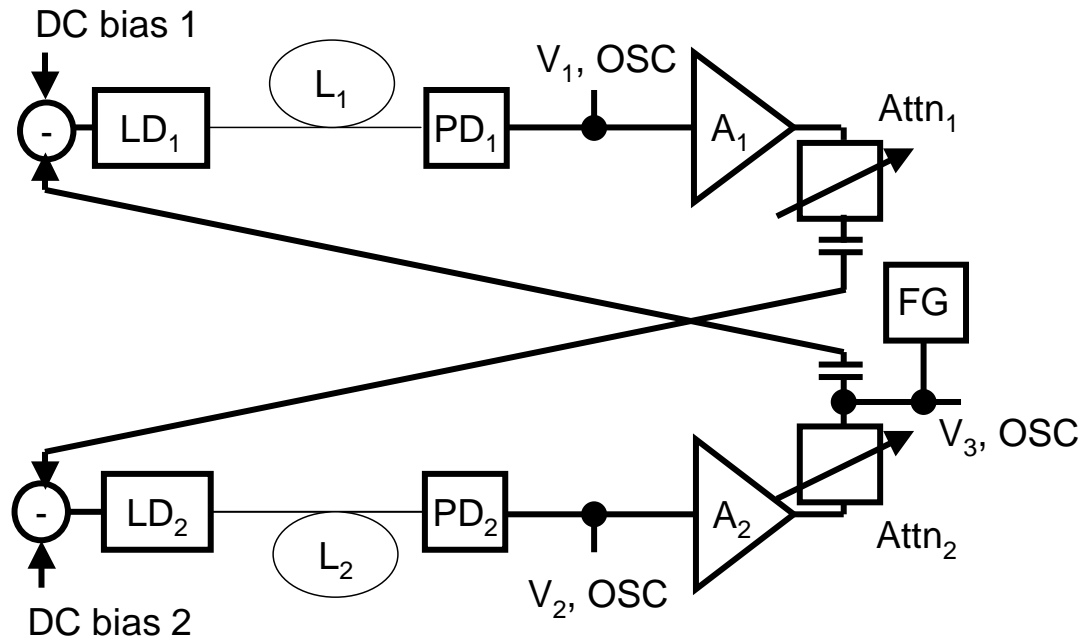
Figure 4.15: Schematic diagram of cross-coupled lasers with an external modulation. LD_1 and LD_2: laser diodes; PD_1 and PD_2: photodiodes; L_1 and L_2: optical fibers; OSC: oscilloscope; V_1 and V_2: photodiode output voltages; A_1 and A_2: electronic amplifiers; $Attn_1$ and $Attn_2$: variable electronic attenuators; FG: function generator; V_3: output voltage from FG. A sinusoidal signal generated from a function generator (FG) is combined with the feedback signal from LD_2 at a location between a DC blocking capacitor and a variable attenuator ($Attn_2$) to modulate LD_1.

fluctuations of each laser, and the output voltage from the function generator V_3 is used as a reference signal. We can control the peak-to-peak amplitude V_{mod} and the frequency f_{mod} of a sinusoidal wave.

Fig. 4.16 shows the power spectrum of each voltage signal with $V_{mod} = 0\ mV$. V_1 and V_2 oscillate in phase and the peak-to-peak amplitude is $30\ mV$. The dominant peak in the power spectrum is located at $f = 42\ MHz \sim 3f_{loop}$. V_3 is not zero even though we used a power splitter and a power combiner to isolate signals. Therefore, it seems that adding an extra component on the electronic path such as a function generater may influence the dynamics of cross-coupled lasers with delayed opto-electronic feedback. Each electronic component becomes a part of the electronic path and interacts with the opto-electronic loop.

We vary the frequency of a sinusoidal wave from $1\ MHz$ to $30\ MHz$ at different modulation amplitudes $V_{mod} = 20\ mV$, $30\ mV$, $40\ mV$, and $50\ mV$. The dominant frequency is measured at each modulation frequency by calculating the power spectrum of the recorded time signal. In Fig. 4.17, the dominant frequency of the light power fluctuations (open circles) and that of a modulation signal (dots) are plotted for $V_{mod} = 20\ mV$, $30\ mV$, $40\ mV$, and $50\ mV$.

The light power fluctuations fall into three categories: the oscillations occur at $f = 28\ MHz = 2\ f_{loop}$ with anti-phase relation between V_1 and V_2, at $f = 42\ MHz = 3\ f_{loop}$ with in-phase relation between V_1 and V_2, or at $f = f_{mod}$ with various responses depending on the modulation signal. It seems that the external modulation added to the input of one laser and the boundary effect set by the negative opto-electronic coupling compete to arrive at a stable solution.
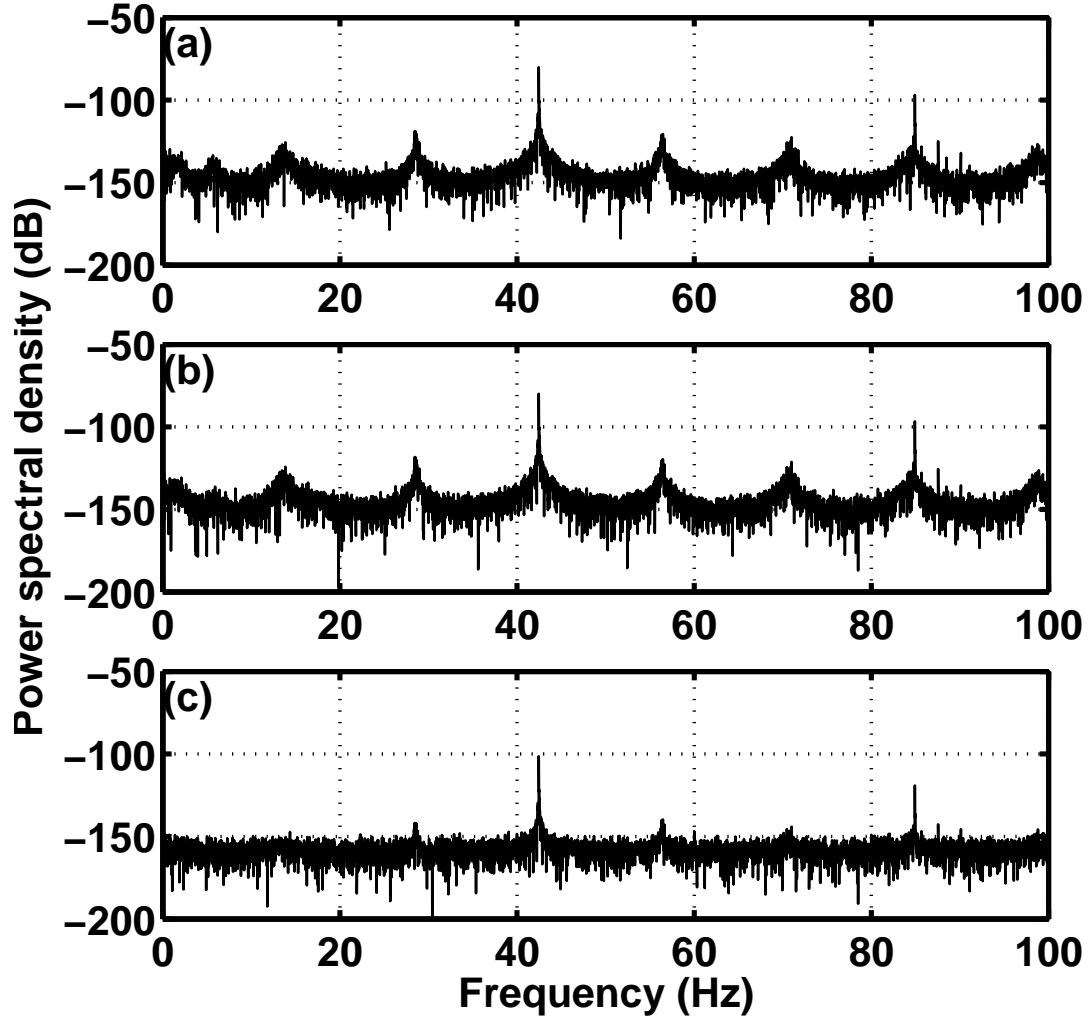
Figure 4.16: The power spectral density with 0 mV modulation amplitude. (a) Power spectral density calculated from V_1, (b) V_2, and (c) V_3. The dominant peak is located at 42.5 MHz. The loop frequency is $f_{\text{loop}} \sim 14\ MHz$ without an additional fiber on the optical path.
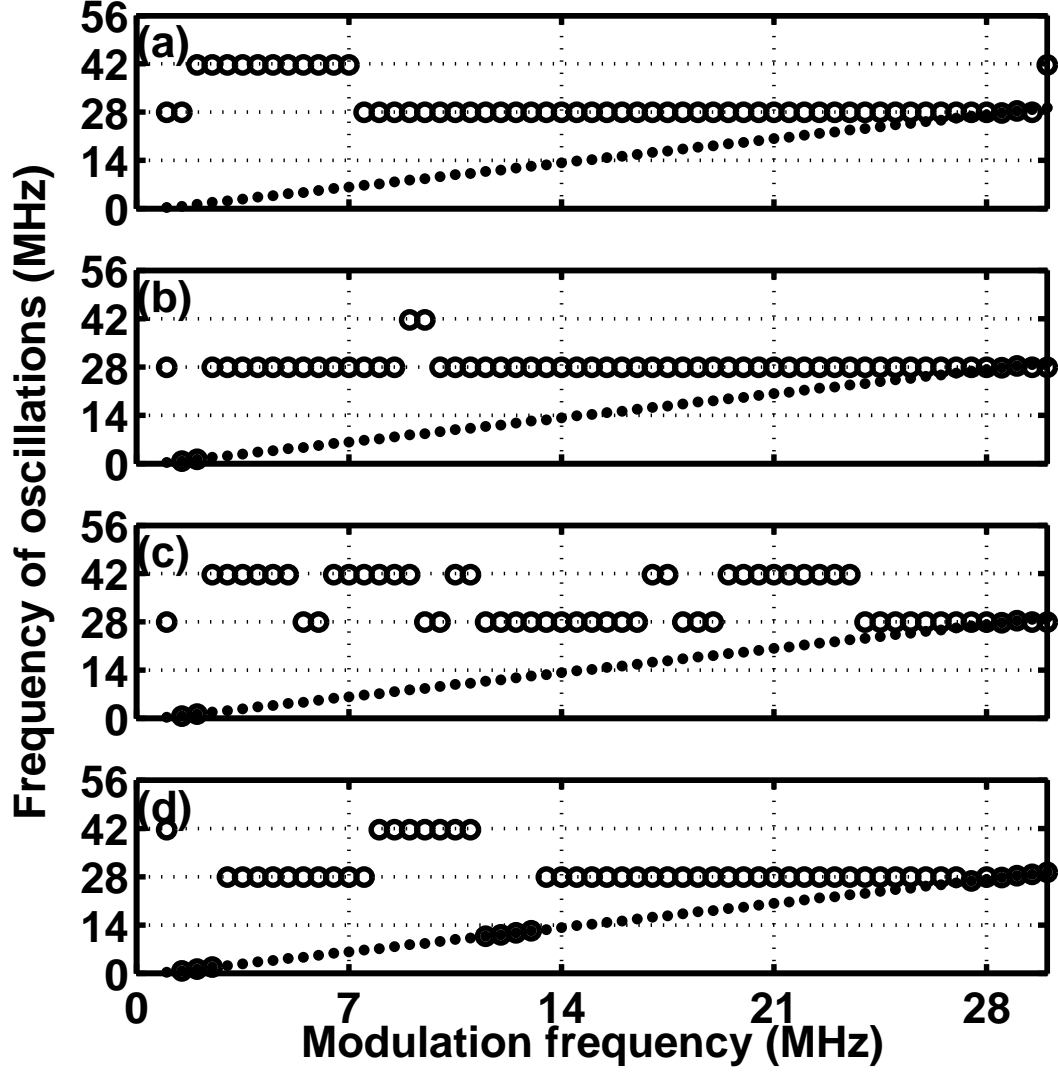
Figure 4.17: The frequency of oscillations as varying the modulation frequency f_{mod} from 1 MHz to 30 MHz at different magnitude of modulation amplitude, i.e., (a) $V_{\text{mod}} = 20\ mV$, (b) $V_{\text{mod}} = 30\ mV$, (c) $V_{\text{mod}} = 30\ mV$, and (d) $V_{\text{mod}} = 50\ mV$. The dots are the dominant frequencies measured from the sinusoidal input signals (V_3). The open circles are the dominant frequencies measured from the photodetector output signals (V_1, V_2).

The competition between dynamics with different time scale introduced by an external modulation in two cross-coupled lasers with negative opto-electronic coupling is currently under numerical investigation.

Chapter 5

Chaotic Dynamics of Electronic Circuit with Time-delayed Feedback

In this and the following chapter, we study the dynamics of an electronic circuit with time-delayed feedback and the synchronization of two uni-directionally coupled electronic circuits. The solitary circuit presented in this chapter is an oscillator that shows rich dynamics depending on the system parameter values. Following a brief introduction to the mathematical model, the analytical and numerical approaches to the model are presented, including the bifurcation and the route to chaos. The electronic realization of the model is presented in the following section.

5.1 Introduction to Mackey-Glass System

Since Mackey and Glass suggested a mathematical model to describe the dynamics in physiological control systems [4], there have been numerous studies on the, so called, Mackey-Glass system [29, 30, 31, 32, 33, 34, 35, 36, 37]. The Mackey-Glass model is described by a first order delay differential equation

$$\frac{dx}{dt} = \frac{ax_\tau}{1 + x_\tau^n} - bx, \tag{5.1}$$

where x is the variable of interest at time t, $x_\tau = x(t-\tau)$ is the delayed variable, and a, b, and n are constant parameters. For most of the numerical studies, the delay time is used as a control parameter with the fixed values of $a = 0.2$, $b = 0.1$ and $n = 10$. It is known that the system shows steady, periodic, and chaotic dynamics as the

delay time is varied [29]. The initial transition to chaos occurs at $\tau = \tau_c = 16.8$. The delayed feedback is a very convenient way of generating high dimensional systems. It is well known that the dimension of a system described by Eqn. 5.1 is proportional to the delay time [29].

With $a = 0.2$, $b = 0.1$ and $n = 10$, Eqn. 5.1 can be reduced by dividing the right hand side by b and scaling the time quantities $t \to bt$, $\tau \to b\tau$ ($\tau_c \to b\tau_c = 1.68$)

$$\frac{dx}{dt} = \frac{2x_\tau}{1 + x_\tau^n} - x \equiv F(x_\tau) - x, \tag{5.2}$$

where $F(x_\tau)$ corresponds to the delayed feedback [35]. Eqn. 5.2 has three stationary points $x^* = 0, \pm 1$. Depending on the initial conditions the attractor is located at either $x < 0$ or at $x > 0$. Since these two attractors are symmetrical, we consider the properties of the system close to the stationary point $x^* = 1$.

To study the evolution of small perturbations around the stationary point, we apply the linear stability analysis to Eqn. 5.2 and obtain

$$\frac{d\delta x}{dt} = \frac{\partial F(x_\tau)}{\partial x_\tau}\bigg|_{x_\tau = x^*} \delta x(t - \tau) - \delta x = -4\delta x(t - \tau) - \delta x, \tag{5.3}$$

where $\delta x = x - x^*$ defines the small deviations from the stationary point [35]. This equation can be solved by substituting $\delta x \propto e^{\lambda t}$,

$$\lambda + 4e^{-\lambda \tau} + 1 = 0, \tag{5.4}$$

where $\lambda = u + iv$ defines the eigenvalues of the stationary point. By separating the real and the imaginary part of above equation, we obtain

$$\text{Re} \quad : \quad u + 1 = -4e^{-u\tau} \cos(v\tau), \tag{5.5}$$

$$\text{Im} \quad : \quad v - 4e^{-u\tau} \sin(v\tau) = 0. \tag{5.6}$$

The Hopf bifurcation occurs when the eigenvalue becomes pure imaginary. By substituting $u = 0$,

$$v = 4\sin(v\tau), \tag{5.7}$$

$$1 = -4\cos(v\tau), \tag{5.8}$$

which can be rewritten as

$$v = -\tan(v\tau) \tag{5.9}$$

$$1 + v^2 = 16. \tag{5.10}$$

The value $\tau = (\arctan(-\sqrt{15}) + \pi)/\sqrt{15} = 0.471$ corresponds to the threshold of the Hopf bifurcation. For $\tau > 1.68$, the numerical simulations display chaotic attractors.

We used a fixed step fourth-order Runge-Kutta algorithm for numerical integrations of this system. The same constant initial function $x_0 = 0.9$ on $(-\tau, 0)$ was used. In order to investigate the dynamics of system described by Eqn. 5.2, we calculate the power spectrum of the time series. First, we generate a long time series starting with a constant initial condition. After removing the transient period, we divide the long time series into many sub-windows. The power spectrum for each sub-window is computed using the periodogram method (Fast Fourier Transform) and the individual results are averaged to produce an averaged power spectrum [32]. The phase portraits of the variable $x(t)$ versus the delayed variable $x(t - \tau)$ are also used to further characterize the solutions.

Fig. 5.1 shows numerical results of the time series, power spectra, and phase portrait at different delay times. When the delay time is short (Fig. 5.1(a)), the

system shows steady state behavior. As the delay time increases, the system begins to display periodic oscillations with a constant amplitude and phase (Fig. 5.1(b)). At long delay times, we observe period doubling bifurcations (Fig. 5.1(c) and Fig. 5.1(d)). For delay times longer than the critical value, i.e., $\tau_c = 1.68$, a chaotic attractor is observed as shown in Fig. 5.1(f). Fig. 5.2 is the bifurcation diagram of the local maxima of the time series as varying a delay time τ from 0.5 to 10.5. As the delay time is made longer, we observe that the system follows a period doubling route to chaos.

There is the possibility that different initial functions lead to different solutions for a given set of parameters, i.e., the dynamics are multistable [33, 71, 72]. However, we will only consider the solutions starting with a constant initial function for the numerical simulations presented in this dissertation.
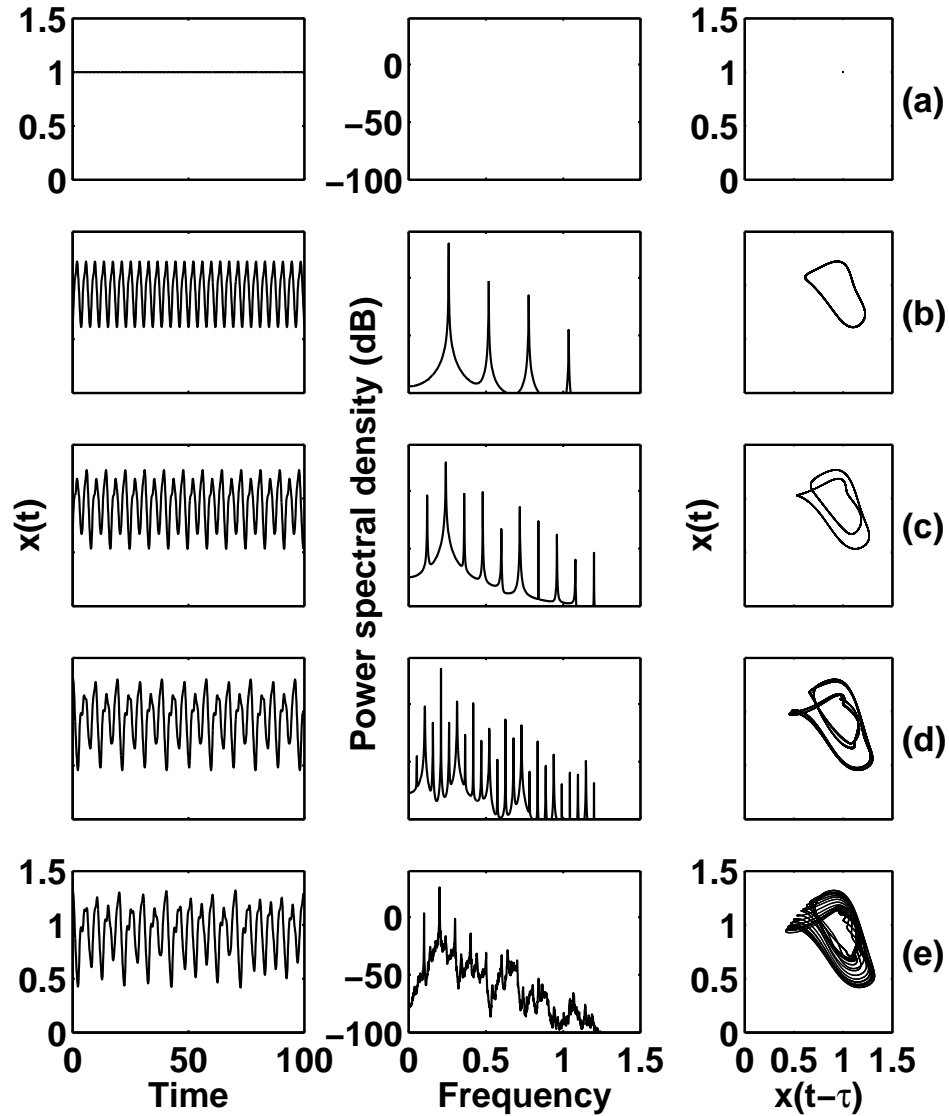
Figure 5.1: The time series (left), power spectra (middle), and phase portraits of $x(t)$ versus $x(t - \tau)$ (right) for different delay times. (a) shows a steady state at $\tau = 0.46$. (b) is a stable limit cycle at $\tau = 1.30$. (c) is a period-2 attractor at $\tau = 1.40$. (d) is a period-4 attractor at $\tau = 1.60$. (e) shows a chaotic attractor at $\tau = 1.70$. The spectra are obtained using the FFT algorithm and are averages of spectra from 20 consecutive 8192 sample points. The integration time step is $\Delta t_{\text{integration}} = 0.01$ and the sampling time is $\Delta t_{\text{sample}} = 0.1$. $x_0 = 0.9$ on $(-\tau, 0)$.
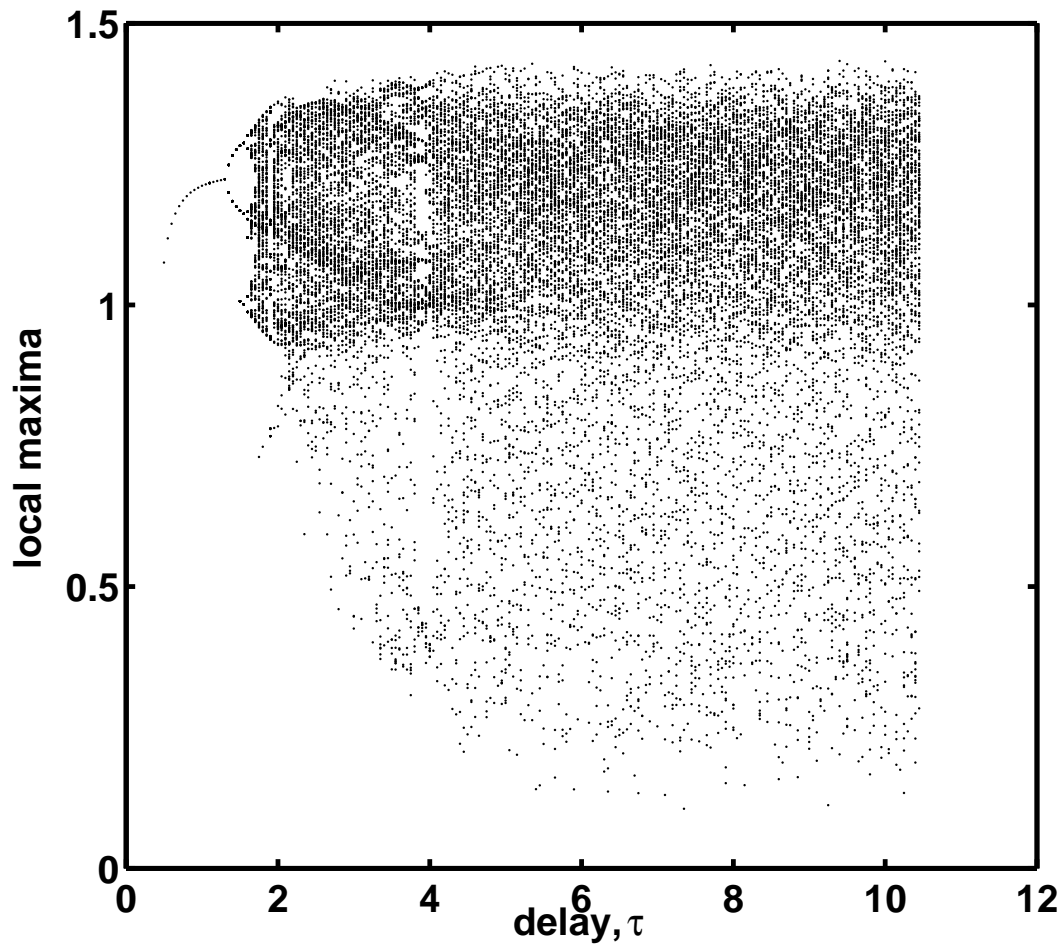
Figure 5.2: Bifurcation diagram of the local maxima of the time series with the delay time τ ranging from 0.5 to 10.5. The integration time step is $\Delta t_{\text{integration}} = 0.005$. $x_0 = 0.9$ on $(-\tau, 0)$.
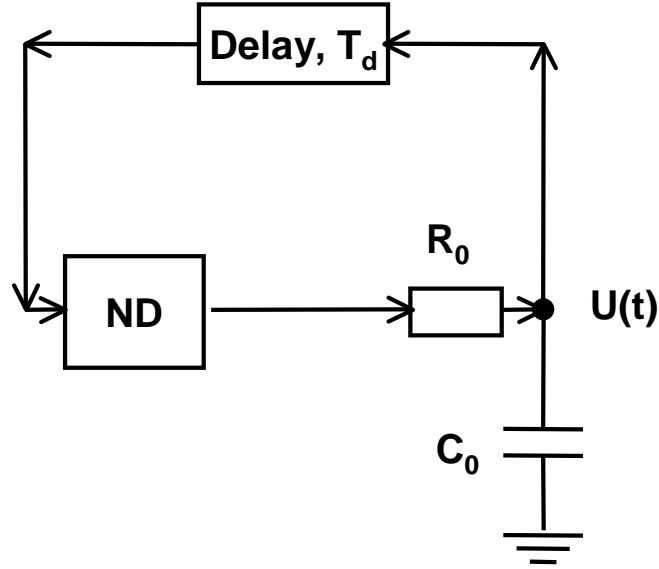
Figure 5.3: Block diagram of the Mackey-Glass analog circuit. ND is a nonlinear device, T_d is a time delay, and $U(t)$ is a voltage signal measured at a low pass filter. R_0 and C_0 are a resistor and a capacitor in the low pass filter section.

5.2   A Mackey-Glass Analog Circuit

An analog electronic circuit simulating a Mackey-Glass (MG) system [34, 73] was constructed. First demonstrated in Ref. [34], the circuit contains a delay unit, a nonlinear device (ND), and a fixed RC filter. Fig. 5.3 is the block diagram of the MG analog circuit and Fig. 5.4 is the picture of our MG circuit. In this section, we will describe the analog circuit in detail and study the dynamics as the linear gain of the ND is varied.

As shown in Fig. 5.5, the delay unit is a network of π-type LCL filters with matching resistors R at the input and the output. The output from the kth terminal is connected to the amplifier and the delay can be approximated by $T_d(k) =$
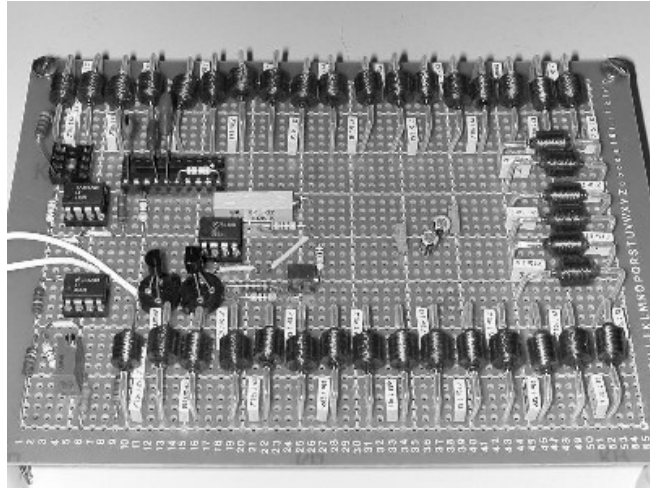
Figure 5.4: Picture of the Mackey-Glass analog circuit.
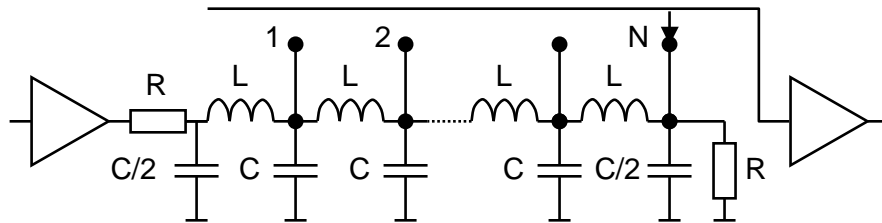
Figure 5.5: Block diagram of the delay unit. L's are inductors, C's are capacitors, and R's are matching resistors. $L = 4.7 \ mH$, $C = 10 \ nF$, $R = 680 \ \Omega$. $k = 1, \ 2, \ \ldots, N$ indicate the output terminals.
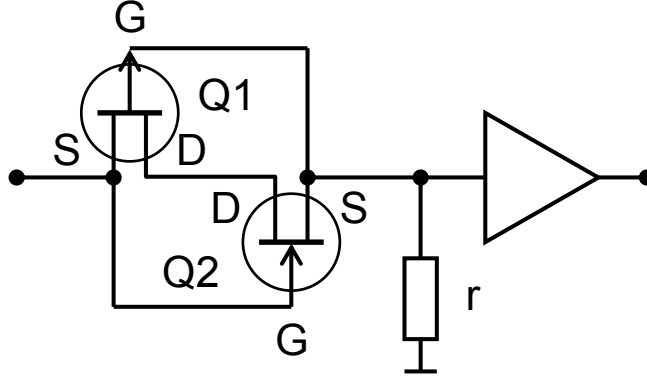
Figure 5.6: Block diagram of the nonlinear device. Q1 is a p-channel JFET(2N5461) and Q2 is a n-channel JFET(2N5458). G, S, D are the gain, source, and drain elements of the JFET, respectively.

$k(LC)^{1/2} \approx k(6.86 \ \mu s)$. The cutoff frequency of the delay line is $f_c = 1/(\pi\sqrt{LC}) \approx$ 46 kHz and the cutoff frequency of the RC low pass filter is $f_{RC} = (2\pi R_0 C_0)^{-1} \approx$ 6.2kHz. Therefore, $f_c \gg f_{RC}$, ensuring that the low pass filtered signals pass down the delay unit without much distortion.

The nonlinear device consists of two coupled junction field-effect transistors (JFETs) as shown in Fig. 5.6. The voltage signal from the resistor r is amplified in an operational amplifier and we use a potentiometer to control the linear gain of the nonlinear device. The resulting output characteristic is a unimodal function presented in Fig. 5.7. The input and output from the ND are normalized to the steady state.

The dynamics of the circuit shown in Fig. 5.3 are described by a delay-differential equation

$$R_0 C_0 \frac{dU(t)}{dt} = ND(U(t - T_d)) - U(t), \qquad (5.11)$$
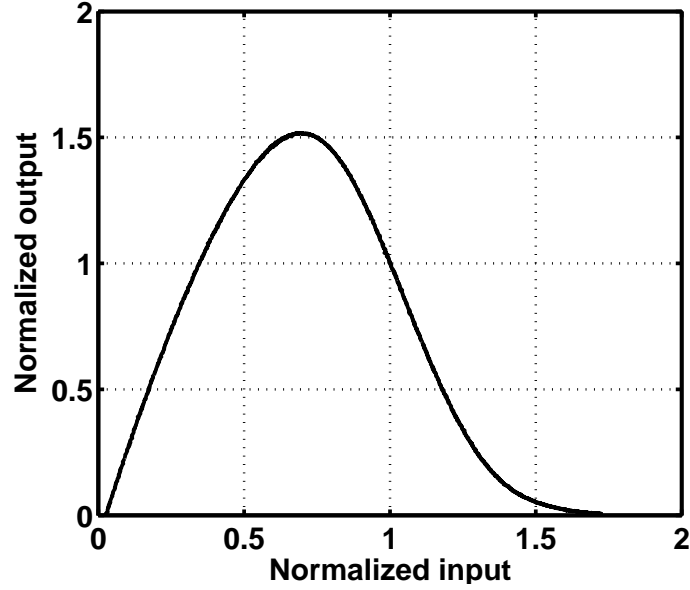
Figure 5.7: The nonlinear device characteristic curve. The input and output are normalized to the steady state.

where $U(t)$ is the voltage at the RC filter, T_d is the delay time in seconds, and $ND(U_{in})$ is the transfer function of the nonlinear device. The steady state voltage, U_s, satisfies $ND(U_s) = U_s$ and Fig. 5.7 plots ND/U_s versus U/U_s.

Introducing the dimensionless variable x, time t, and a dimensionless delay time τ,

$$\frac{U}{U_s} = x, \quad \frac{t}{R_0C_0} = t, \quad \frac{T_d}{R_0C_0} = \tau, \tag{5.12}$$

we obtain the equation,

$$\dot{x} = \lambda(x_\tau) - x, \tag{5.13}$$

with $\lambda(x) = ND/U_s$. In our experiments, R_0C_0 is 25.9 μs and $T_d \approx 180$ μs, that is, $\tau \approx 7.0$. We approximate the nonlinearity by

$$\lambda(x) = \frac{ax}{1 + x^{10}}. \tag{5.14}$$

100

Unlike the ideal delay unit, the practical delay unit shows different frequency responses and different losses at each output terminal. It is difficult to keep the other parameters the same while the delay time is varied. For example, if the signal at the end of the delay unit is attenuated, then Eqn. 5.13 and 5.14 become

$$\dot{x} = \frac{a(rx_\tau)}{1 + (rx_\tau)^{10}} - x,$$

(5.15)

where r describes the attenuation level of the signal. By substituting $x' = r\,x$, we obtain

$$\dot{x'} = \frac{ar\,x_\tau{'}}{1 + x_\tau{'}^{10}} - x'.$$

(5.16)

Therefore, the net effect of the loss along the delay unit can be regarded as a change in the linear gain of the nonlinear feedback term defined in Eqn. 5.14.

In the following section, we investigate the dynamics of the system as the linear gain is increased. The numerical value of the delay time τ is fixed at 7.0 in order to compare the numerical simulations and experimental measurements. We will not take the effect of the exponent in denominator, n, into consideration [74].

5.3 The Dependence of the Dynamics on the Linear Gain of the Nonlinear Feedback

Most of the studies about the Mackey-Glass system have been concerned with the dynamical changes as the delay time is varied, while few studies have focused on the role of the linear gain of the feedback term [33]. Since we have seen that the coupling strengths in the cross-coupled lasers with a fixed delay play an important

role to induce the instability in Chapter 2, the linear gain of the feedback term could serve as a control parameter for the dynamics of the Mackey-Glass system.

The Mackey-Glass equation that we are going to study is

$$\dot{x} = \frac{ax_\tau}{1 + x_\tau{}^{10}} - x \equiv F(x_\tau) - x, \tag{5.17}$$

where a is the linear gain of the feedback term. Instead of varying the delay time τ, we vary the linear gain a for a fixed delay time. The steady state is given by $F(x^*) = x^*$ and we can apply a similar method to that used in Eqn. 5.3 and Eqn. 5.4 to describe the dynamics of small perturbations around the nonzero steady state value, $x - x^* \propto e^{\lambda t}$. The corresponding characteristic equation is

$$\lambda + (9 - \frac{10}{a})e^{-\lambda t} + 1 = 0. \tag{5.18}$$

A Hopf bifurcation occurs when the eigenvalue becomes pure imaginary, i.e., $\lambda = i\omega$. Then Eqn. 5.18 can be separated into the real and the imaginary part such that

$$\text{Re} \quad : \quad 1 = -(9 - \frac{10}{a})\cos(\omega\tau), \tag{5.19}$$

$$\text{Im} \quad : \quad \omega = (9 - \frac{10}{a})\sin(\omega\tau). \tag{5.20}$$

Since we are interested in the real value of the steady state, the linear gain is restricted to be greater than 1, i.e., $a > 1$. The argument $(\omega\tau)$ is constrained to be in 2nd quadrant for $a > 10/9$ and in 4th quadrant for $1 < a < 10/9$.

Eqns. 5.19 and 5.20 can be rewritten as

$$w = -\tan(\omega\tau), \tag{5.21}$$

$$(9 - \frac{10}{a})^2 = 1 + \omega^2. \tag{5.22}$$
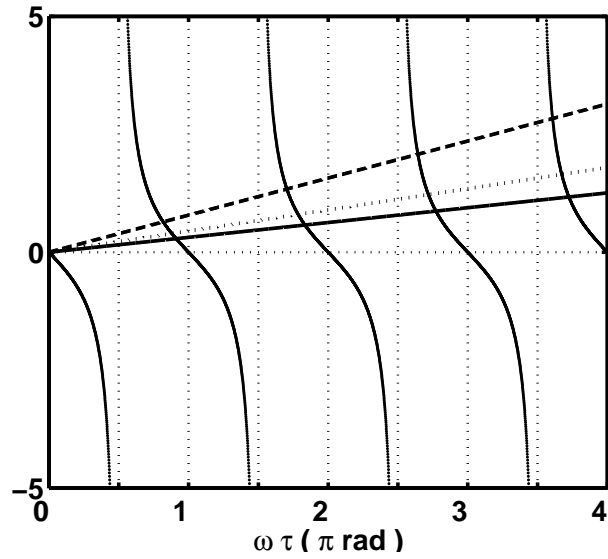
Figure 5.8: Plot of the left hand side and the right hand side of Eqn. 5.21 as a function of argument $(\omega\tau)$. The tangential curve corresponds to the right hand side. The lines correspond to the left hand side at different τ and the slope of lines is $1/\tau$. The dashed line corresponds to $\tau = 4.0$, the dotted line to $\tau = 7.0$, and the solid line to $\tau = 10.0$.
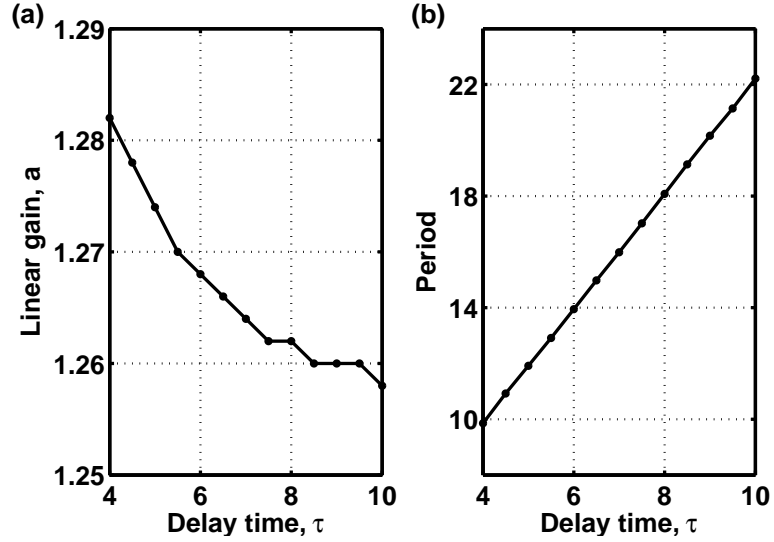
Figure 5.9: The onset of periodic oscillations. (a) The critical value of the linear gain versus the delay time. (b) The period of the oscillations versus the delay time. The integration time step is $h = 0.005$.

The angular frequency of the periodic signal can be calculated by solving Eqn. 5.21 and the value of the linear gain at the onset of instability for the specific angular frequency can be calculated from Eqn. 5.22. Fig. 5.8 plots the left hand side and the right hand side of Eqn. 5.21 for different values of τ. The intersection points between the tangent curve and the line for given τ correspond to the solutions. For a large enough delay time, the solutions of Eqn. 5.21 are approximated by

$$w = w_n = \frac{n\pi}{\tau} \equiv \frac{2\pi}{T_n}, \ n = 1, 3, 5, \ldots, \tag{5.23}$$

where $T_n = 2\tau/n$ is the period of the oscillations. The fundamental period is, therefore, $T_1 = 2\tau$, and the onset occurs at $a = 10/(9 - \sqrt{1 + \omega^2})$.

In Fig. 5.9, we show the critical value of the linear gain a, and the period of

104

the oscillations with the delay time τ, varying from 4.0 to 10.0. The linear gain is increased by the amount of $\Delta a = 0.002$, and the critical value of the linear gain is defined as when the amplitude of the oscillations becomes greater than a specific constant, 0.01 in this case. Fig. 5.9(a) shows that the value of the linear gain at the onset approaches $10/(9 - \sqrt{1}) = 1.25$ as the delay time is increased. In Fig. 5.9(b), we observe that the period of oscillations near the onset is linearly proportional to the delay time.

Since the delay time in our electronic circuit corresponds to $\tau \approx 7$ in dimensionless units, we simulate Eqn. 5.17 at different values of the linear gain a with $\tau = 7$. In Fig. 5.10(a), with $a = 1.26$ which is very near the onset of the periodic oscillations, and the time series looks almost like a steady state. We can observe a very weak peak of the power at the fundamental frequency, i.e., $f_1 = 1/T_1$. When a is increased to 1.32 in Fig. 5.10(b), we can clearly see the periodic oscillations at the fundamental frequency. At $a = 1.36$ in Fig. 5.10(c), an additional frequency component appears at $f_1/2$ in the power spectrum and this corresponds to the period doubling. The period 2 oscillations are obvious in the time series of Fig. 5.10(d) at $a = 1.38$. In Fig. 5.10(e), we observe a new frequency component at $f_1/4$ in the power spectrum and the period 4 oscillations in the time series.

For values of a greater than 1.42, the time series is chaotic and the power spectrum shows a broad band. In Fig. 5.10(f), we still see the remnants of periodic oscillations in the power spectrum when a is near the onset of chaos. This remnant disappears as a increases away from the chaotic onset and Fig. 5.10(i) shows fully developed chaos. Fig. 5.11 plots the phase portraits of $x(t)$ versus $x(t - \tau)$ for the
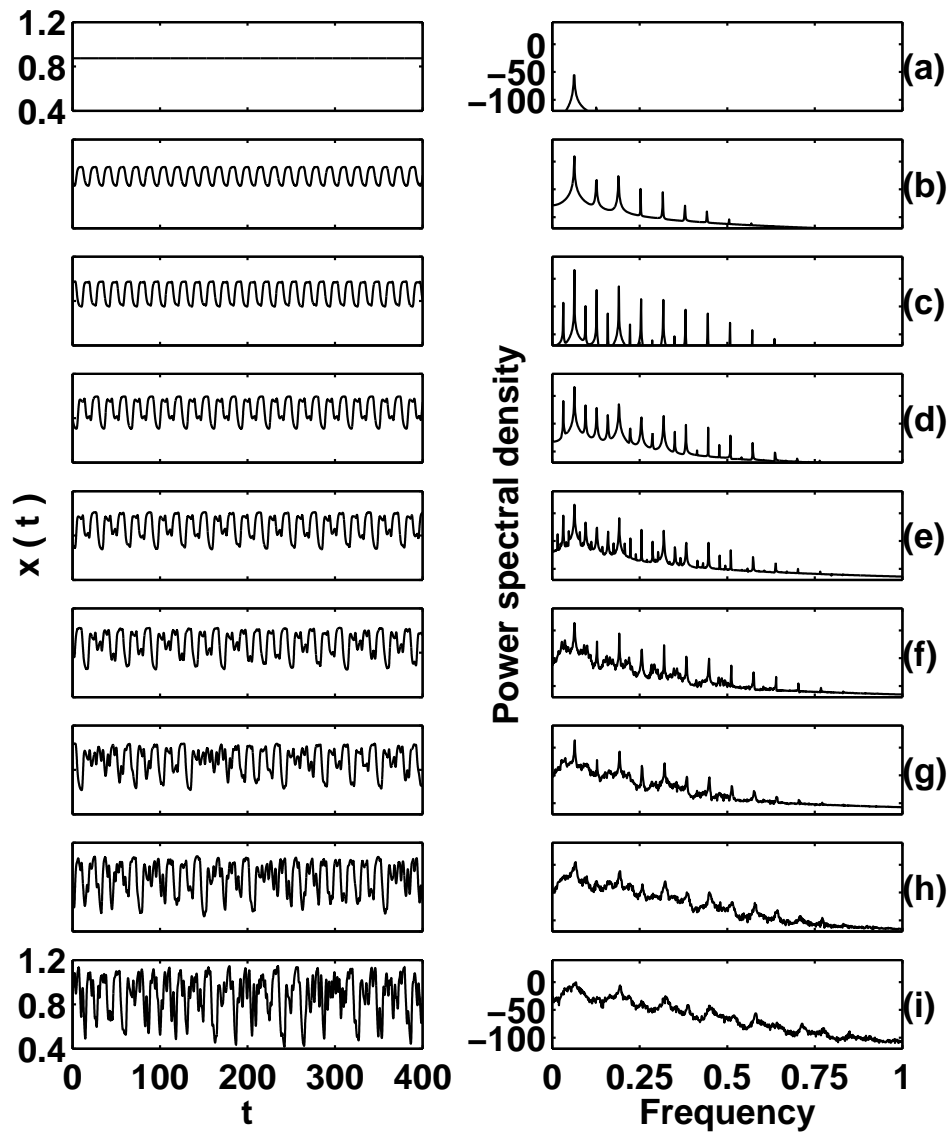
Figure 5.10: Time series (left) and power spectral densities (right) at different values of the linear gain. (a) $a = 1.26$, (b) $a = 1.32$, (c) $a = 1.36$, (d) $a = 1.38$, (e) $a = 1.40$, (f) $a = 1.42$ (g) $a = 1.44$, (h) $a = 1.50$, and (i) $a = 1.60$. The spectra are obtained using a FFT algorithm and are averages of spectra from 10 consecutive 8192 sample points. The integration time step is $\Delta t_{\text{integration}} = 0.005$ and the sampling time is $\Delta t_{\text{sample}} = 0.1$. A constant initial function, $x_0 = 0.9$, is used on $(-\tau, 0)$ with $\tau = 7$.
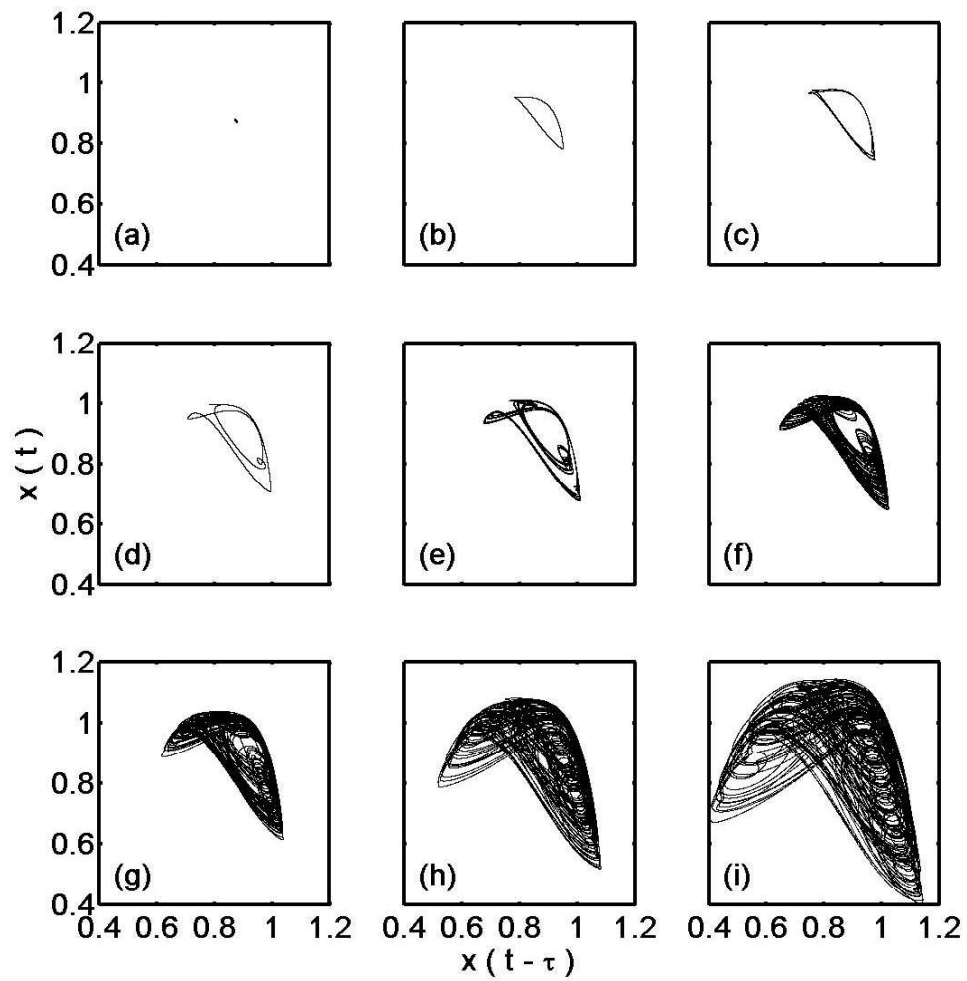
Figure 5.11: Phase portraits of $x(t)$ versus $x(t - \tau)$ at (a) $a = 1.26$, (b) $a = 1.32$, (c) $a = 1.36$, (d) $a = 1.38$, (e) $a = 1.40$, (f) $a = 1.42$ (g) $a = 1.44$, (h) $a = 1.50$, and (i) $a = 1.60$. $\Delta t = 0.005$, $x_0 = 0.9$ on $(-\tau, 0)$, $\tau = 7$.
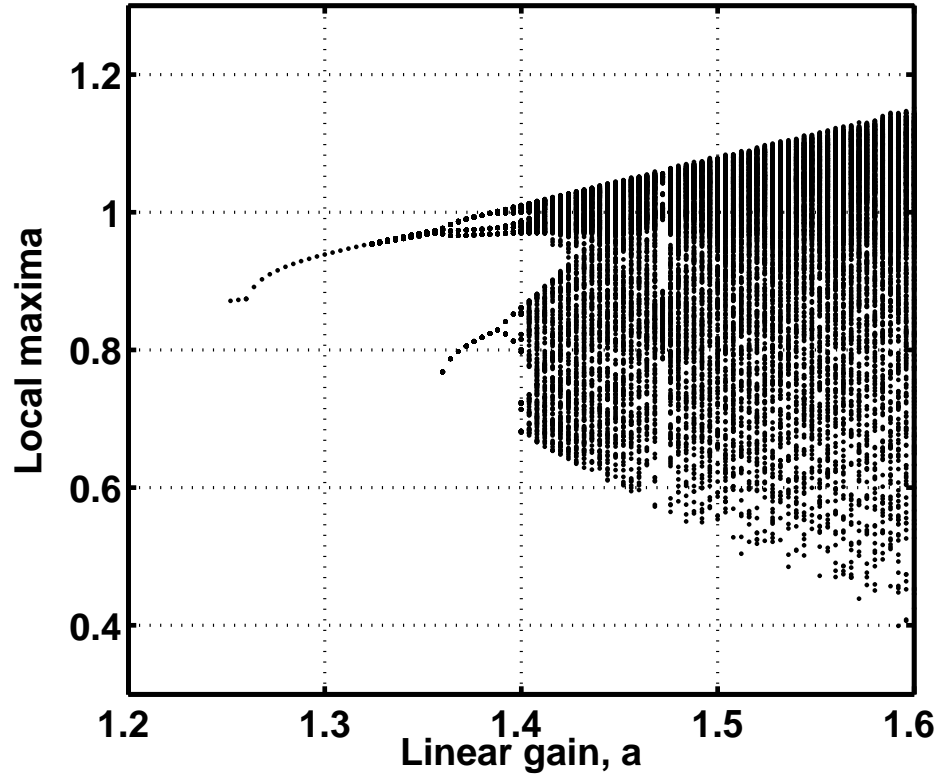
Figure 5.12: Bifurcation diagram of the local maxima of the time series as linear gain a varies from 1.2 to 1.6. The integration time step is $\Delta t_{\text{integration}} = 0.005$. $x_0 = 0.9$ on $(-\tau, 0)$ with $\tau = 7.0$.

values of a used in Fig. 5.10 and we see the route to chaos through the periodic doubling processes, as explained above. In Fig. 5.12, we show the bifurcation diagram by plotting the local maxima of the time series as the linear gain a varies from 0.6 to 0.8.

In the experiments, we vary the linear gain of the nonlinear device by changing the resistance of the potentiometer. The same route to chaos shown in the numerical simulations can be seen experimentally.

5.4 Chaotic Signal Generation

So far, we have investigated how the dynamics of Mackey-Glass system depend on different parameters. First, the delay time was varied for the fixed value of the linear gain, then the linear gain was varied for a fixed delay time. Both the delay time and the linear gain can be used as a control parameter to understand the dynamics of the system and induce a period doubling route to chaos. For the remaining part of this dissertation, we will focus on the chaotic signal generated by the Mackey-Glass system for a given parameter set.

In this section, we generate chaotic signals experimentally and numerically. In order to make a comparison between the experimental observations and the numerical simulations, we determine matching parameters and carry out proper conversions in the variables. As mentioned in the previous section, the linear gain of the nonlinear feedback term in the Eqn. 5.17 is related to both the gain of the nonlinear device and the losses in the delayed feedback loop in the experiments.

Fig. 5.13(a) shows the chaotic time series taken from our Mackey-Glass analog circuit. 4096 sample points are recorded at 10^5 samples per second for each time window. The power spectrum is obtained by averaging the individual power spectrum from 5 time windows in Fig. 5.13(b). Fig. 5.13(c) is the phase portrait of the normalized voltage signal $U(t)/ < U >$ versus the delayed normalized voltage signal $U(t - T_d)/ < U >$. We normalize the signals to their mean value.

From the power spectrum shown in Fig. 5.13(b), we see that there exists the remnants from the periodic oscillations since there are peaks in addition to the
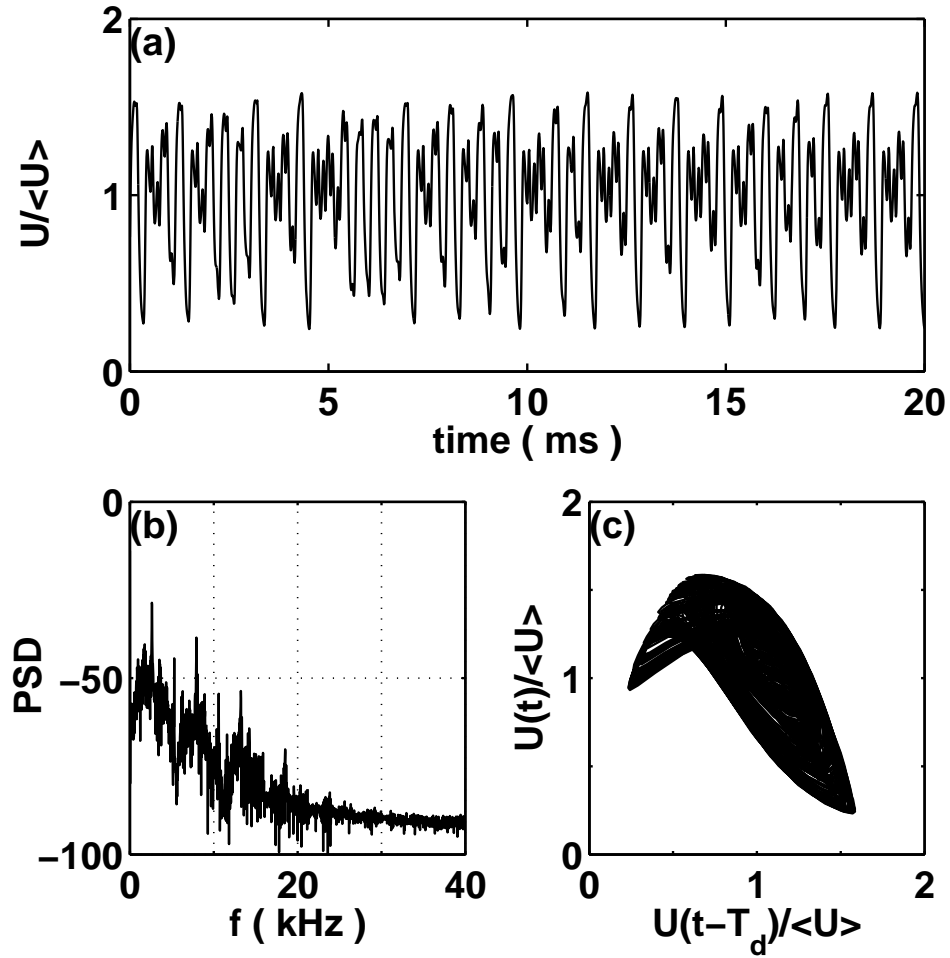
Figure 5.13: (a) The chaotic time series, (b) power spectral density (PSD) and (c) phase portrait generated by a Mackey-Glass analog circuit. The sampling time is 10 μs and 4096 sample points are recorded for each time window. The PSD is the average of individual PSD from 5 windows.
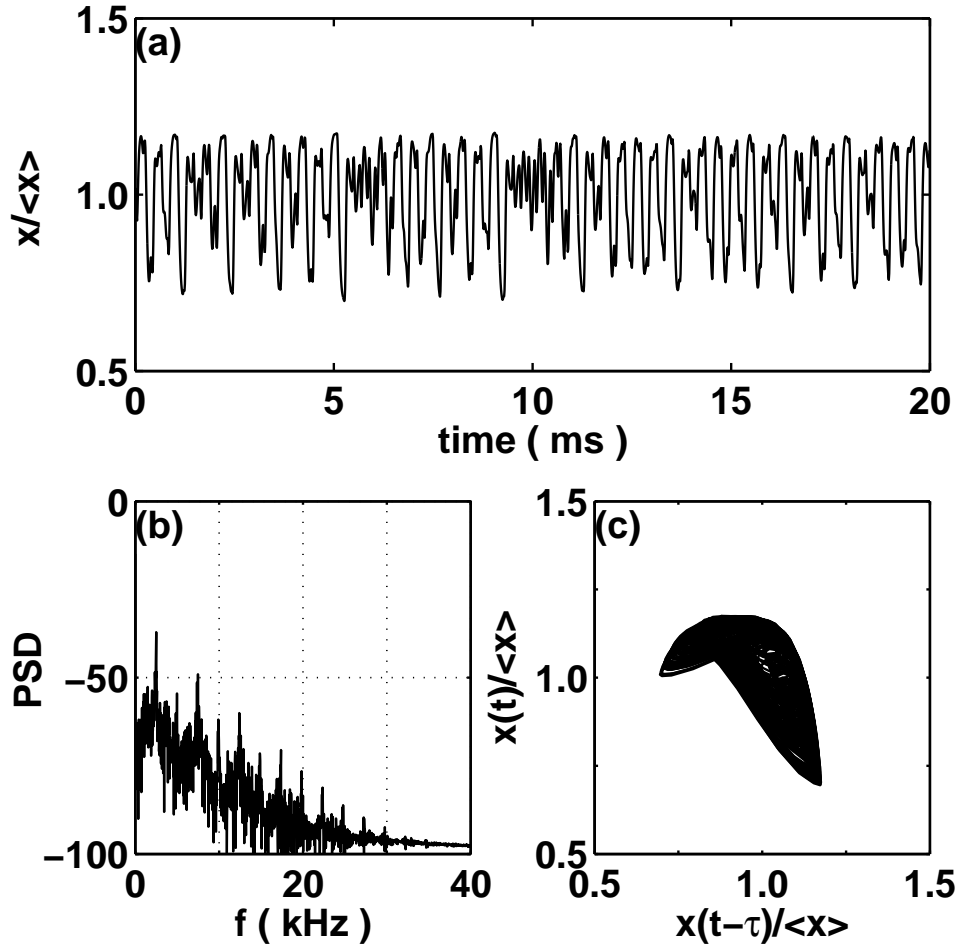
Figure 5.14: (a) The chaotic time series, (b) power spectral density (PSD) and (c) phase portrait generated by numerical integration of Eqn. 5.17. The integration time step is $\Delta t_{\text{integration}} = 0.005$ and the sampling time is $\Delta t_{\text{sampling}} = 0.385$ in dimensionless units.

broad band spectrum. The dominant peak is located at 2.7 kHz which corresponds to the fundamental frequency calculated from the linear stability analysis, i.e., $f_1 = (2T_d)^{-1} = (2 \times 180\mu s)^{-1} \approx 2.8\ kHz$. When the value of the linear gain is chosen to be 1.44, the shapes of the power spectrum and the phase portrait obtained from the numerical simulations match those from the experiments as shown in Fig. 5.14. The dimensionless time from the numerical simulations is converted to the physical time in seconds by the relationship given in Eqn. 5.12, i.e., t [sec] $= R_0 C_0 \times t$ [dimensionless] with $R_0 C_0 = 25.9\ \mu s$.

Using the chaotic signal generated in this section as a standard drive signal, we will study the synchronization of a receiver signal under different conditions in the following chapter.

Chapter 6

Synchronization of Unidirectionally Coupled Mackey-Glass Circuits

Chaotic signals are extremely complex and very sensitive to initial conditions, which make them unpredictable to an arbitrary observer [75]. This unpredictability, however, can be driven by deterministic models, and therefore can be controlled. There have been numerous studies on the control of chaos both theoretically and experimentally [76, 77, 78, 79, 80, 81]. The synchronization of chaotic system has been investigated extensively because of its potential applications in communication [38, 39, 40, 41, 42, 43, 44, 45, 46]. In this chapter, we will investigate the synchronization of two unidirectionally coupled Mackey-Glass circuits.

6.1 Open-loop and Closed-loop Configuration for the Receiver

Recently, the concept of synchronization of chaos has been demonstrated in theoretical, numerical, and experimental research. One example is synchronization of chaos in semiconductor lasers with delayed optoelectronic feedback [82, 83, 84]. Also there are examples of synchronization in chaotic external cavity lasers [85]. In both cases, the quality of synchronization has been studied when the receiver is set in either an open-loop or closed-loop configuration. In an open-loop configuration, the receiver is a solitary laser, whereas in the closed-loop configuration the receiver is a semiconductor laser with delayed optoelectronic feedback or a chaotic external

x(t)

G

x(t-τ)

τ

τ

(1- c) y(t-τ)

G

c x(t-τ)

y(t)

+

Driver   Receiver
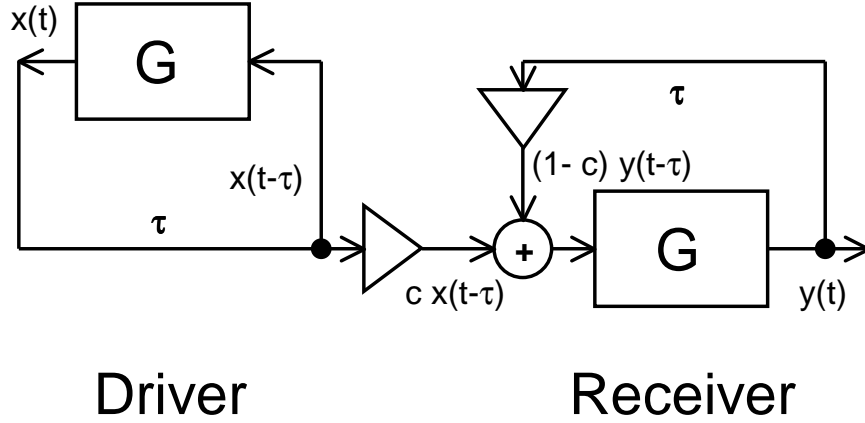
Figure 6.1: Block diagram of two unidirectionally coupled Mackey-Glass systems. G denotes the nonlinear system function of the Mackey-Glass system, which includes nonlinear feedback and a low pass filter.

cavity laser. In both systems, the open-loop configuration shows a better quality of synchronization of chaos.

In this section, we assume that the receiver dynamical system is identical to the driver dynamical system. Fig. 6.1 shows the schematic diagram of two unidirectionally coupled identical Mackey-Glass systems. The driver has a feedback loop and the dynamics are described by a Mackey-Glass model. At the receiver, the coupled signal from the driver, together with the feedback signal from the receiver, is used to drive the receiver. A factor c indicates the percentage of the signal from the driver, whereas $(1-c)$ indicates the percentage of the feedback from the receiver output in the total driving signal to the receiver [83, 86]. The c factor can vary from 0 to 1. When $c = 1$, the receiver is in an open loop. When $c = 0$, the receiver is completely isolated from the driver.

Since we assume identical systems for the receiver and the driver, the equations

for the unidirectionally coupled Mackey-Glass system are given by

$$\frac{dx(t)}{dt} = \frac{a\ x(t-\tau)}{1+x(t-\tau)^n} - x(t), \tag{6.1}$$

$$y_{in}(t) = cx(t-\tau) + (1-c)y(t-\tau), \tag{6.2}$$

$$\frac{dy(t)}{dt} = \frac{a\ y_{in}(t)}{1+y_{in}(t)^n} - y(t), \tag{6.3}$$

where x is the driver output, y is the receiver output. Each system evolves indepen-
dently from the constant initial functions (x_0, y_0) for t on $(-\tau, 0)$ until the coupling
is "on". For $t > t_{\text{on}}$, the two systems are coupled as described in Eqns. 6.1 - 6.3.

For $a = 2$, $n = 10$, and $\tau = 7$, we calculated a cross-correlation coefficient

$$\rho = \frac{<(x(t)-<x(t)>)(y(t)-<y(t)>)>}{<|x(t)-<x(t)>|^2>^{1/2}<|y(t)-<y(t)>|^2>^{1/2}}, \tag{6.4}$$

where $< \cdot >$ denotes time averaging. The cross-correlation coefficient ρ is calculated
for different values of c in Fig. 6.2. As c varies from 0 to 1, ρ increases from 0 to 1.
ρ increases dramatically from ~ 0.2 to 1 as c increases from 0.2 to 0.3.

For the remaining part of this chapter, we will study the characteristics of
synchronization of chaos using an open-loop configuration for the receiver circuit.

6.2   Synchronization with Parameter Mismatch

In the previous chapter, we introduced a Mackey-Glass analog circuit and studied
the change of the dynamical behavior as a function of the system parameters. In this
section, we introduce two unidirectionally coupled Mackey-Glass analog circuits with
an open-loop receiver configuration. The quality of synchronization with parameter
mismatch is investigated through numerical simulations.
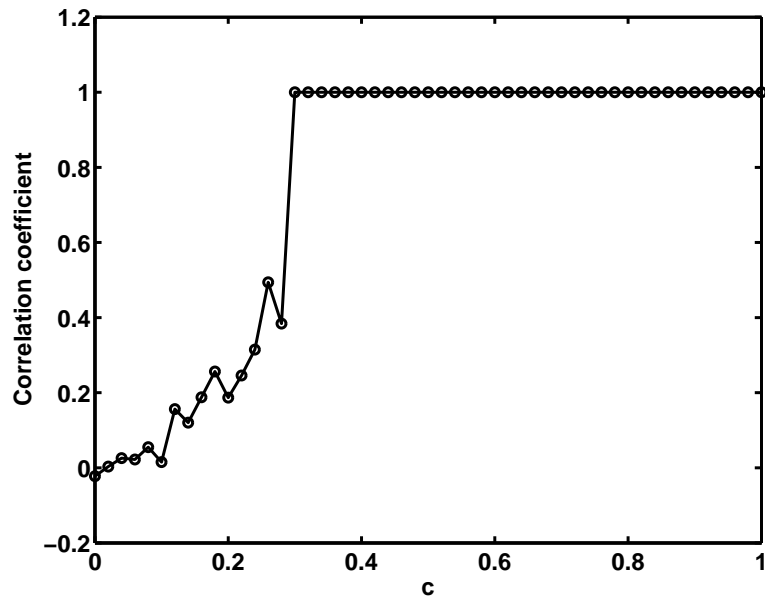
Figure 6.2: Cross-correlation coefficient ρ versus c factor obtained by numerically integrating Eqns. 6.1 - 6.3. $\Delta t_{\text{integration}} = 0.005$, $x_0 = 0.9$ and $y_0 = 1.1$ for t on $(-\tau, 0)$. The coupling is "on" for $t > 200$ and the time average is taken for $500\tau < t < 1000\tau$.

6.2.1 Unidirectionally Coupled Mackey-Glass Analog Circuits

A block diagram of two unidirectionally coupled Mackey-Glass circuits is shown in Fig. 6.3. The driver consists of a nonlinear device, a low pass filter and a delay line. The output of the driver $TX(t)$, is the delayed feedback signal $U_1(t - T_d)$, where T_d is the feedback delay time. Assuming there is channel distortion in the transmission line, the receiver signal $U_2(t)$ is driven by the distorted signal $TX'(t)$. We ignore the transmission time for the driver output to reach the receiver.

The dynamics of the circuits are described by coupled delay-differential equations

$$R_1 C_1 \frac{dU_1(t)}{dt} = ND_1(U_1(t - T_d)) - U_1(t), \tag{6.5}$$

$$R_2 C_2 \frac{dU_2(t)}{dt} = ND_2(TX'(t)) - U_2(t), \tag{6.6}$$

where R_1, R_2 are resistances, C_1, C_2 are capacitances, and ND_1, ND_2 are the transfer functions of each nonlinear device. We introduce dimensionless variables and dimensionless parameters, as in Eqn. 5.12

$$\frac{U_1(t)}{U_{1s}} = x(t), \quad \frac{U_2(t)}{U_{1s}} = y(t), \quad \frac{TX'(t)}{U_{1s}} = y_{in}(t),$$

$$\frac{t}{R_1 C_1} = t, \quad \frac{T_d}{R_1 C_1} = \tau, \quad \frac{R_2 C_2}{R_1 C_1} = \frac{1}{b}, \tag{6.7}$$

where $x(t)$ is the driver signal, $y(t)$ is the receiver signal, $y_{in}(t)$ is the transmitted signal, and b corresponds to the mismatch in RC constants. The coupled equations become

$$\frac{dx}{dt} = \frac{a\, x_\tau}{1 + x_\tau{}^n} - x, \tag{6.8}$$

$$\frac{dy}{dt} = b \left[\frac{a'\, y_{in}}{1 + y_{in}{}^{n'}} - y \right], \tag{6.9}$$

117
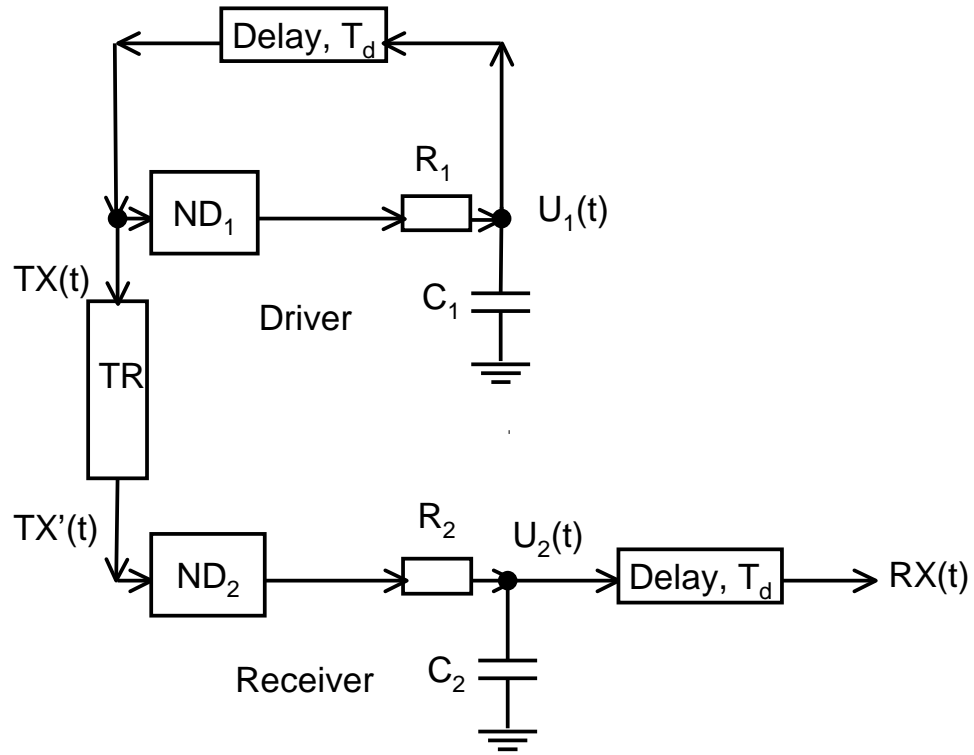
Figure 6.3: Block diagram of two unidirectionally coupled Mackey-Glass analog circuits with an open-loop configuration. ND_1, ND_2 are nonlinear devices; T_d is delay time in seconds; R_1, R_2 are resistors; C_1, C_2 are capacitors; TR is the transmission channel; U_1, U_2 are voltage signals at the low pass filter. TX is the signal output from the driver, TX' is the transmitted signal, and RX is the signal output from the receiver [87].

where a, a' are the linear gains of each nonlinear device.

In the remaining part of this section, we will consider the linear amplification/attenuation in transmission and numerically investigate the characteristics of the synchronization with parameter mismatch between the driver and the receiver. In the following section, we will consider the bandwidth limitation in transmission and characterize the synchronization properties both experimentally and numerically.

6.2.2 Parameter Mismatch

Assuming linear amplification or attenuation in transmission,

$$TX(t)' = \kappa TX(t) = \kappa U_1(t - T_d) \quad \text{or} \quad y_{in}(t) = \kappa x(t - \tau), \tag{6.10}$$

where κ is the coupling strength between the driver and the receiver. The delayed driver signal $x(t - \tau)$ is linearly amplified ($\kappa > 1$) or attenuated ($\kappa < 1$) to drive the receiver, whereas $x(t - \tau)$ is directly fed back to the driver. The dynamics of the system are described by

$$\frac{dx}{dt} = \frac{a\ x_\tau}{1 + x_\tau{}^n} - x, \tag{6.11}$$

$$\frac{dy}{dt} = b\left[\frac{a'\ (\kappa\ x_\tau)}{1 + (\kappa\ x_\tau)^{n'}} - y\right]. \tag{6.12}$$

From now on, we will focus on the case where $n' = n = 10$, $\tau = 7$. The value of a will be chosen to be either 2.0 which corresponds to the fully developed chaos, or 1.44 which is near the onset of the chaos (where the power spectrum has periodic peaks in addition to the broad band).

Since the dynamics of the driver are isolated from the dynamics of the receiver, we integrate Eqn. 6.11 and obtain the entire driver signal at a given value of a. The receiver signal is obtained by integrating Eqn. 6.12 with a given set of parameters (a', b, κ). A fixed step fourth-order Runge-Kutta method is used with an integration time step $\Delta t_{\text{integration}} = 0.005$. The linear interpolation is used for the required two midpoint evaluations of the delayed variable and we generate the drive signal starting with a constant initial condition $(x_0 = 0.9)$ on $(-\tau, 0)$. The coupling between the driver and the receiver will be "on" from $t = 200\tau$ and the signals generated between $400\tau < t \leq 900\tau$ are used for numerical data analysis.

The dynamics of the receiver change at different values of parameters a', b, and κ. a'/a describes the level of mismatch in the linear gain of the nonlinear devices and b describes the level of mismatch in the RC constants. When $a'/a = 1$ and $b = 1$, the driver circuit and the receiver circuit are identical. On the other hand, κ describes the coupling strength between the driver and the receiver. For $\kappa < 1$, the signal will be linearly attenuated during the transmission, while for $\kappa > 1$, the signal will be linearly amplified. The time-shifted cross-correlation coefficient, introduced in Eqn. 4.1,

$$C(\Delta t) = \frac{< [x(t)- < x(t) >][y(t + \Delta t)- < y(t) >] >}{< |x(t)- < x(t) > |^2 >^{1/2}< |y(t)- < y(t) > |^2 >^{1/2}}, \tag{6.13}$$

is calculated to characterize the synchronization of chaos [84].

The synchronization of identical systems without linear attenuation/amplification during transmission, corresponding to $a'/a = b = \kappa = 1$, is shown in Fig. 6.4. In Fig. 6.4(a) and (c), the driver signal $x(t)$ and the receiver signal $y(t)$ are identical.
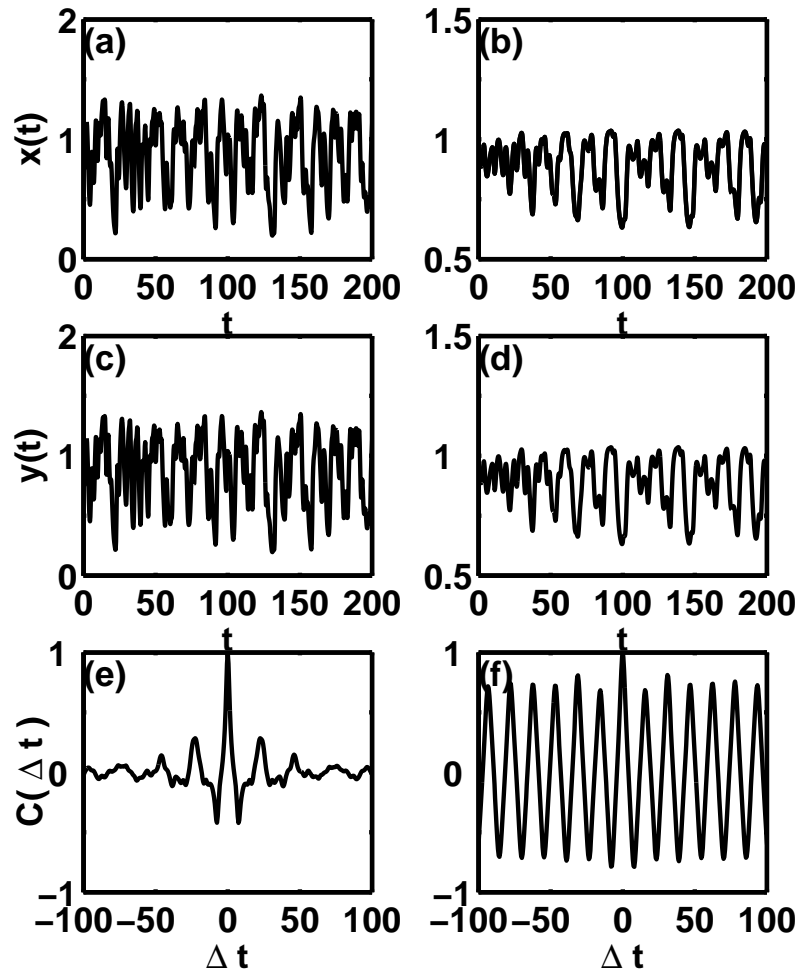
Figure 6.4: Synchronization of identical systems without linear attenuation/amplification during transmission ($a'/a = b = \kappa = 1$). (a) Time series of the driver signal $x(t)$, (c) time series of the receiver signal $y(t)$, and (e) the time-shifted cross-correlation coefficient $C(\Delta t)$ at $a = 2.0$. (b), (d), and (f) are the corresponding results at $a = 1.44$. The time t and the time shift Δt are measured in dimensionless units.

In Fig. 6.4(e) and (f), the shifted cross-correlation coefficient $C(\Delta t)$ is maximum at $\Delta t = 0$, i.e., $C(0) = 1$, which corresponds to perfect synchronization. $C(\Delta t)$ reduces to zero as Δt gets further from zero at $a = 2$, whereas for $a = 1.44$ it oscillates periodically with time interval equal to the fundamental period of the MG system, $T_1 \sim 2\tau$.

The mismatch in the linear gain factor a'/a, as well as the mismatch in the RC constant b, does not noticeably change the shape of $C(\Delta t)$. However, $C(\Delta t)$ changes significantly with change in the coupling strength κ. Fig. 6.5 shows $C(\Delta t)$ versus time shift, Δt, at $\kappa = 0.25$ (top), 1.0 (middle), and 2.0 (bottom). For $\kappa = 0.25$, the coupling is weak and there is linear attenuation in the transmission line, whereas for $\kappa = 2.0$, the coupling is strong with linear amplification in the transmission line. In Fig. 6.5(a) and (b), for $\kappa = 0.25$, a maximum peak is observed at $\Delta t \sim \tau$. In Fig. 6.5(e) and (f) with $\kappa = 2.0$, a maximum peak is observed at $\Delta t \sim 2\tau$ and a minimum valley at $\Delta t \sim \tau$.

Fig. 6.6 and Fig. 6.7 show how the maximum value of the shifted cross-correlation coefficient, $C(\Delta t = T_{max})$, and the corresponding time shift, T_{max}, vary with parameter mismatch and the coupling strength at $a = 2.0$ and 1.44. The circles show $C(T_{max})$ and T_{max} when a'/a is varied under the conditions $b = 1$ and $\kappa = 1$. The squares show $C(T_{max})$ and T_{max} when b is varied with $a'/a = 1$ and $\kappa = 1$. As discussed above, a mismatch in a'/a and b does not change the quality of synchronization, and the driver signal $x(t)$ and the receiver signal $y(t)$ remain very well synchronized. On the other hand, the variation in the coupling strength κ, indicated by the triangles, changes the property of synchronization significantly. The effect
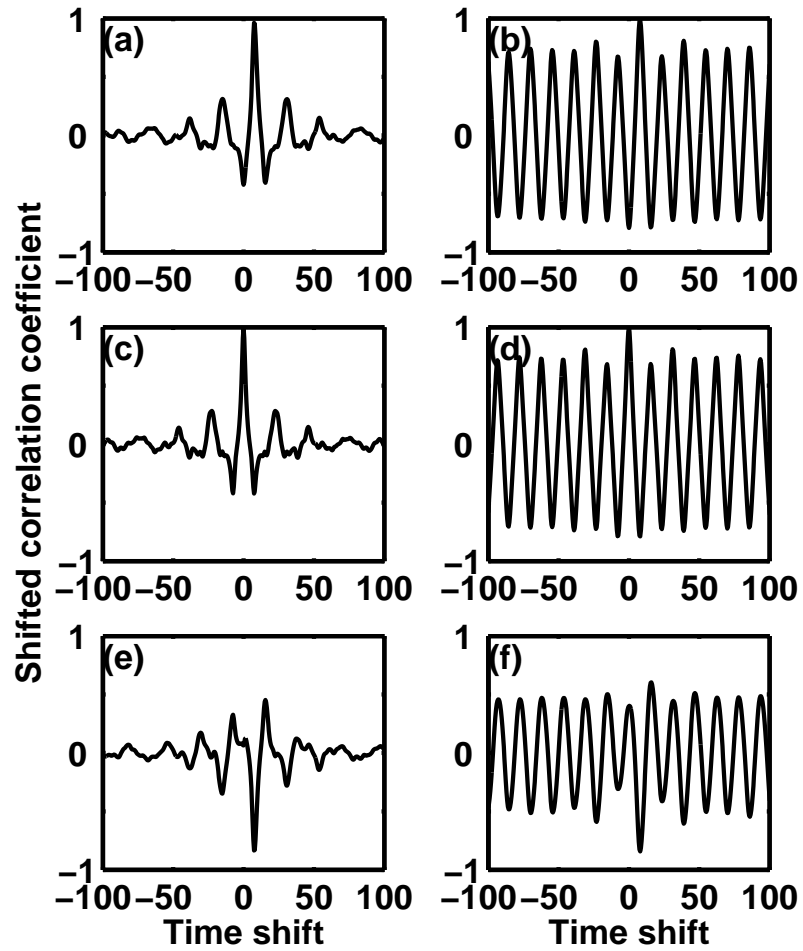
Figure 6.5: Time-shifted cross-correlation coefficient, $C(\Delta t)$, at different values of the coupling strength κ. (a) $\kappa = 0.25$, (c) $\kappa = 1.0$, and (e) $\kappa = 2.0$ for $a = 2.0$. (b), (d), and (f) are the corresponding results for $a = 1.44$.
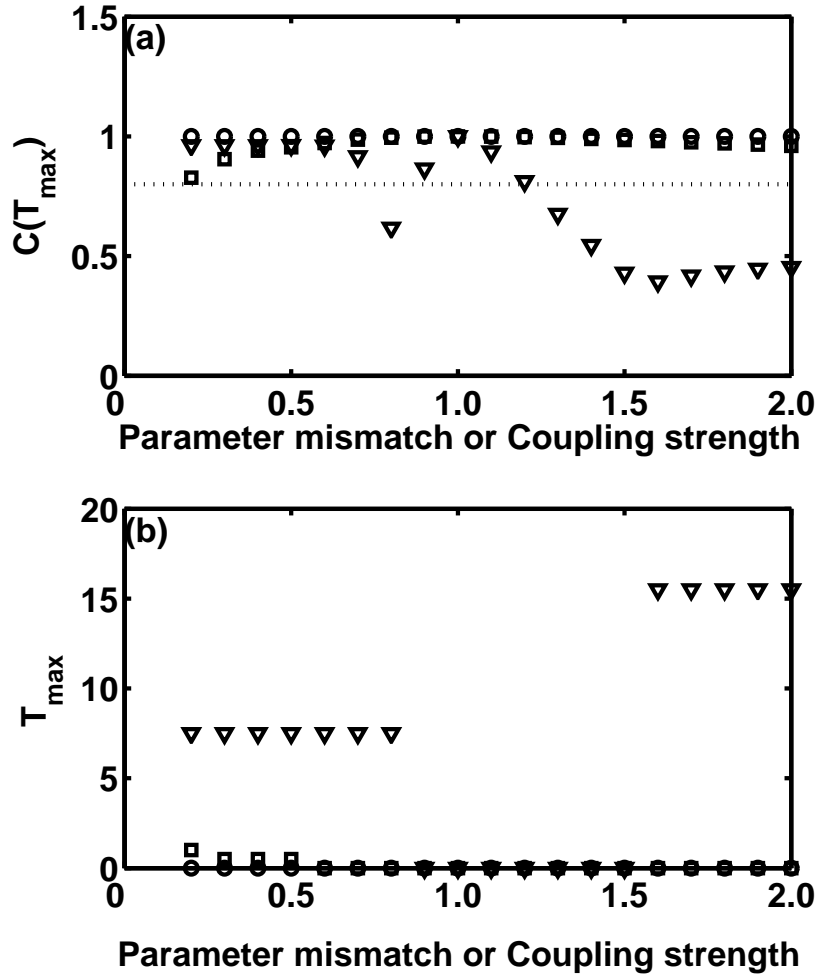
Figure 6.6: (a) The maximum of the shifted cross-correlation coefficient and (b) the corresponding time shift at maximum versus parameter mismatch or coupling strength at $a = 2.0$. The circles are for the mismatch in the linear gain of the nonlinear feedback a'/a, the squares are for the mismatch in the RC constant b, and the triangles are for the variation in the coupling strength κ. The line in (a) is drawn at $C = 0.8$. $a'/a = 1$ and $b = 1$ corresponds to the identical circuits. For $\kappa > 1$ ($\kappa < 1$), the signal is linearly amplified (attenuated) in the transmission line.
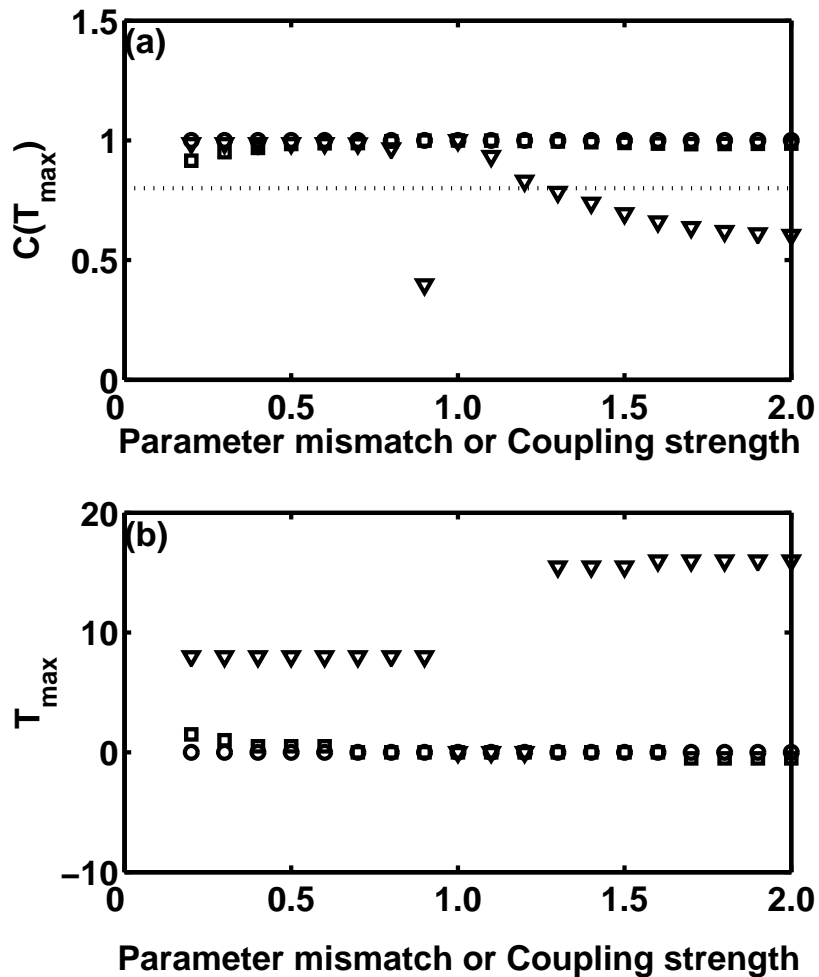
Figure 6.7: (a) The maximum of the shifted cross-correlation coefficient and (b) the corresponding time shift at maximum versus parameter mismatch or coupling strength at $a = 1.44$. The circles are for the mismatch in the linear gain of the nonlinear feedback a'/a, the squares are for the mismatch in the RC constant b, and the triangles are for the variation in the coupling strength κ. The line in (a) is drawn at $C = 0.8$. $a'/a = 1$ and $b = 1$ corresponds to the identical circuits. For $\kappa > 1$ ($\kappa < 1$), the signal is linearly amplified (attenuated) in the transmission line.

of the coupling strength on the synchronization will be discussed in details in the following section.

In the pair of Mackey-Glass circuits used in the experiments, the low pass filter components and the nonlinear devices are matched very carefully. The range of parameter mismatch a'/a and b, therefore, falls well within $[0.5, 1.5]$. The observations from the numerical simulation indicate that the effect of mismatching these parameters on the synchronization of coupled Mackey-Glass circuits is not as important as that of the coupling strength. From now on, we will focus on the case of identical circuits, where $a' = a$ and $b = 1$.

6.2.3 Linear Amplification or Attenuation in the Transmission Line

The triangles in Fig. 6.6 and Fig. 6.7 show how the maximum value of the shifted cross-correlation coefficient and the corresponding time shift vary with coupling strength, κ. The synchronization quality is the best when $\kappa = 1$. As κ moves away from 1, the synchronization between the driver signal $x(t)$ and the receiver signal $y(t)$ degrades. In Fig. 6.6 with $a = 2.0$, the maximum correlation occurs at $T_{max} \sim \tau$ for $\kappa < 0.8$ with $C(T_{max})$ close to 1, and at $T_{max} \sim 2\tau$ for $\kappa > 1.5$. As we will see in the following paragraph, these cases are related to the direct response of the receiver to the input signal. The transition from synchronization to the direct response occurs when κ is close to 1 with $a = 1.44$.

In Figs. 6.8 - 6.10, a comparison of the time series and the correlation plots are shown for different coupling strength κ corresponding to Fig. 6.5(a), (c) and (e), respectively. Fig. 6.8(a) shows the comparison between the driver signal $x(t)$ and

the receiver signal $y(t)$. Fig. 6.8(b) shows the comparison between the driver signal $x(t)$ and the receiver signal after the delay time τ, $y(t+\tau)$. Since the receiver at time $(t+\tau)$ is driven by the input signal $\kappa x(t+\tau-\tau) = \kappa x(t)$, Fig. 6.8(b) shows the direct modulation response of the receiver to the input signal at each time. Fig. 6.8(c) and (d) shows the corresponding correlation plots. At $\kappa = 0.25$, therefore, the receiver signal is directly modulated by the input signal. In other words, the receiver signal is strongly correlated to the driver signal with a time shift τ. With weak coupling or with strong attenuation during transmission, the input signal to the receiver is very small and the response of the receiver is determined by the transfer characteristics of nonlinear device. Since the slope of the transfer function at a small amplitude is positive, a positive linear modulation occurs at $\kappa = 0.25$, i.e., $\Delta y(t) \propto +\Delta x(t - \tau)$.

In Fig. 6.9, the driver signal $x(t)$ and the receiver signal $y(t)$ are perfectly synchronized. In Fig. 6.9(d), the correlation plot of the receiver signal $y(t + \tau)$ versus the corresponding input signal $x(t)$ reconstructs the typical Mackey-Glass attractor. Fig. 6.10 shows a similar comparison as in Fig. 6.8 under the condition of $\kappa = 2$. The receiver signal is again strongly correlated to the driver signal with a time shift τ. However, this case corresponds to a negative linear modulation with $\Delta y(t) \propto -\Delta x(t-\tau)$. With amplification in the transmission line, the input signal to the receiver becomes large. Since the slope of the transfer function of the nonlinear device is negative at a large amplitude, a negative linear modulation occurs at $\kappa = 2$. As a result, the direct response of the receiver to the input signal at weak coupling gives a positive correlation coefficient, $C(\tau) > 0$, whereas with strong coupling, the correlation coefficient is negative, $C(\tau) < 0$.
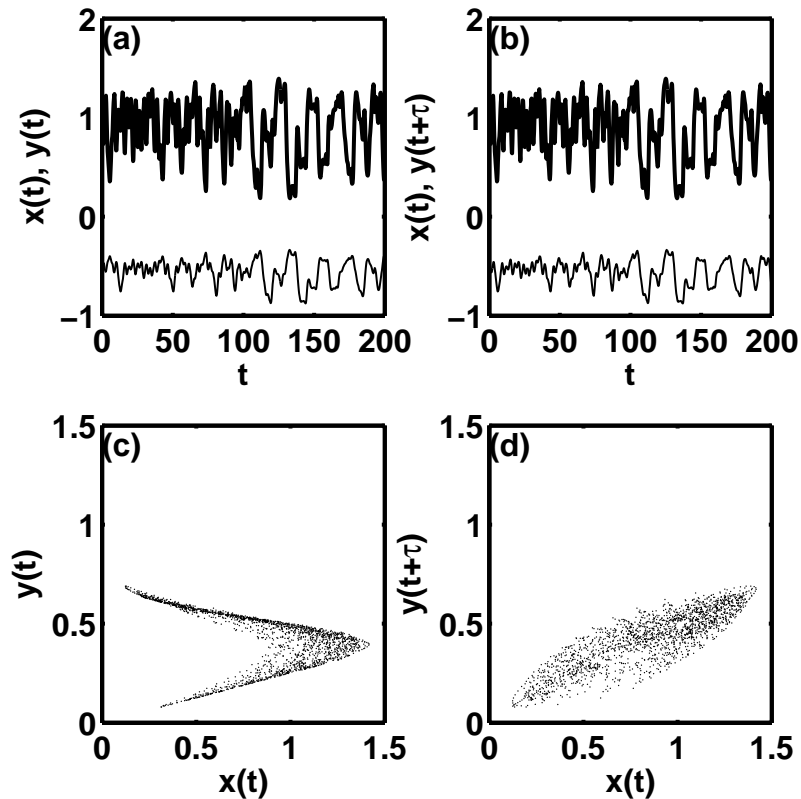
Figure 6.8: Comparison of the time series and the correlation plots for $\kappa = 0.25$ with $b = 1$, $a' = a = 2.0$, as in Fig. 6.5(a). (a) The time series of the driver signal, $x(t)$, (upper trace) and the receiver signal, $y(t)$, (lower trace). (b) The time series of the driver signal, $x(t)$, (upper trace) and the shifted receiver signal, $y(t+\tau)$, (lower trace). (c) The correlation plot between the two traces in (a). (d) The correlation plot between two traces in (b). $y(t+\tau)$ is driven by $x(t)$ in our configuration.
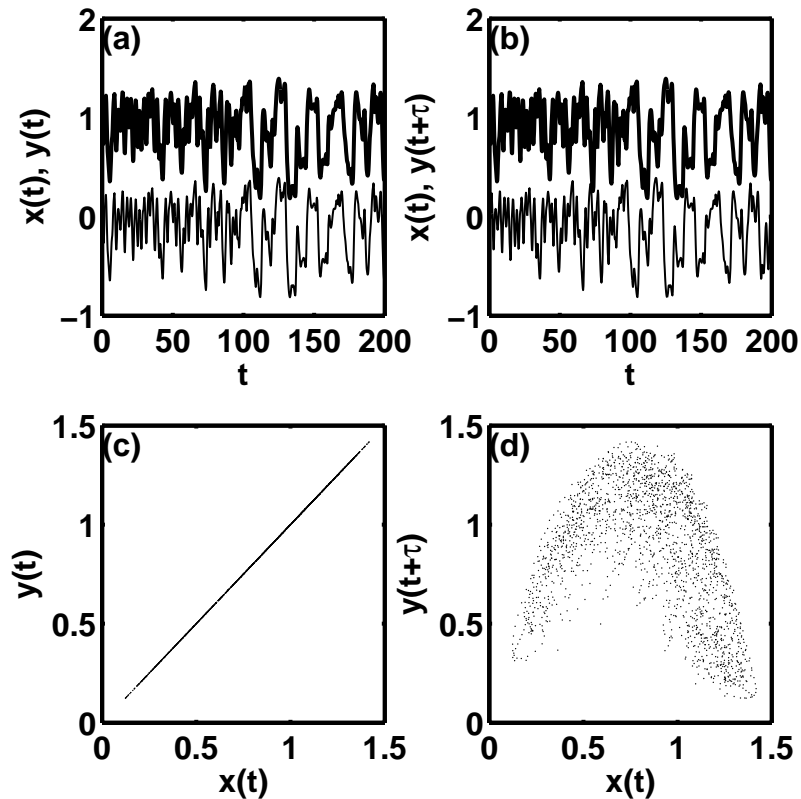
Figure 6.9: Comparison of the time series and the correlation plots for $\kappa = 1$ with $b = 1$, $a' = a = 2.0$, as in Fig. 6.5(a). (a) The time series of the driver signal, $x(t)$, (upper trace) and the receiver signal, $y(t)$, (lower trace). (b) The time series of the driver signal, $x(t)$, (upper trace) and the shifted receiver signal, $y(t + \tau)$, (lower trace). (c) The correlation plot between the two traces in (a). (d) The correlation plot between two traces in (b). $y(t + \tau)$ is driven by $x(t)$ in our configuration.
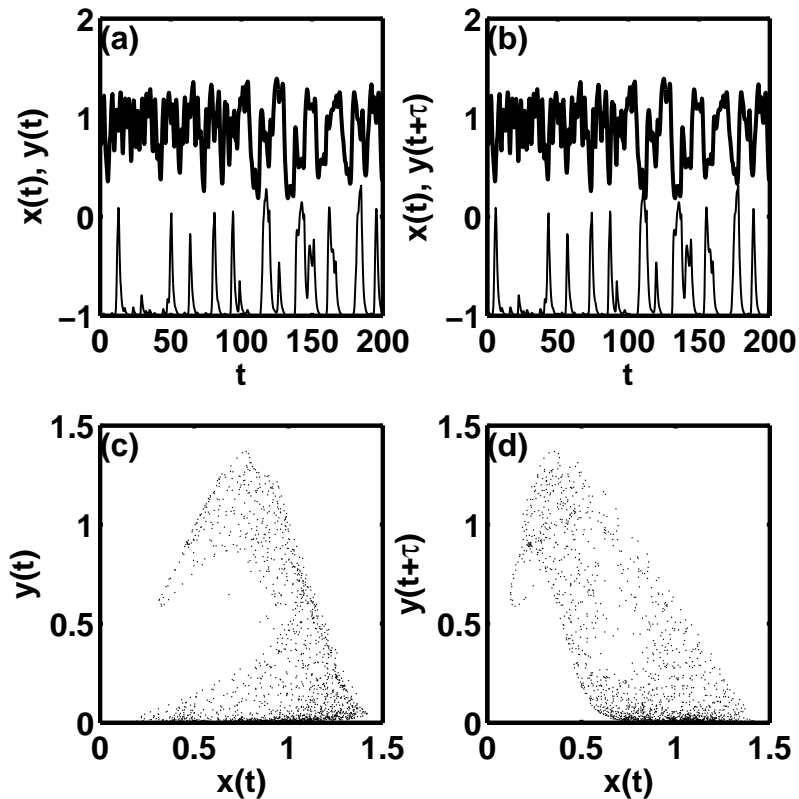
Figure 6.10: Comparison of the time series and the correlation plots for $\kappa = 2$ with $b = 1$, $a' = a = 2.0$, as in Fig. 6.5(a). (a) The time series of the driver signal, $x(t)$, (upper trace) and the receiver signal, $y(t)$, (lower trace). (b) The time series of the driver signal, $x(t)$, (upper trace) and the shifted receiver signal, $y(t + \tau)$, (lower trace). (c) The correlation plot between the two traces in (a). (d) The correlation plot between two traces in (b). $y(t + \tau)$ is driven by $x(t)$ in our configuration.
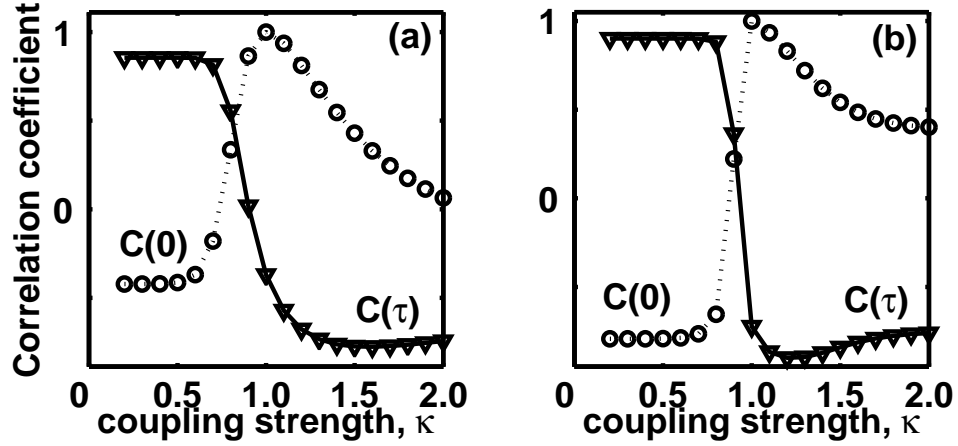
Figure 6.11: The cross-correlation coefficient $C(\Delta t = 0)$ associated with synchronization between the driver and the receiver (circles) and $C(\Delta t = \tau)$ associated with the direct modulation response of the receiver to the input signal (triangles). (a) $a' = a = 2.0$ and $b = 1$. (c) $a' = a = 1.44$ and $b = 1$.

In Fig. 6.11, we calculate the correlation coefficient $C(\Delta t = 0)$ associated with the synchronization of chaos between the driver and the receiver and $C(\Delta t = \tau)$ associated with the direct modulation response of the receiver to the input signal, varying the coupling strength κ. The correlation coefficient, $C(0)$, reaches its maximum at $\kappa = 1$, where the driver and the receiver are driven by the same signal and, therefore, are perfectly synchronized. As κ deviates from 1, the synchronization worsens. On the other hand, the correlation coefficient, $C(\tau)$, increases as the coupling gets weaker and reaches the saturation level corresponding to the positive linear modulation. The correlation coefficient, $C(\tau)$, decreases as the coupling gets stronger and reaches a minimum corresponding to the negative linear modulation. Further increasing the coupling strength, the nonlinearity of the transfer function

plays a role in the deterioration of the modulation quality. The synchronization regime is narrower at $a = 1.44$.

6.3 Synchronization with Bandwidth Limitation in Transmission

So far, we have assumed a transmission channel with infinite bandwidth. However, there exist bandwidth limitations and the channel noise in practical transmission lines. There have been few studies on the synchronization of chaotic systems with filtered signal and channel noise [47, 48, 49, 50]. In this section, we present the synchronization of two unidirectionally coupled Mackey-Glass circuits with bandwidth limitation in the transmission line [87].

6.3.1 A Low Pass Filter in the Transmission Channel

To investigate synchronization of chaos with bandwidth limitation in the transmission channel, we use two types of low pass filters, and use the cutoff frequency as a control parameter. Fig. 6.12 shows the block diagram of a simple RC filter and an active 2-pole Chebyshev filter [88]. With a simple RC filter shown in Fig. 6.12(a), the transfer function can be expressed as

$$H(s) = \frac{V_O}{V_{IN}} = \frac{1}{RCs + 1},\tag{6.14}$$

with $s = j\,2\pi f$ for a given frequency f. The cutoff frequency is defined as $f_c = (2\pi RC)^{-1}$ for which the magnitude of $H(s)$ is 3 dB less than that of the DC signal, i.e., $H(j\,2\pi f_c) = H(0) - 3$ in decibels.

An active Chebyshev filter as shown in Fig. 6.12(b) has a transfer function

$$H(s) = \frac{V_O}{V_{IN}} = \frac{A_V}{R^2C^2s^2 + RCs(3 - A_V) + 1},\tag{6.15}$$

where $A_V = 1 + R_2/R_1$ is the gain of the OP-Amp stage. The circuit parameters A_V and RC specify the characteristics of this Chebyshev filter. We choose the parameter

133
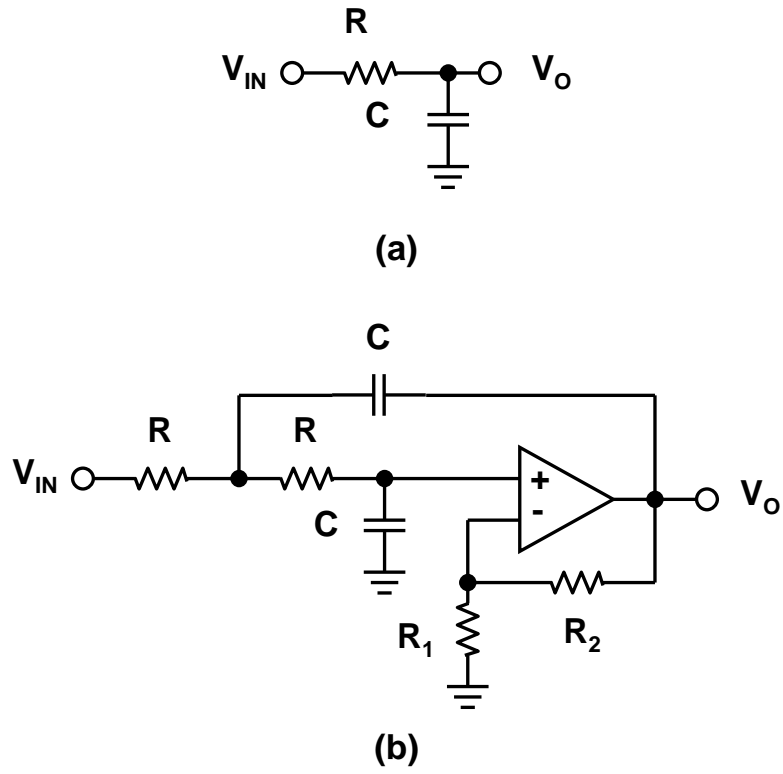
Figure 6.12: The block diagram of a low pass filter. (a) A simple RC filter and (b) an active 2-pole Chebyshev filter.

values such that the DC gain is equal to $0\ dB$ with the pass band ripple, $\gamma = 2\ dB$. The cutoff frequency in a Chebyshev filter is measured when the magnitude of the transfer function $H(j\ 2\pi f_c)$ becomes $3\ dB$ less than the maximum value H_{max}, i.e., $H(j\ 2\pi f_c) = H_{max} - 3$ in decibels. The relationship between the cutoff frequency and the product RC is

$$f_c = \frac{\alpha}{2\pi RC}, \tag{6.16}$$

where $\alpha = 1.1840$ for our setup. We can vary the cutoff frequency, f_c, by changing the value of RC for both types of low pass filters.

In the numerical simulations, we integrate the following equations

$$\frac{dx}{dt} = \frac{a\ x_\tau}{1 + x_\tau^{10}} - x, \tag{6.17}$$

$$\frac{dy}{dt} = \frac{a'\ y_{in}}{1 + y_{in}^{10}} - y, \tag{6.18}$$

with

$$y_{in}(t) = tx'(t) = \kappa\ \text{IFFT}[H(j\ 2\pi f) \times \text{FFT}[x(t - \tau)]], \tag{6.19}$$

where κ denotes the linear amplification factor in the transmission line or the coupling strength between the driver and the receiver circuits. In other words, the delayed driver signal $x(t - \tau)$ is Fourier transformed (FFT) and multiplied by the transfer function at each frequency component $H(j2\pi f)$ and then inverse Fourier transformed (IFFT) to obtain the transmitted signal $tx'(t)$. This transmitted signal is the input signal of the receiver circuit. In the following paragraph, $H(j2\pi f)$ will be defined such that $H(0) = 0$ in decibels. The linear amplification factor, or the coupling strength κ determines the total gain of the DC signal.
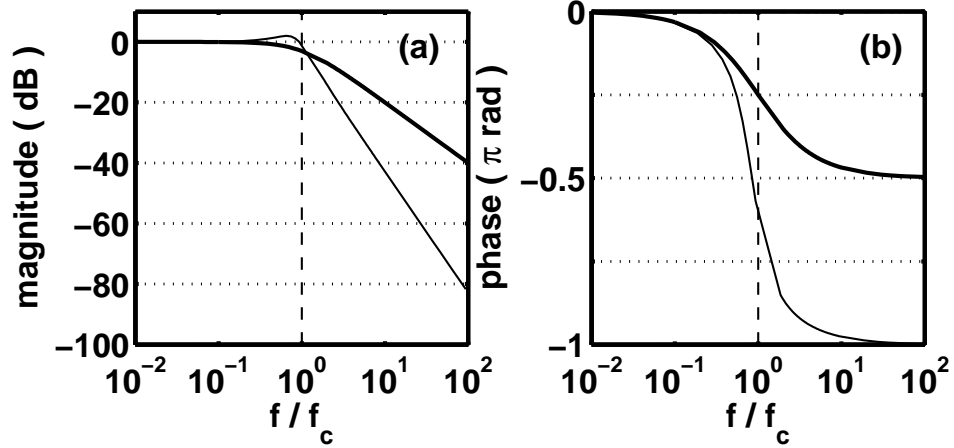
Figure 6.13: Numerically obtained low pass filter characteristics. (a) The normalized magnitude in dB versus the normalized frequency, f/f_c. (b) The phase characteristic as a function of the normalized frequency. The thick lines are results for the RC filter and thin lines for the 2-pole Chebyshev filter.

The transfer function for the RC filter is

$$H_{RC}(f) = \frac{1}{j\ (f/f_c) + 1}, \tag{6.20}$$

and that for the active 2-pole Chebyshev filter with 2 dB ripple is

$$H_{Cheby}(f) = \frac{1}{-c_1(f/f_c)^2 + j\ c_2(f/f_c) + 1}, \tag{6.21}$$

with $c_1 = 1.4018, c_2 = 1.0490$ for our case. The corresponding magnitude response and the phase response of each transfer function are shown in Fig. 6.13. The filtered magnitude decays more strongly with a Chebyshev filter as the frequency increases to larger than the cutoff frequency.

Before we present the experimental and numerical results for synchronization with a low pass filter in the transmission channel, we first show the results for

136
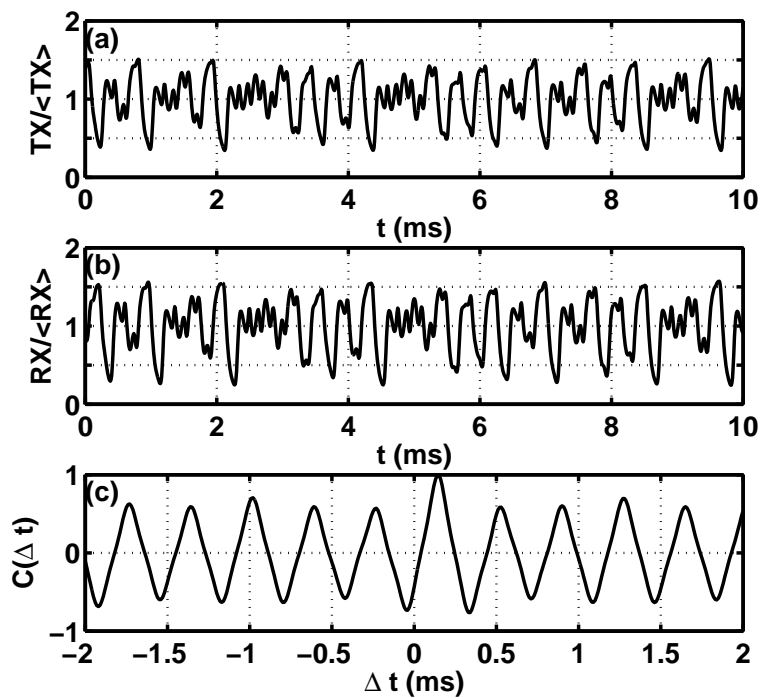
Figure 6.14: Synchronization of two unidirectionally coupled Mackey-Glass analog circuits without a filter in the transmission channel. (a) The time series of the driver output normalized to its mean $TX(t)/ < TX(t) >$. (b) The time series of the receiver output normalized to its mean $RX(t)/ < RX(t) >$. (c) The shifted cross correlation coefficient $C(\Delta t)$ versus the time shift Δt. T_{max} corresponds to the time shift at which $C(\Delta t)$ is maximum, $\sim 180 \ \mu s$ in our experimental setup [87].
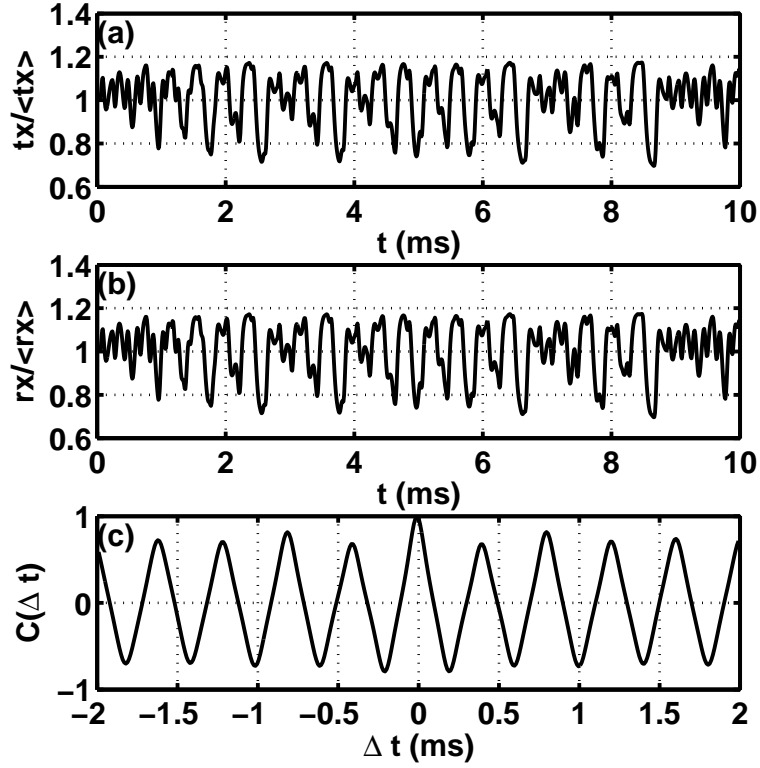
Figure 6.15: Numerical simulation plot corresponding to Fig. 6.14. The driver output $tx(t)$ is the delayed driver signal $x(t - \tau)$ and the receiver output $rx(t)$ is the delayed receiver signal $y(t - \tau)$, where $x(t)$ and $y(t)$ are numerically integrated from Eqn. 6.11 and Eqn. 6.12 with $a = a' = 1.44, b = 2, n' = n = 10, \tau = 7$ and $\kappa = 1$. The dimensionless time from the numerical simulation is converted to ms for the direct comparison with the experimental measurements.

138

synchronization with no filter in Fig. 6.14 and Fig. 6.15 as references. In Fig. 6.14, the time series of the receiver output exactly follows the time series of the driver output after 180 μs. The shifted cross-correlation coefficient $C(\Delta t)$ is maximum at $\Delta t = T_{\max} \sim 180 \ \mu s$ and its value is 1. On the other hand, the numerical simulations show that the receiver output follows the driver output with no time shift when there is no linear amplification/attenuation in transmission. In Fig. 6.7, we showed that the receiver signal follows the driver signal after a propagation delay time, T_d, when the transmitted signal is attenuated along the transmission. Therefore, we conclude that the driver output is attenuated in the transmission channel for our experimental setup.

6.3.2   Experimental Observations

In this section, we present the dependence of the synchronization on the cutoff frequency of the low pass filter in the transmission channel. We use a 2-channel oscilloscope (GageScope CS1450) to record the driver output $TX(t)$ and the receiver output $RX(t)$ at 10^5 samples per second. 4602 sample points are recorded for each time window and 5 time series are taken for each cutoff frequency.

In Fig. 6.16 and Fig. 6.17, the driver output normalized to its mean $TX/ < TX >$ and the receiver output normalized to its mean $RX/ < RX >$ are shown and the shifted cross correlation coefficient $C(\Delta t)$ is plotted as a function of the time shift, Δt. Fig. 6.16 is obtained with the RC filter for $f_c = 125 \ Hz$ (left column) and $12,100 \ Hz$ (right column), and Fig. 6.17 is obtained with the active 2-pole Chebyshev filter for $f_c = 646 \ Hz$ (left column) and $15,052 \ Hz$ (right column). For a small
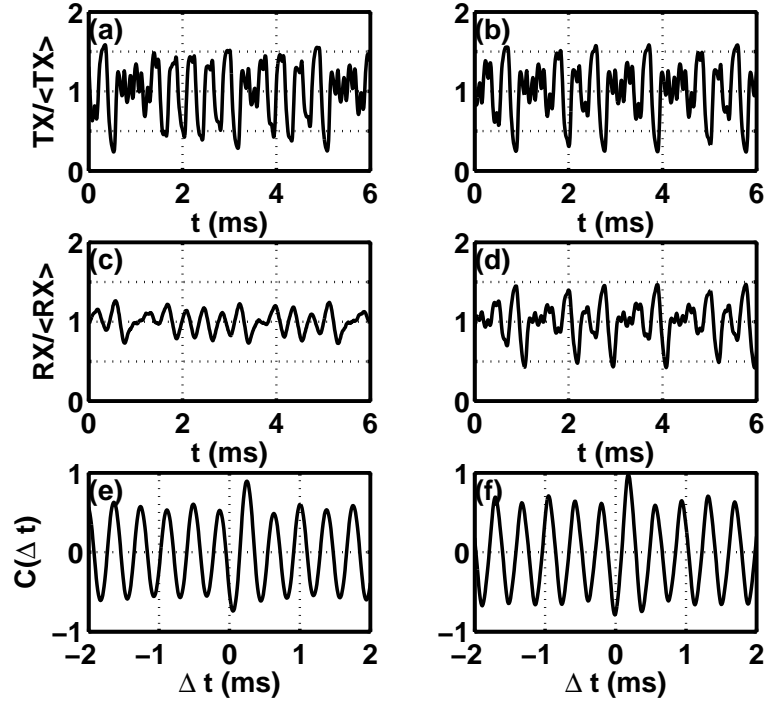
Figure 6.16: Experimental time series of the synchronization with an RC filter in the transmission channel. The time series of the driver output normalized to its mean (top); the time series of the receiver output normalized to its mean (middle); the shifted cross-correlation versus the time shift (bottom). (a), (c), and (e) are obtained for the cutoff frequency $f_c = 125\ Hz$, and (b), (d), and (f) for $f_c = 12,100\ Hz$. The dominant peak of the chaotic signal generated by the driver circuit is located at $f_1 = 2.7\ kHz$ as discussed in Section 5.4 [87].
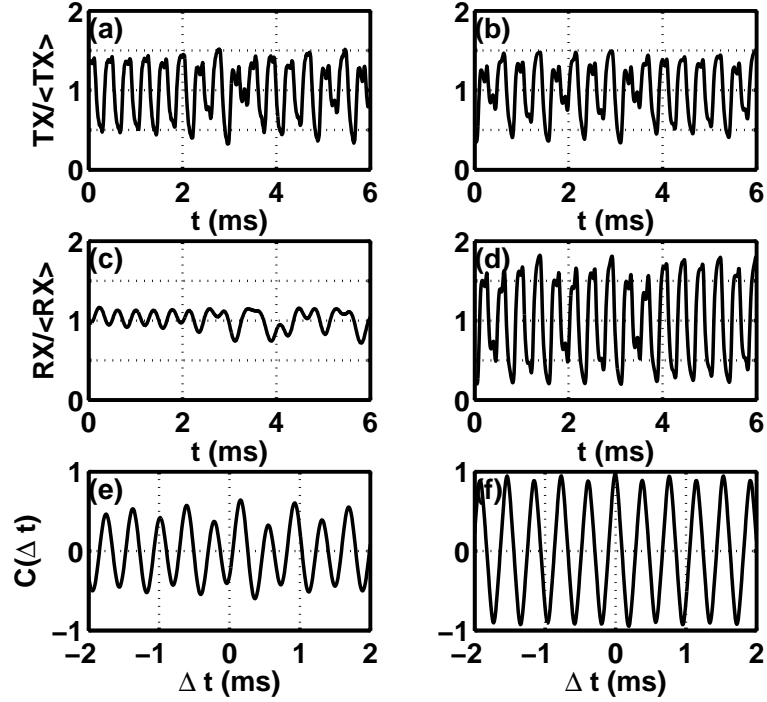
Figure 6.17: Experimental time series of the synchronization with a active 2-pole Chebyshev filter in the transmission channel. The time series of the driver output normalized to its mean (top); the time series of the receiver output normalized to its mean (middle); the shifted cross-correlation versus the time shift (bottom). (a), (c), and (e) are obtained for the cutoff frequency $f_c = 2646\ Hz$, and (b), (d), and (f) for $f_c = 15,052\ Hz$. The dominant peak of the chaotic signal generated by the driver circuit is located at $f_1 = 2.7\ kHz$ as discussed in Section 5.4.

cutoff frequency, the fast oscillations are filtered and the receiver output becomes smooth, whereas, for a large cutoff frequency, the receiver output synchronizes to the driver output more accurately in both types of filters.

In Fig. 6.18, the color map of the shifted cross-correlation coefficient

$$
\begin{aligned}
C(\Delta t) &= C_{TX,RX}(\Delta t), \\
&= \frac{<(TX(t)- <TX(t)>)(RX(t+\Delta t)- <RX(t)>)>}{\sqrt{<(TX(t)- <TX(t)>)^2>}\sqrt{<(RX(t)- <RX(t)>)^2>}}, \quad (6.22)
\end{aligned}
$$

is calculated for a varying cutoff frequency of the RC filter in (a) and that of active 2-pole Chebyshev filters in (b). In Fig. 6.18(a) with the RC filter, the time at maximum correlation T_{max} increases from 180 μs to 290 μs as the cutoff frequency f_c decreases (downward in vertical direction). Fig. 6.18(b) shows the results with the active Chebyshev filter, T_{max} increases from 0 μs to 180 μs as f_c decreases.

Fig. 6.19 shows the maximum cross-correlation $C(T_{max})$ and the corresponding time shift T_{max} as a function of f_c for the RC filter (circles) and for the Chebyshev filter (squares). The error bars are given by the standard deviation of the average $C(T_{max})$ and T_{max} calculated from 5 time windows for a given f_c. The vertical lines are located at the dominant peak in the power spectrum of the chaotic signal, i.e., $f_1 = 2.7\ kHz$ for our experimental setup. The correlation is reduced dramatically for $f_c < f_1$ and is saturated for $f_c > f_1$. In other words, the inclusion of the frequency components up to the dominant frequency is very important to achieve synchronization of the receiver output with the driver output. Once this condition is satisfied, i.e., if $f_c > f_1$, the higher frequency components with $f > f_1$ do not significantly affect the quality of synchronization.
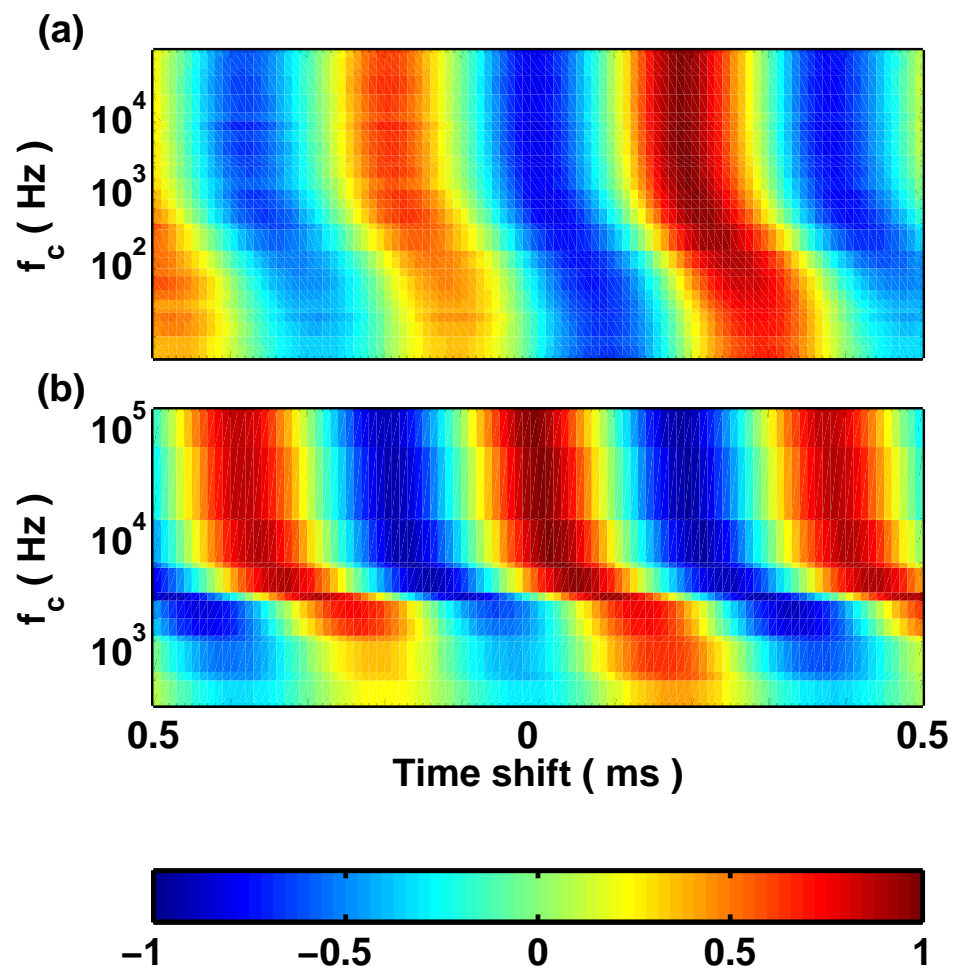
Figure 6.18: The color map of the shifted cross-correlation coefficient $C(\Delta t)$ calculated from the driver output $TX(t)$ and the receiver output $RX(t)$, while varying the cutoff frequency f_c. (a) is obtained with an RC filter in the transmission channel, and (b) with a 2-pole Chebyshev filter. The horizontal axis represents the time shift, Δt, measured in ms and the vertical axis represents the cutoff frequency, f_c, measured in Hz [87].

Figure 6.19: (a) The maximum cross-correlation coefficient $C(\Delta t = T_{max})$ versus $\log_{10}(f_c)$ and (b) the corresponding time shift at maximum correlation T_{max}. Circles are obtained with RC filters and squares with 2-pole Chebyshev filters. The vertical line is located at $f_1 = 2.7 \ kHz$ [87].

To better understand the experimental observations, we explore the numerical simulations in the following section.

6.3.3   Measurements in the Experiments and in the Numerical Simulations

Before we present results from numerical simulations, we clarify what we measure in experiments and in numerical simulations. In Fig. 6.20, we show the block diagram of unidirectionally coupled Mackey-Glass circuits in an open-loop receiver configuration. In the experiments, we record voltage signals at points 2 and 5, the driver output, $TX(t)$, and the receiver output, $RX(t)$, respectively. The time-shifted cross-correlation coefficient between these two signals

$$C(\Delta t) = C_{TX,RX}(\Delta t),$$
$$= \frac{< (TX(t)- < TX(t) >)(RX(t + \Delta t)- < RX(t) >) >}{\sqrt{< (TX(t)- < TX(t) >)^2 >}\sqrt{< (RX(t)- < RX(t) >)^2 >}}, \quad (6.23)$$

is associated with the synchronization between the driver and receiver circuits.

In the numerical simulations, the dynamics of voltage signals at points 1 and 4, the driver signal $x(t)$ and the receiver signal $y(t)$, are described by the coupled Mackey-Glass equations shown in Eqns. 6.17- 6.18. The voltage signal at point 3, which is the input signal to the receiver $y_{in}(t)$, is also calculated by low pass filtering the delayed driver signal, $x(t - \tau)$. To characterize the synchronization between the driver and receiver signals, we calculate the time-shifted cross-correlation coefficient between $x(t)$ and $y(t)$

$$C_1(\Delta t) \quad = \quad C_{x,y}(\Delta t),$$
$$= \quad \frac{< (x(t)- < x(t) >)(y(t + \Delta t)- < y(t) >) >}{\sqrt{< (x(t)- < x(t) >)^2 >}\sqrt{< (y(t)- < y(t) >)^2 >}}, \quad (6.24)$$
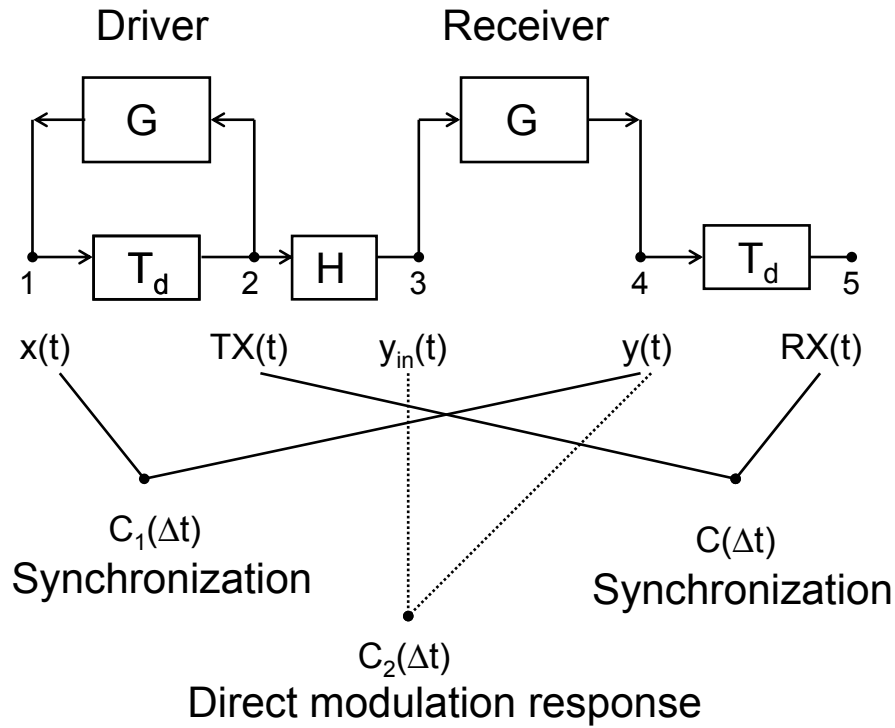
Figure 6.20: The block diagram of two unidirectionally coupled Mackey-Glass circuits in an open-loop receiver configuration. G is the nonlinear block for Mackey-Glass dynamics (a nonlinear device with a low pass filter) and T_d corresponds to the delay line. H corresponds to the transmission line. $TX(t)$ is the driver output, $RX(t)$ is the receiver output, and we record these two variables in the experiments. $x(t)$ is the driver signal, $y(t)$ is the receiver signal, $y_{in}(t)$ is the input signal to the receiver, and we calculate these three variables in the numerical simulations. The shifted cross correlation $C(\Delta t)$ measures the synchronization between $TX(t)$ and $RX(t)$, $C_1(\Delta t)$ measures the synchronization between $x(t)$ and $y(t)$, and $C_2(\Delta t)$ measures the direct modulation response of $y(t)$ to $y_{in}(t)$.

which is same as $C(\Delta t)$.

In addition to $C_1(\Delta t)$, we calculate the time-shifted cross-correlation coefficient between $y_{in}(t)$ and $y(t)$

$$
\begin{aligned}
C_2(\Delta t) &= C_{y_{in},y}(\Delta t), \\
&= \frac{< (y_{in}(t)- < y_{in}(t) >)(y(t+\Delta t)- < y(t) >) >}{\sqrt{< (y_{in}(t)- < y_{in}(t) >)^2 >}\sqrt{< (y(t)- < y(t) >)^2 >}}, \quad (6.25)
\end{aligned}
$$

and $C_2(\Delta t)$ is associated with the direct modulation response of the receiver to the input signal. The component G in Fig. 6.20 shows a nonlinear transfer characteristic and the response to the input signal is determined by the transfer function of G. Therefore, by calculating $C_2(\Delta t)$, we can estimate the modulation response of $y(t)$ for a given input signal $y_{in}(t)$.

In the following section, we calculate $C(\Delta t)$, $C_1(\Delta t)$, and $C_2(\Delta t)$ to study the response of the receiver circuit.

6.3.4 Numerical Simulations

Fig. 6.21 shows the time series of the driver signal $x(t)$, the input signal to the receiver $y_{in}(t)$, and the receiver signal $y(t)$ obtained by integrating Eqns. 6.17, 6.18 and 6.19, with an RC filter in the transmission line described by Eqn. 6.20 for $f_c = 0.32 \times f_1 < f_1$ in (a) and for $f_c = 32 \times f_1 > f_1$ in (b). We consider the case of $\kappa = 1$ with $a' = a = 1.44$, and $\tau = 7$.

In Fig. 6.21(a) and (b), the input signal of the receiver $y_{in}(t)$ follows the driver signal with the time delay τ, as indicated by arrows, while the fast oscillations are removed at a smaller value of f_c in (a) due to the low pass filtering effect. For
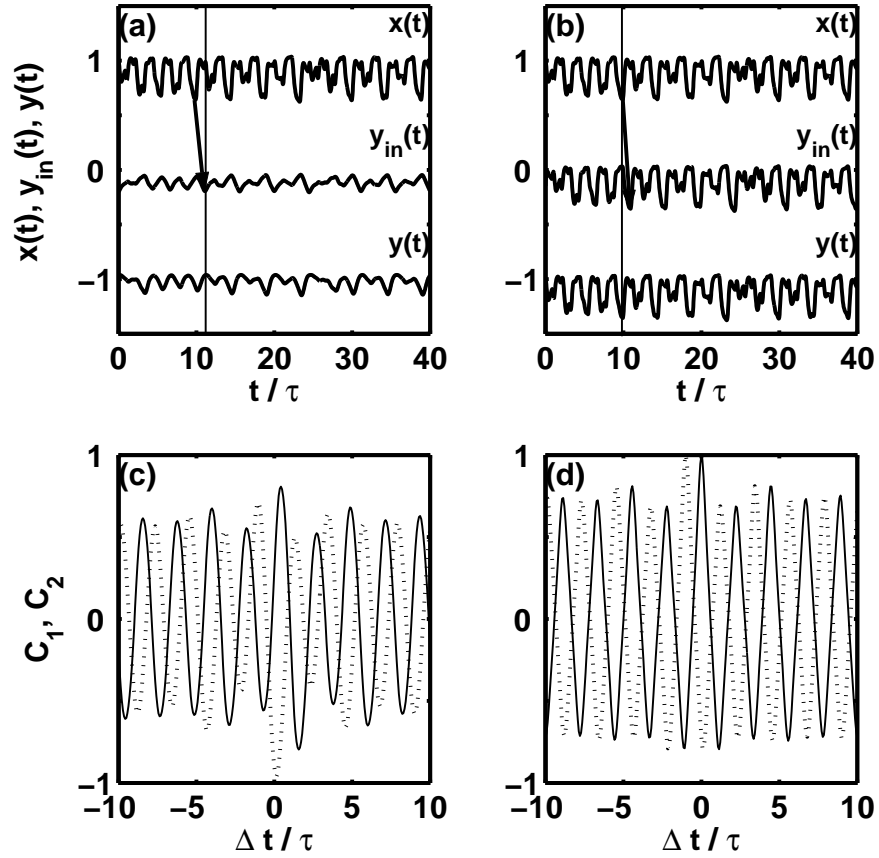
Figure 6.21: Numerical comparison of the time series and the shifted cross-correlation coefficients with an RC filter in the transmission channel. (a) and (b): The time series of the driver signal $x(t)$ (top trace), the input signal to the receiver $y_{in}(t)$ (middle trace), and the receiver signal $y(t)$ (bottom trace). (c) and (d): The shifted cross-correlation coefficient calculated between the driver signal and the receiver signal, $C_1(\Delta t) = C_{x,y}(\Delta t)$ (solid line), and the shifted cross-correlation coefficient calculated between the input signal and the receiver signal, $C_2(\Delta t) = C_{y_{in},y}(\Delta t)$ (dotted line). (a) and (c) are obtained for $f_c/f_1 = 0.32$ and (b) and (d) for $f_c/f_1 = 32$. The time and the the time shift are measured in units of the time delay τ ($a' = a = 1.44$, $\tau = 7$, and $\kappa = 1$).

$f_c = 0.32 \ f_1$ in Fig. 6.21(a), the receiver signal follows the input signal almost linearly with anti-phase relationship, whereas for $f_c = 32 \ f_1$ in Fig. 6.21(b), the receiver signal is synchronized to the driver signal, therefore anticipating the input signal.

In Fig. 6.21(c) and (d), we calculate the shifted cross-correlation coefficient associated with synchronization between the driver and the receiver (solid lines), $C_1(\Delta t) = C_{x,y}(\Delta t)$, and the shifted cross-correlation coefficient associated with the direct modulation response of the receiver to the input signal (dotted lines), $C_2(\Delta t) = C_{y_{in},y}(\Delta t)$.

For $f_c = 0.32 \ f_1$ in Fig. 6.21(c), $C_2(\Delta t)$ reaches its minimum at $\Delta t = 0$ and its magnitude is greater than the maximum value of $C_1(\Delta t)$. Therefore, the receiver signal is the directly modulated by the input signal with an anti-phase relationship. On the other hand, in Fig. 6.21(d) with $f_c = 32 \ f_1$, $C_1(\Delta t)$ is at the maximum with $\Delta t = 0$, indicating very good synchronization between the driver and the receiver. $C_2(\Delta t = -\tau) = 1$ simply indicates that the input signal to the receiver is the delayed driver signal without distortion. Therefore, the driver and receiver are driven by the same input signals resulting in almost perfect synchronization.

We calculate the maximum value of the cross-correlation coefficient $C(T_{max})$ between the driver output $tx(t) = x(t - \tau)$ and the receiver output $rx(t) = y(t - \tau)$ and the corresponding time shift T_{max} as a function of the cutoff frequency, f_c, in Fig. 6.22. The vertical lines are located at the fundamental frequency f_1 obtained from numerical simulations. As shown experimentally in Fig. 6.19, the maximum correlation time T_{max} increases as f_c decreases below f_1, approaching $T_{max} = T_d$
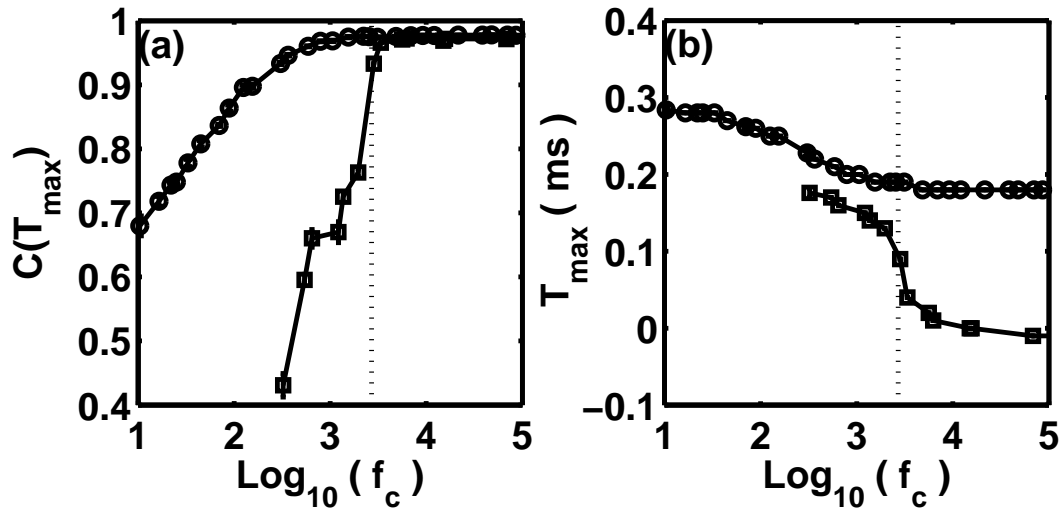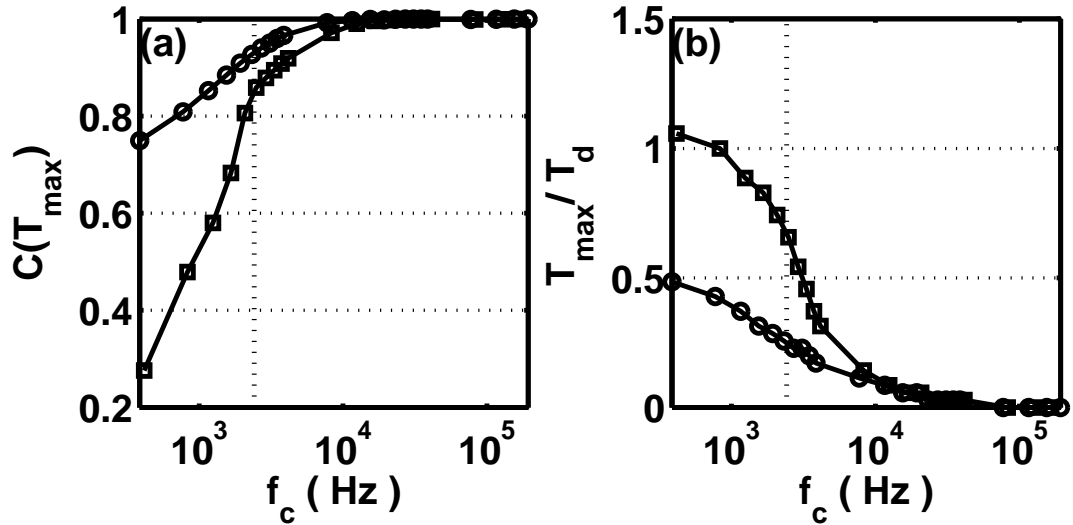
Figure 6.22: Numerical simulation plots corresponding to Fig. 6.19. (a) The maximum cross-correlation coefficient $C(\Delta t = T_{max})$ versus $\log_{10}(f_c)$ and (b) the corresponding time shift at maximum correlation normalized to the delay time T_{max}/T_d. Circles are obtained with an RC filter and squares with a 2-pole Chebyshev filter. The vertical line in each plot is located at the fundamental frequency f_1, corresponding to the dominant peak of the power spectra ($a' = a = 1.44$, $\tau = 7$, and $\kappa = 1$) [87].

with the Chebyshev filter and $T_d/2$ with an RC filter. The corresponding maximum correlation coefficient reduces as f_c decreases below f_1, which is more dramatic with Chebyshev filters. $C(T_{max}) = 1$ and $T_{max} = 0$ when f_c is much greater than f_1.

To see whether the receiver is synchronized to the driver or is just directly modulated by the input signal, we calculate two cross-correlation coefficients ρ_1 and ρ_2 in Fig. 6.23. The coefficient ρ_1

$$\rho_1 = C_1(\Delta t = 0) = C_{x,y}(\Delta t = 0), \tag{6.26}$$

is associated with synchronization between the driver and receiver without the time shift, and the coefficient ρ_2

$$\rho_2 = C_2(\Delta t = 0) = C_{y_{in},y}(\Delta t = 0), \tag{6.27}$$

is associated with the direct modulation response of the receiver to the input signal without the time shift. The vertical lines are located at $f = f_1 = 1/T_1$ and $f = 1/T_d$, where $T_1 \approx 2T_d$. For $f_c < f_1$, the magnitude of ρ_2 is greater than that of ρ_1, whereas for $f_c > 1/T_d$, ρ_1 has greater magnitude than ρ_2. This implies that the receiver is synchronized to the driver when $f_c > 1/T_d$ and is directly modulated by the input signal when $f_c < f_1$. The quality of synchronization with Chebyshev filters shows a significant transition near $f_c = f_1$.

So far, we have assumed that the total gain of DC signal is zero in decibels, i.e., $\kappa = 1$ in Eqn. 6.19. As mentioned earlier for the experiments, the maximum correlation time T_{max} was measured to be T_d without a filter in Fig. 6.14, and T_{max} approached T_d for $f_c > f_1$ with an RC filter in Fig. 6.19(b). In Fig. 6.7 without any filter, we observed that T_{max} is equal to T_d and there is attenuation in the
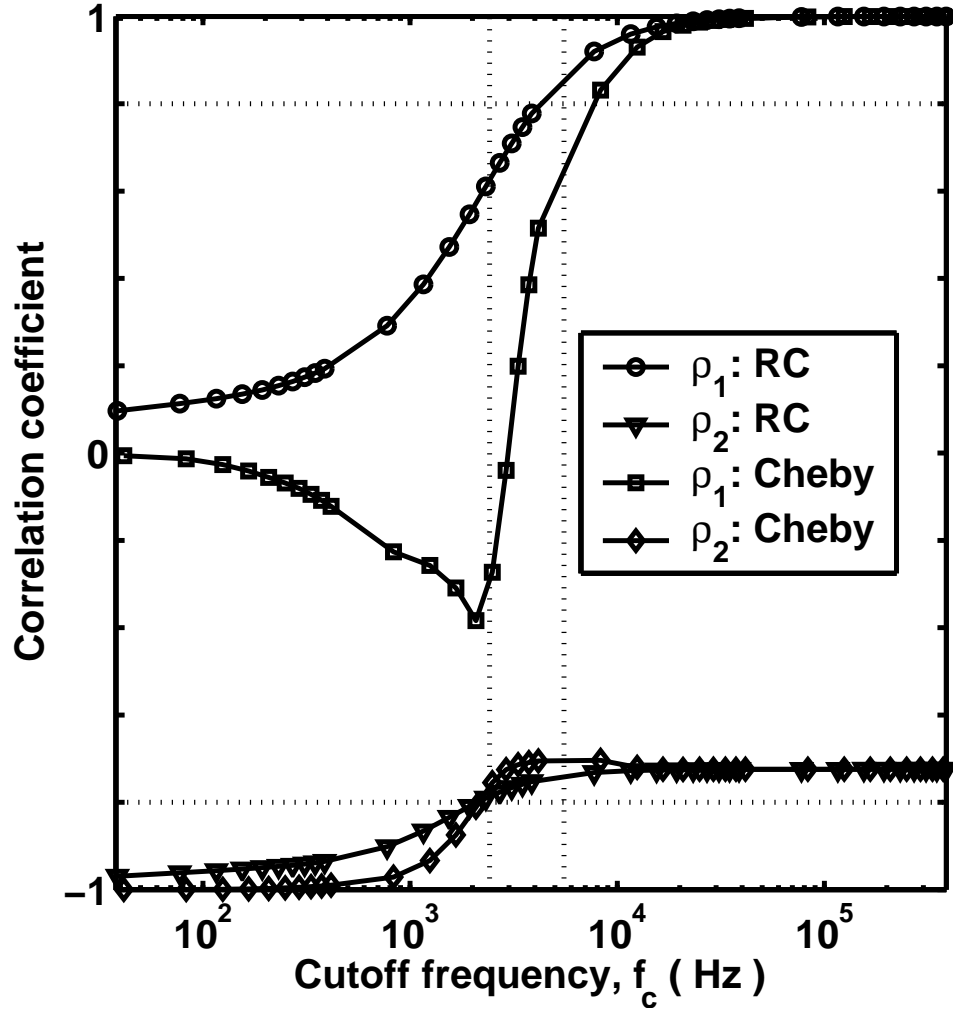
Figure 6.23: The cross-correlation coefficient $\rho_1 = C_1(\Delta t = 0) = C_1(x(t), y(t))$ associated with synchronization between the driver and the receiver (circles for the RC filter and squares for the 2-pole Chebyshev filter), and $\rho_2 = C_2(\Delta t = 0) = C_2(xt'(t), y(t))$ associated with the direct modulation response of the receiver to the transmitted signal (triangles for the RC filter and diamonds for the 2-pole Chebyshev filter). The left vertical line is located at $f_1 = 1/T_1$ and the right vertical line is located at $1/T_d$ ($a' = a = 1.44$, $\tau = 7$).
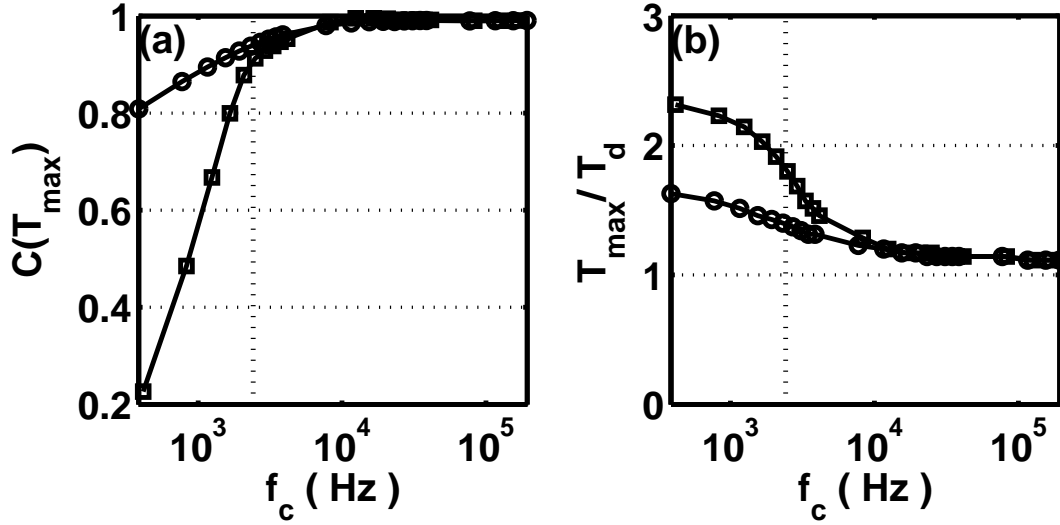
Figure 6.24: Same plot as in Fig. 6.22 except $\kappa = 0.5$ in Eqn. 6.19. (a) The maximum cross-correlation coefficient $C(\Delta t = T_{max})$ versus $\log_{10}(f_c)$ and (b) the corresponding time shift at maximum correlation normalized to the delay time T_{max}/T_d. Circles are obtained with an RC filter and squares with a 2-pole Chebyshev filter. The vertical line in each plot is located at the fundamental frequency f_1, corresponding to the dominant peak of the power spectra ($a' = a = 1.44$, $\tau = 7$) [87].

transmission line, $\kappa < 1$. Therefore, we add linear attenuation with $\kappa = 0.5$ in addition to the low pass filtering in transmission.

Fig. 6.24 and Fig. 6.25 are similar to Fig. 6.22 and Fig. 6.23, respectively, except that κ is fixed at 0.5 in Eqn. 6.19. The maximum correlation time in Fig. 6.24(b) approaches T_d as f_c becomes greater than f_1. In Fig. 6.25, the magnitude of ρ_2 is always greater than that of ρ_1 and this implies that the receiver signal is direct modulation response to the input signal.

In our experiments with a low pass filter in the transmission channel, the DC
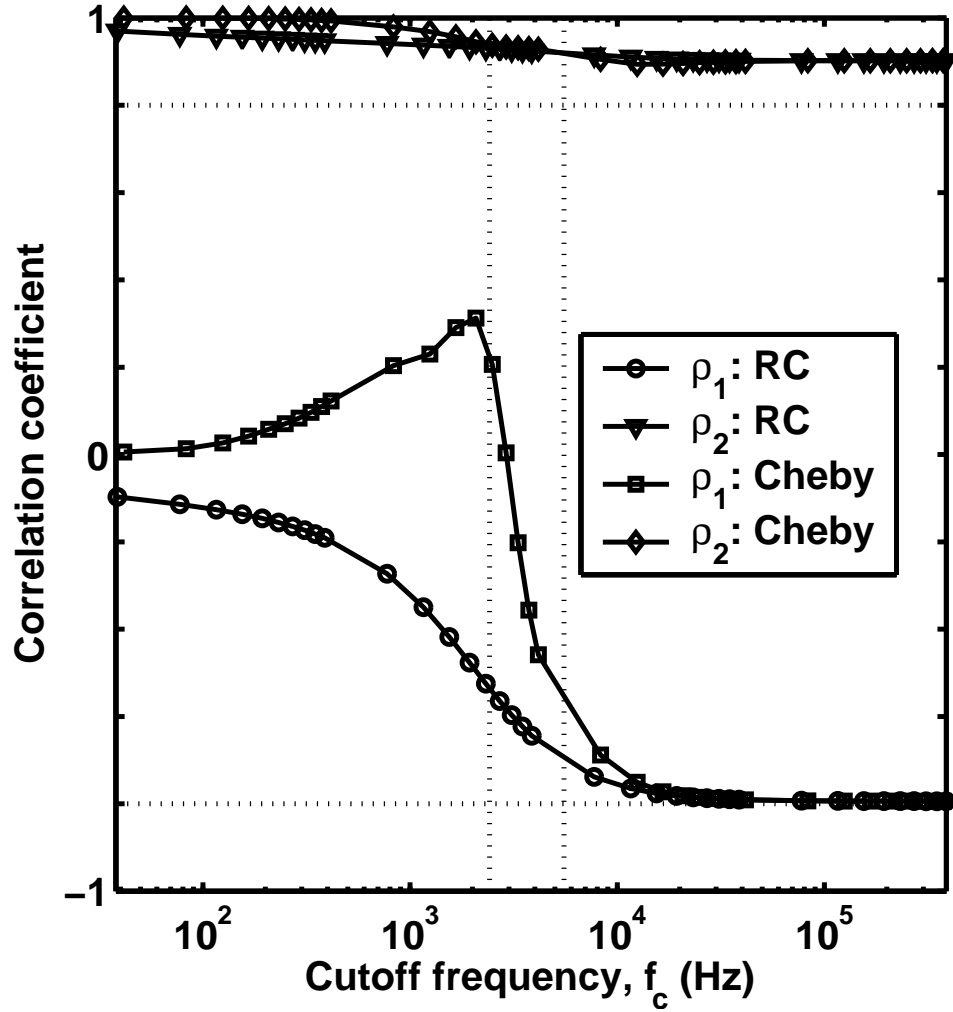
Figure 6.25: Same plot as in Fig. 6.23 except $\kappa = 0.5$ in Eqn. 6.19. The cross-correlation coefficient $\rho_1 = C_1(\Delta t = 0) = C_1(x(t), y(t))$ associated with synchronization between the driver and the receiver (circles for the RC filter and squares for the 2-pole Chebyshev filter), and $\rho_2 = C_2(\Delta t = 0) = C_2(xt'(t), y(t))$ associated with the direct modulation response of the receiver to the transmitted signal (triangles for the RC filter and diamonds for the 2-pole Chebyshev filter). The left vertical line is located at $f_1 = 1/T_1$ and the right vertical line is located at $1/T_d$ $(a' = a = 1.44, \ \tau = 7)$.

gain of the Chebyshev filter was adjusted so that it was zero in decibels, whereas the total gain of DC signal with an RC filter remained the same as that without the filter. Therefore, $C(T_{max})$ and T_{max} plotted in Fig. 6.19 are consistent with numerical data when we assume linear attenuation for the RC filter but no attenuation for the Chebyshev filter. When an RC filter is used with linear attenuation in the transmission line, the receiver signal is the direct modulation response to the input signal. When a Chebyshev filter is used without linear attenuation/amplification in the transmission line, the receiver signal is synchronized to the driver signal.

6.3.5   Phase Distortion in a Low Pass Filter

In Fig. 6.7, we have considered the dependence of the maximum correlation time T_{max} on the coupling strength κ. For $\kappa = 0.5$, T_{max} is almost equal to T_d without low pass filtering in the transmission channel, whereas for $\kappa = 1$, T_{max} is equal to zero. Therefore, the values of T_{max} at $f_c \gg f_1$ in Figs. 6.22 and 6.24 can be explained in terms of the coupling strength. The dependence of T_{max} on the cutoff frequency, however, is not explained by the coupling strength. To understand how T_{max} changes in relation to the cutoff frequency of the low pass filter, we are going to pay attention to the phase distortion introduced by the low pass filter in the transmission channel.

Fig. 6.13(b) shows the phase response of a low pass filter as a function of the frequency normalized to the cutoff frequency. For $f \gg f_c$, a phase shift of $-\pi/2$ is induced by an RC filter and a phase shift of $-\pi$ is induced by a Chebyshev filter. Since the maximum correlation time changes by the amount of $T_d/2$ for an RC filter
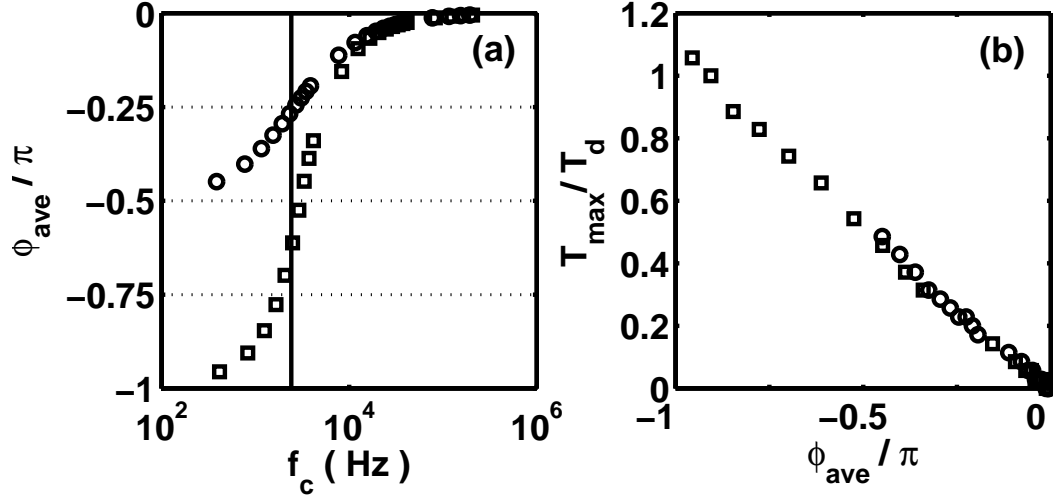
Figure 6.26: The average phase change induced by a low pass filter. (a) The average phase change ϕ_{ave}, versus the cutoff frequency f_c and (b) the maximum correlation time T_{max} for $\kappa = 1$, versus the average phase change ϕ_{ave} at each cutoff frequency. The circles are obtained with an RC filter and squares with a Chebyshev filter. The vertical line in (a) is located at the fundamental frequency f_1, corresponding to the dominant peak of the power spectra ($a' = a = 1.44$, $\tau = 7$).

and by the amount of T_d for an Chebyshev filter, we investigate the relation between T_{max} and the average phase change induced by a low pass filter, ϕ_{ave}, defined as

$$\phi_{ave}(f_c) = \frac{\int_{0^+}^{\infty} \phi[H_{f_c}(j2\pi f)] \times P_x(f)df}{\int_{0^+}^{\infty} P_x(f)df}, \tag{6.28}$$

where the phase angle of the transfer function at a given cutoff frequency, $\phi[H_{f_c}(j2\pi f)]$, is multiplied by the power spectral density of the driver output, $P_x(f)$, and integrated over the positive frequency range.

Fig. 6.26(a) shows the average phase change as a function of the cutoff frequency at a given driver signal. As f_c decreases from 1 MHz to 0.1 kHz, ϕ_{ave} changes

156
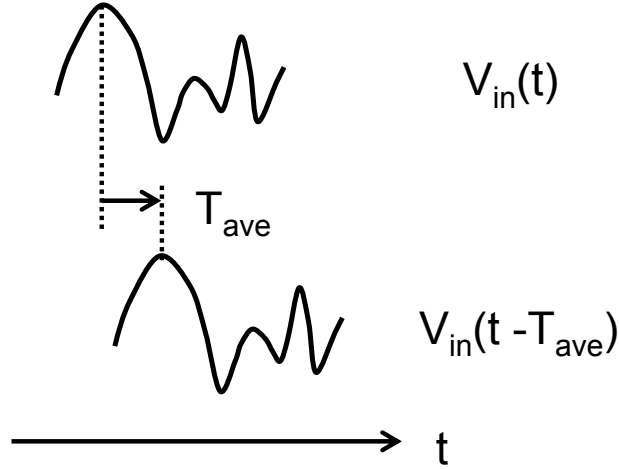
Figure 6.27: The effect of an average time shift on a signal.

from zero to $-\pi/2$ with an RC filter, from zero to $-\pi$ with an Chebyshev filter. Assuming that the maximum correlation time T_{max} may be related with the average phase change induced by a low pass filter, we plot T_{max} versus ϕ_{ave} at each cutoff frequency in Fig. 6.26(b) and find the following relation,

$$\frac{T_{max}}{T_d} \approx -\frac{\phi_{ave}}{\pi}. \tag{6.29}$$

In order to understand this observation, we can provide a intuitive explanation. Most of the AC signal generated by the driver Mackey-Glass circuit is carried by the dominant frequency component, $f_1 \sim 1/(2T_d)$, and the original signal before a low pass filter can be approximated by

$$V_{in}(t) \approx V_1 \exp^{i2\pi f_1 t}, \tag{6.30}$$

where V_1 is the amplitude of the signal at f_1. Since a low pass filter induces an

average phase change, the filtered signal can be written as

$$
\begin{aligned}
V_{out}(t) &\approx V_1 \exp^{i2\pi f_1 t + i\phi_{ave}} \\
&= V_1 \exp^{i2\pi f_1(t + \phi_{ave}/2\pi f_1)} .
\end{aligned}
\tag{6.31}
$$

If the original signal is shifted forward in time by the amount of T_{ave} as illustrated in Fig. 6.27, we have

$$
\begin{aligned}
V_{out}(t) &= V_{in}(t - T_{ave}) \\
&\approx V_1 \exp^{i2\pi f_1(t - T_{ave})} .
\end{aligned}
\tag{6.32}
$$

By equating Eqn. 6.31 with Eqn. 6.32, we obtain

$$
T_{ave} = -\frac{\phi_{ave}}{2\pi f_1} .
\tag{6.33}
$$

The maximum cross-correlation between the original signal and the filtered signal, $< V_{in}(t) V_{out}(t + \Delta t) >$, occurs at $\Delta t = T_{ave}$ in this case. In other words, the time shift at the maximum correlation is given by

$$
T_{max} = T_{ave} = -\frac{\phi_{ave}}{2\pi f_1} \approx -\frac{\phi_{ave} \times 2T_d}{2\pi} = -\frac{\phi_{ave} T_d}{\pi} ,
\tag{6.34}
$$

which is the same result as Eqn. 6.29.

The average phase change induced by a low pass filter in the transmission channel, therefore, explains the dependence of the time shift at the maximum correlation between the driver and receiver signal on the cutoff frequency. When the cutoff frequency of a low pass filter becomes smaller than the dominant frequency of the original signal, the dominant frequency component experiences a phase shift in addition to the attenuation of the power during the transmission. Since most of

the power in the original signal is carried by the dominant frequency component, the time series of the filtered signal is separated from that of the original signal by a time shift corresponding to the phase shift at the dominant frequency.

In summary, the time shift at maximum correlation is strongly dependent both on the phase response of the dominant frequency component to a low pass filter in the transmission channel and on the coupling strength.
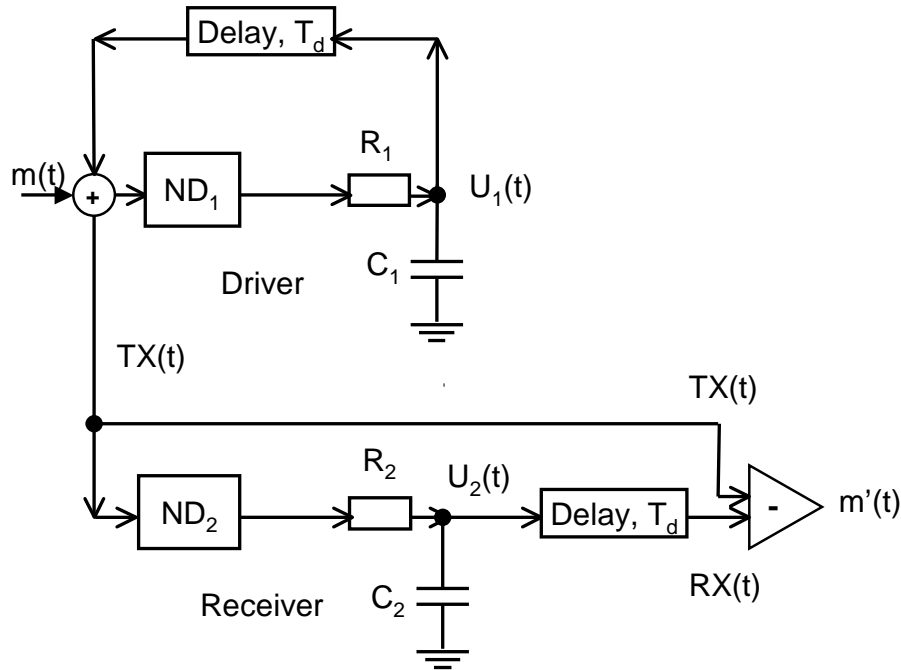
Figure 6.28: The schematic diagram for a synchronized chaotic system using unidirectionally coupled Mackey-Glass analog circuits with an open loop configuration for the receiver. All symbols are same as in Fig. 6.3 except we assume $TX'(t) = TX(t)$. $m(t)$ is the original message and $m'(t)$ is the recovered message.

6.4   Applications to Communication

Synchronization of chaos can be applied to the field of communication by transmitting messages encoded on a chaotic waveform and decoding the original messages using the synchronization [39, 40, 42, 44, 45, 46]. In this section, we present one of the schemes to implement a chaotic communication system using unidirectionally coupled Mackey-Glass analog circuits with an open loop configuration for the receiver.

As shown in Fig. 6.28, the original message signal $m(t)$ is added between the

delay line and the nonlinear device in the driver circuit. Assuming no distortion in the transmission line, the input to ND_1 is equal to the input to ND_2 with $TX(t) = m(t) + U_1(t - T_d)$. When the receiver is synchronized to the driver, we have $U_1(t) = U_2(t)$ and $RX(t) = U_2(t - T_d)$. By subtracting the receiver output from the transmitted signal, we obtain $m'(t)$

$$m'(t) = TX(t) - RX(t) = m(t) + U_1(t - T_d) - U_2(t - T_d), \qquad (6.35)$$

where the recovered signal $m'(t)$ is equivalent to the original message $m(t)$ when two circuits are synchronized $U_2(t) = U_1(t)$.

Fig. 6.29 shows the synchronization between the driver and receiver with a 500 Hz sinusoidal message. By subtracting the transmitted signal $TX(t)$ from the receiver output $RX(t)$, we obtain the recovered message $m'(t)$. To remove fast noise signal from the recovered message, a low pass filter with high enough cutoff frequency can be added after the subtraction.

In summary, we have investigated synchronization of chaos in two unidirectionally coupled Mackey-Glass circuits with parameter mismatch and with channel distortion. The synchronization is characterized when the linear amplification/attenuation related with the coupling strength between two circuits and the bandwidth limitation implemented by a low pass filter in transmission are considered. The calculation of the shifted cross-correlation coefficient and its maximum with the corresponding time shift helps us to understand how the receiver responds in various parameter regimes. It is observed that the inclusion of the frequency components up to the fundamental frequency f_1, which is equivalent to the condition

161
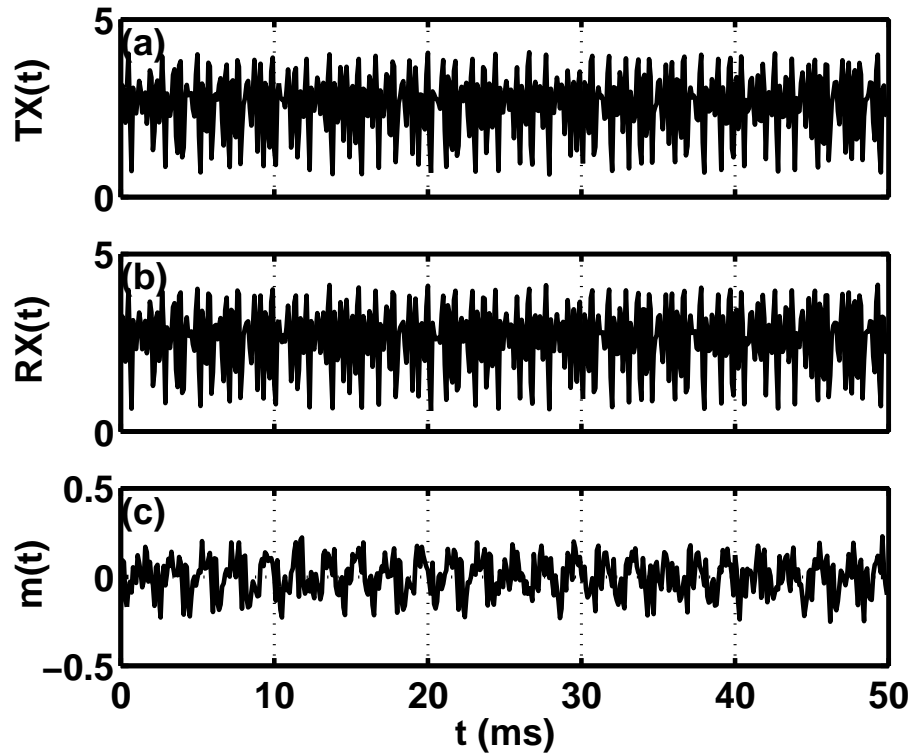
Figure 6.29: Synchronization with a 500 Hz sinusoidal message. (a) The time series of the driver output $TX(t)$, (b) the time series of the receiver output $RX(t)$, and (d) the subtracted messages $m'(t) = RX(t) - TX(t)$.

$f_c > f_1$, is crucial to achieve synchronization between the receiver and the driver circuits. In addition, the time shift at the maximum correlation is closely related both to the average phase change induced by a low pass filter in the transmission line and to the coupling strength between the driver and receiver circuits.

Chapter 7

Conclusion

7.1   Summary

In this thesis, we have studied delay induced instabilities in two different systems. One consists of two cross-coupled semiconductor lasers with time-delayed negative optoelectronic coupling, and the other consists of two unidirectionally coupled electronic circuits with time-delayed nonlinear feedback.

First we have studied the dynamics of cross-coupled lasers near the onset of oscillations. In the experiment, a signal proportional to the light power fluctuations of one laser modulates the injection current of the other laser through time-delayed negative optoelectronic coupling. As the coupling is made stronger than a critical value, the sinusoidal oscillations in the laser outputs are observed to grow in amplitude thereafter. It is seen that the oscillating signals from the lasers are in phase and that the period of the oscillations is twice the delay time. By varying coupling strengths in each direction asymmetrically, we observed that the onset of oscillations occurs when the product of the coupling strengths increases through a critical value. We also observed a scaling law between rescaled amplitudes of the oscillations and the product of the coupling strengths.

In order to verify experimental observations, linear stability analysis and numerical simulations of the rescaled coupled laser equations were carried out. The

linear stability analysis showed that there exist an internal mode corresponding to the relaxation oscillations and an infinite number of external modes induced by the time-delayed negative coupling. The onset condition of each mode is again determined by the value of the product of the coupling constants, and the critical value of the product for the internal mode is smaller than that for the external mode without filters in the delay loop. From the numerical simulations, it was observed that the internal mode emerges as the product of the coupling constants increases. The scaling relationship was again observed between the rescaled amplitudes and the product of the coupling constants near the onset of the periodic oscillations. The ratio of the rescaled variables from each laser was found to be unity from the numerical simulations.

As the coupling increases, the dynamics of the system is determined by the competition between the relaxation oscillations (internal mode) and the delay induced oscillations (external mode) with bandwidth limitations on the delay loop. By including a low pass filter in the delay loop, we introduced a frequency dependent coupling strength. When the cut off frequency of a low pass filter is placed between the relaxation oscillation frequency and the fundamental frequency, the internal mode is suppressed and the fundamental external mode emerges as the coupling increases in strength.

In Chapter 4, we studied the periodicity and the phase relation of the cross-coupled laser outputs experimentally as we adjusted the delay time by inserting additional fibers of different lengths on the optical path of the delay loop. In-phase oscillations at the fundamental frequency dominate for smaller delay times, while

anti-phase oscillations with higher order harmonic frequencies appear as the delay time is increased. The time-shifted cross-correlation coefficient is calculated between the two laser outputs in order to reveal the underlying dynamics. In addition, the effect of an external modulation was experimentally investigated by varying the modulation frequency at different modulation amplitudes. The external modulation of the input bias current and the delay-induced oscillations compete to arrive at a stable state.

In the second part of the thesis, we studied the dynamics of the electronic circuits with time-delayed nonlinear feedback. In Chapter 5, we investigated how the dynamics of the Mackey-Glass system depend on different parameters. First, the delay time was varied for the fixed value of the linear gain, and then the linear gain was varied for a fixed delay time. Both the delay time and the linear gain can be used as a control parameter to determine the dynamics of the system, and each parameter demonstrates a period doubling route to chaos. We generated chaotic signals experimentally and numerically by matching parameters and carrying out proper conversions of the variables.

In Chapter 6, we investigated synchronization of chaos in two unidirectionally coupled Mackey-Glass circuits under different conditions. The quality of synchronization was studied when the receiver is set in either an open-loop or closed-loop configuration, and we observed that the open-loop configuration shows a better quality of synchronization. With an open-loop receiver, the effect of the circuit parameter mismatch, coupling strength and bandwidth limitation in the transmission channel has been considered. The calculation of the time-shifted cross-correlation

coefficient and its maximum with the corresponding time shift helps us to understand how the receiver responds in various parameter regimes.

Numerical simulations showed that the effect of mismatching circuit parameters is not as important as that of the coupling strength to achieve synchronization between the driver and receiver circuits. The receiver is directly modulated by the transmitted signal when linear attenuation or amplification occurs during transmission. With a low pass filter in the transmission line, we observed that the inclusion of the frequency components up to the fundamental frequency of the driver signal is crucial to achieve synchronization between the receiver and the driver circuits, both numerically and experimentally. The maximum cross-correlation and the corresponding time shift reveal that the frequency dependent attenuation and phase distortion due to a low pass filter in the transmission channel change the quality of synchronization.

7.2   Future work

In the first part of this thesis, we studied the influence of asymmetric coupling strengths on the dynamics of two cross-coupled lasers with time-delayed negative optoelectronic coupling for a fixed delay as well as the dependence of periodicity and phase relations on different values of the delay time. Since we were interested in the asymmetry in coupling strengths, we matched other parameters in both systems, including injection currents and time delays. However, it is more likely to happen that two coupled systems in nature have mismatching parameters. In addition,

167

the propagation delay time in one direction can be different from that in the other direction. Therefore, there is a need to investigate the influence of asymmetric injection currents and asymmetric propagation time delays on the dynamics of the two cross-coupled lasers. From the analogy between laser population dynamics and disease population dynamics, these asymmetries are of particular interest because the size of the populations as well as the disease transmission mechanisms can be asymmetric.

We discussed the competition between dynamics of different time scales by performing experiments in two schemes of operation. In one condition, the delay time of the optoelectronic loop was varied, and in the other condition, an external modulation was added to the injection current of one laser. We observed that the periodicity and the phase relation of the oscillating outputs from the lasers are determined by the competition between dynamics with different time scales. In order to understand the origins of different time scales, we need to carry out more numerical simulations for different situations. One way to introduce a new time scale is to add sinusoidal modulation terms to the injection current in the coupled laser equations. Another way is to assign a sinusoidally varying initial condition or a piecewise constant initial condition with the time scale of interest. The effect of filters in the delay loop and that of spontaneous emission noise are also important topics to be considered.

We are interested in the dynamics of systems with more than two lasers. For example, we can add one more laser to the existing two cross-coupled lasers. All three lasers can be coupled in a linear structure or in a circular structure. The change

in the periodicity and the phase relations among the lasers under different coupling conditions may lead us to understand the spatio-temporal patterns observed in the incidences of epidemics.

In the second part of this thesis, we studied synchronization of the two unidirectionally coupled electronic circuits with an open-loop receiver configuration. It will be interesting to study synchronization of two bidirectionally coupled circuits where both circuits are in closed loop configurations. In Ref. [89], it is shown that bidirectionally coupled fiber ring lasers are synchronized at a weaker coupling level than unidirectionally coupled fiber ring lasers, and that the role as a leader and a follower switches between two fiber ring lasers in time. Based on these results, we can study whether the same phenomena observed in the coupled fiber lasers can now be shown with bidirectionally coupled electronic circuits.

BIBLIOGRAPHY

[1] K. Ikeda, "Multiple-valued stationary state and its instability of the transmitted light by a ring cavity system", Optics Comm. **30**, 257 (1979).

[2] K. Ikeda, H. Daido and O. Akimoto, "Optical turbulence: chaotic behavior of transmitted light from a ring cavity", Phys. Rev. Lett. **45**, 709 (1980).

[3] K. Ikeda, H. Daido and O. Akimoto, "Successive higher-harmonic bifurcations in systems with delayed feedback", Phys. Rev. Lett. **49**, 1467 (1982).

[4] M.C. Mackey and L. Glass, "Oscillation and chaos in physiological control systems", Science **197**, 287 (1977).

[5] R.M. May, *Stability and Complexity in Model Ecosystems* (Princeton University Press, Princeton, NJ, 2001), Chap. 4.

[6] J. Sacher, D. Baums, P. Panknin, W. Elsasser and E.O. Gabel, "Intensity instabilities of semiconductor lasers under current modulation, external light injection, and delayed feedback", Phys. Rev. A **45**, 1893 (1992).

[7] T.B. Simpson, J.M. Liu, A. Gavrielides, V. Kovanis and P.M. Alsing, "Period-doubling cascades and chaos in a semiconductor laser with optical injection", Phys. Rev. A **51**, 4181 (1995).

[8] J.R. Tredicce, F.T. Arecchi, G.L. Lippi and G.P. Pucchioni, "Instabilities in lasers with an injected signal", J. Opt. Soc. Am. B **2**, 173 (1985).

[9] J. Mork, B. Tromborg and J. Mark, "Chaos in semiconductor lasers with optical feedback: Theory and experiment", IEEE J. Quantum Electron. **28**, 93 (1992).

[10] J. Mork, B. Tromborg and P.L. Christiansen, "Bistability and low-frequency fluctuations in semiconductor lasers with optical feedback: A theoretical analysis", IEEE J. Quantum Electron. **24**, 124 (1988).

[11] C.H. Henry and R.F. Kazarinov, "Instability of semiconductor lasers due to optical feedback from distant reflectors", IEEE J. Quantum Electron. **22**, 294 (1986).

[12] S. Tang and J.M. Liu, "Chaotic pulsing and quasi-periodic route to chaos in a semiconductor laser with delayed opto-electronic feedback", IEEE J. Quantum Electron. **37**, 329 (2001).

[13] H. Nakatsuka, S. Asaka, H. Itoh, K. Ikeda and M. Matsuoka, "Observation of Bifurcation to chaos in an all-optical bistable system", Phys. Rev. Lett. **50**, 109 (1983).

[14] F.T. Arecchi, G. Giacomelli, A. Lapucci and R. Meucci, "Dynamics of a CO_2 laser with delayed feedback: The short-delay regime", Phys. Rev. A **43**, 4997 (1991).

[15] J.N. Blakely, L. Illing and D.J. Gauthier, "High-speed chaos in an optical feedback system with flexible timescales", IEEE J. Quantum Electron. **40**, 299 (2004).

[16] Y. Kuramoto, *Chemical Oscillations, Waves, and Turbulence* (Springer-Verlag, Berlin, 1984).

[17] H.G. Schuster and P. Wagner, "Mutual entrainment of two limit cycle oscillators with time delayed coupling", Prog. Theor. Phys. **81**, 939 (1989).

[18] M.K.S. Yeung and S.H. Strogatz, "Time delay in the kuramoto model of coupled oscillators", Phys. Rev. Lett. **82**, 648 (1999).

[19] M. Bestehorn, E.V. Grigorieva, H. Haken and S.A. Kaschenko, "Order parameters for class-B lasers with a long time delayed feedback", Physica D **145**, 110 (2000).

[20] D. Pieroux, T. Erneux, A. Gavrielides and V. Kovanis, "Hopf bifurcation subject to a large delay in a laser system", SIAM J. Appl. Math. **61**, 966 (2000).

[21] B.M. Bolker and B.T. Grenfell, "Chaos and biological complexity in measles dynamics", Proc. R. Sco. Lond. B **251**, 75 (1993).

[22] M. Keeling and B. Grenfell, "Stochastic dynamics and a power law for measles variability", Phil. Trans. R. Soc. Lond. B **354**, 769 (1999).

[23] B.T. Grenfell, O.N. Bjornstad and J. Kappey, "Travelling waves and spatial hierarchies in measles epidemics", Nature **414**, 716 (2001).

[24] L. Billings and I.B. Schwartz, "Exciting chaos with noise: unexpected dynamics in epidemic outbreaks", J. Math. Biol. **44**, 31 (2002).

[25] A.L. Lloyd and V.A.A. Jansen, "Spatiotemporal dynamics of epidemics: synchrony in metapopulation models", Math. Biosci. **188**, 1 (2004).

[26] A.L. Lloyd and R.M. May, "Spatial heterogeneity in epidemic models", J. Theor. Biol. **179**, 1 (1996).

[27] P. Rohani, D.J.D. Earn and B.T. Grenfell, "Opposite patterns of synchrony in sympatric disease metapopulations", Science **286**, 968 (1999).

[28] M.J. Keeling and P. Rohani, "Estimating spatial coupling in epidemiological systems: a mechanistic approach", Ecol. Lett. **5**, 20 (2002).

[29] J.D. Farmer, "Chaotic attractors of an infinite-dimensional dynamical system", Physica **4D**, 366 (1982).

[30] P. Grassberger and I. Procaccia, "Measuring the strangeness of strange attractors", Physica **9D**, 189 (1983).

[31] J. Losson, M.C. Mackey and A. Longtin, "Solution multistability in first-order nonlinear differential delay equations", Chaos **3**, 167 (1993).

[32] B. Mensour and A. Longtin, "Power spectra and dynamical invariants for delay-differential and difference equations", Physica D **113**, 1 (1998).

[33] B. Mensour and A. Longtin, "Chaos control in multistable delay-differential equations and their singular limit maps", Phys. Rev. E **58**, 410 (1998).

[34] A. Namajunas, K. Pyragas, and A. Tamasevicius, "An electronic analog of the Mackey-Glass system", Phys. Lett. A **201**, 42 (1995).

[35] A. Namajunas, K. Pyragas, and A. Tamasevicius, "Stabilization of an unstable steady state in a Mackey-Glass system", Phys. Lett. A **204**, 255 (1995).

[36] S. Boccaletti, D.L. Valladares, J. Kurths, D. Maza and H. Mancini, "Synchronization of chaotic structurally nonequivalent systems", Phys. Rev. E **61**, 3712 (2000).

[37] H.U. Voss, "Real-time anticipation of chaotic states of an electronic circuit", Int. J. Bifurcation Chaos **12**, 1619 (2002).

[38] L.M. Pecora and T.L. Carroll, "Synchronization in chaotic systems", Phys. Rev. Lett. **8**, 821 (1990).

[39] L. Kocarev, K.S. Halle, K. Eckert, L.O. Chua and U. Parlitz, "Exerimental demonstration of secure communications via chaotic synchronization", Int. J. Bifurcation Chaos **2**, 709 (1992).

[40] K.M. Cuomo and A.V. Oppenheim, "Circuit implementation of synchronized chaos with applications to communications", Phys. Rev. Lett. **71**, 65 (1993).

[41] L. Kocarev and U. Parlitz, "General approach for chaotic synchronization with applications to communication", Phys. Rev. Lett. **74**, 5028 (1995).

[42] U. Parlitz, L. Kocarev, T. Stojanovski and H. Preckel, "Encoding messages using chaotic synchronization", Phys. Rev. E **53**, 4351 (1996).

[43] L. Larger, J.-P. Goedgebuer and F. Delorme, "Optical encryption system using hyperchaos generated by an optoelectronic wavelength oscillator", Phys. Rev. E **57**, 6618 (1998).

[44] G.D. VanWiggeren and R. Roy, "Communications with chaotic lasers", Science **279**, 1198 (1998).

[45] S. Tang, H.F. Chen, S.K. Hwang and J.M. Liu, "Message encoding and decoding through chaos modulation in chaotic optical communications", IEEE Trans. Circuits Syst. I **49**, 163 (2002).

[46] J.M. Liu, H.F. Chen and S. Tang, "Synchronized chaotic optical communications at high bit rates", IEEE J. Quantum Electron. **38**, 1184 (2002).

[47] K.S. Halle, C.W. Wu, M. Itho and L. Chua, "Spread spectrum communication through modulation of chaos", Int. J. Bifurcation Chaos **3**, 469 (1993).

[48] C.W. Wu and L. Chua, "A simple way to synchronize chaotic systems with applications to secure communication systems", Int. J. Bifurcation Chaos **3**, 1619 (1993).

[49] T.L. Carroll, "Synchronizing chaotic systems using filtered signals", Phys. Rev. E **50**, 2580 (1994).

[50] T.L. Carroll, "Communicating with use of filtered, synchronized, chaotic signals", IEEE Trans. Circuits Syst. I **42**, 105 (1995).

[51] G.P. Agrawal and N.K. Dutta, *Semiconductor Lasers* (Van Nostrand Reinhold, New York, 1993), Chaps. 1, 2, 6.

[52] C.H. Townes, *How the Laser Happened* (Oxford Univ. Press, New York, 1999) p. 84.

[53] K. Shimoda, H. Takahasi, and C. H. Townes, J. Phys. Soc. Japan **12**, 686 (1957).

[54] L. Billings, E. Bollt, D. Morgan, and I.B. Schwartz, "Stochastic global bifurcation in perturbed hamiltonian systems", in *Proceedings of the fourth international conference on dynamical systems and differential equations, Wilmington, 2002* (American Institute of Mathematical Sciences, Springfield, 2003), p. 122.

[55] B.T. Grenfell, K. Wilson, B.F. Finkenstadt, T.N. Coulson, S. Murray, S.D. Albon, J.M. Pemberton, T.H. Clutton-Brock and M.J. Crawley, "Noise and determinism in synchronized sheep dynamics", Nature **394**, 674 (1998).

[56] I.B. Schwartz and H.L. Smith, "Infinite subharmonic bifurcation in an SEIR epidemic model", J. Math. Biol. **18**, 233 (1983).

[57] R.M. Anderson and R.M. May, *Infectious Diseases of Humans* (Oxford Univ. Press, New York, 1991).

[58] D. Tilman and P. Kareiva, *Spatial Ecology* (Princeton Univ. Press, Princeton, NJ, 1997).

[59] W.H. Hamer, "Epidemic disease in England", The Lancet **1**, 733 (1906).

[60] I.B. Schwartz, "Multiple stable recurrent outbreaks and predictability in seasonally forced nonlinear epidemic models", J. Math. Biol. **21**, 347 (1985).

[61] A.D. Cliff, P. Haggett, and M. Smallman-Raynor, *Measles: An Historical Geography of a Major Human Viral Disease from Global Expansion to Local Retreat, 1840-1990*, (Oxford: Blackwell Reference, 1993).

[62] D.A.T. Cummings, R.A. Irizarry, N.E. Huang, T.P. Endy, A. Nisalak, K. Ungchusak and D.S. Burke, "Travelling waves in the occurrence of dengue haemorrhagic fever in Thailand", Nature **427**, 344 (2004).

[63] M.-Y. Kim, R. Roy, J.L. Aron, T.W. Carr and I.B. Schwartz, "Scaling behavior of laser population dynamics with time-delayed coupling: theory and experiment", Phys. Rev. Lett. **94**, 088101 (2005).

[64] D.J. Gubler, "Dengue and dengue hemorrhagic fever", Clin. Microbiol. Rev. **11**, 480 (1998).

[65] D.J. Gubler, "Epidemic dengue/dengue hemorrhagic fever as a public health, social and economic problem in the 21st century", Trends Microbiol. **10**, 100 (2002).

[66] V. Petrov, Q. Ouyang and H.L. Swinney, "Resonant pattern formation in a chemical system", Nature **388**, 655 (1997).

[67] C.-H. Lee, S.-Y. Shin and S.-Y. Lee, "Optical short-pulse generation using diode lasers with negative optoelectronic feedback", Opt. Lett. **13**, 464 (1988).

[68] C.-H. Lee and S.-Y. Shin, "Self-pulsing, spectral bistability, and chaos in a semiconductor laser diode with optoelectronic feedback", Appl. Phys. Lett. **62**, 922 (1993).

[69] F.Y. Lin and J.M. Liu, "Harmonic frequency locking in a semiconductor laser with delayed negative optoelectronic feedback", Appl. Phys. Lett. **81**, 3128 (2002).

[70] M.-Y. Kim, R. Roy, J.L. Aron, T.W. Carr and I.B. Schwartz, "Delay dependence of cross-coupled population dynamics", in preparation.

[71] T. Aida and P. Davis, "Oscillation modes of laser diode pumped hybrid bistable system with large delay and application to dynamical memory", IEEE J. Quantum Electron. **28**, 686 (1992).

[72] K. Ikeda, K. Kondo and O. Akimoto, "Successive higher-harmonic bifurcations in systems with delayed feedback", Phys. Rev. Lett. **49**, 1467 (1982).

[73] V. Dronov, "Communication with a Chaotic Traveling Wave Tube Microwave Generator", Master thesis, University of Maryland, Collge Park, MD

[74] L. Glass and M.C. Mackey, "Pathological conditions resulting from the instabilities in physiological control systems", Annals of the New York Academy of Science, **316**, 214 (1979).

[75] E. Ott, *Chaos in Dynamical Systems* (Cambridge University Press, New York, NY, 1993).

[76] E. Ott, C. Grebogi and J.A. Yorke, "Controlling chaos", Phys. Rev. Lett. **11**, 1196 (1990).

[77] W.L. Ditto, S.N. Rauseo and M.L. Spano, "Experimental control of chaos", Phys. Rev. Lett. **65**, 3211 (1990).

[78] R. Roy, T.W. Murphy, T.D. Maier and Z. Gills, "Dynamical control of a chaotic laser: experimental stabilization of a globally coupled system", Phys. Rev. Lett. **68**, 1259 (1992).

[79] S. Hayes, C. Grebogi, E. Ott and A. Mark, "Experimental control of chaos for communication", Phys. Rev. Lett. **73**, 1782 (1994).

[80] B. Mensour and A. Longtin, "Controlling chaos to store information in delay-differential equations", Phys. Lett. A **205**, 18 (1995).

[81] S. Boccaletti, C. Grebogi, Y.-C. Lai, H. Mancini and D. Maza, "The control of chaos: Theory and applications", Physics Reports **329**, 103 (2000).

[82] J.M. Liu, H.F. Chen and S. Tang, "Optical-communication systems based on chaos in semiconductor lasers", IEEE Trans. Circuits Syst. I **48**, 1475 (2001).

[83] S. Tang and J.M. Liu, "Message encoding-decoding at 2.5 Gbits/s through synchronization of chaotic pulsing semiconductor lasers", Opt. Lett. **26**, 1843 (2001).

[84] S. Tang and J.M. Liu, "Chaos synchronization in semiconductor lasers with optoelectronic feedback", IEEE J. Quantum Electron. **39**, 708 (2003).

[85] M.W. Lee, J. Paul, S. Sivaprakasam and K.A. Shore, "Competition of closed-loop and open-loop feedback schemes of message decoding using chaotic laser diodes", Opt. Lett. **28**, 2168 (2003).

[86] H.D.I Abarbanel and M.B. Kennel, "Synchronizing high-dimensional chaotic optical ring dynamics", Phys. Rev. Lett. **80** 3153 (1998).

[87] C. Sramek, M.-Y. Kim, A. Uchida and R. Roy, "Synchronization of unidirectionally coupled Mackey-Glass circuits with bandwidth limitation in the transmission channel", in preparation.

[88] J. Millman and A. Grabel, *Microelectronics, 2 ed.* (McGraw-Hill, Singapore, 1987), Chap. 16.

[89] E.A. Rogers, J. Garcia-Ojalvo, D.J. DeShazer and R. Roy, "Spatiotemporal representation of high dimensional dynamics: synchronization and symmetry breaking in mutually coupled fiber ring lasers", submitted to Phys. Rev. Lett.